PROPERTIES AND THERMODYNAMICS OF ANOMALOUS ONE-DIMENSIONAL FERMIONS

Joshua Robert McKenney

A dissertation submitted to the faculty at the University of North Carolina at Chapel Hill in partial fulfillment of the requirements for the degree of Doctor of Philosophy in the Department of Physics & Astronomy.

Chapel Hill
2020

Approved by:

Joaquín E. Drut

Gökçe Başar

Jonathan Engel

Charles R. Evans

Amy Nicholson

ABSTRACT

Joshua Robert McKenney: PROPERTIES AND THERMODYNAMICS OF ANOMALOUS ONE-DIMENSIONAL FERMIONS
(Under the direction of Joaquín E. Drut)

In ultracold Fermi gases, the spatial dimension and the number of particles involved in interactions largely determine the behavior of the system. By exploiting harmonic trapping potentials and multiple hyperfine states, experiments wield a high degree of control over both of these parameters. In this work, we show that a nonrelativistic, one-dimensional, three-component Fermi system with three-body contact interactions exhibits a quantum anomaly, breaking the scale invariance that exists for this system classically. The exact solution of this three-body problem, wherein a bound trimer forms at arbitrarily small attractive couplings, features a correspondence to the two-dimensional, two-body Fermi system, through which we determine the first non-trivial virial coefficient. We further develop a numerical technique for solving the few-body problem for up to six particles and find that the effective interaction between two trimers is repulsive. To extend our analysis to the many-body problem, we apply the worm algorithm of quantum Monte Carlo and present results for various thermodynamic quantities. We find that for increasing attractive couplings, the system undergoes a Fermi-Fermi crossover from a set of three ideal Fermi gases to one weakly repulsive Fermi gas consisting of massive composite trimers. Finally, we adapt the three-body interaction to a two-dimensional lattice model, where we find strong evidence for a second-order phase transition with an associated reduction in a discrete global symmetry. While the exact experimental parameters we require have not yet been physically realized, our work provides a comprehensive first set of predictions for this model.

To my parents, Lori and John, for insisting that I stay in Engineering, and thereby guaranteeing that I studied Physics.

ACKNOWLEDGEMENTS

I thank Joaquín Drut and Lukas Rammelmüller for their helpful feedback on this work, and the UNC Dissertation Completion Fellowship for providing me with the time to write it.

TABLE OF CONTENTS

LIST OF TABLES

LIST OF FIGURES

LIST OF ABBREVIATIONS AND SYMBOLS

1D	One-dimensional
2D	Two-dimensional
3D	Three-dimensional
BEC	Bose-Einstein Condensate
BCS	Bardeen-Cooper-Schrieffer
$\hbar$	Reduced Planck's constant
k_B	Boltzmann's constant
m	Mass
c.m.	Center of mass
g	Interaction coupling strength
L	Length
ϵ_B	Binding energy
∇^2	Laplace operator
i	Imaginary unit, $\sqrt{-1}$
$\mathcal{Q}_n$	Canonical partition function for n particles
$\mathcal{Z}$	Grand canonical partition function
b_n	Virial coefficient of order n
z	Fugacity
μ	Chemical potential
β	Inverse temperature
τ	Imaginary time-step

Ω	Grand potential
κ	Compressibility
χ	Magnetic susceptibility
UV	Ultraviolet
IR	Infrared
$\hat{a}^\dagger$	Particle creation/raising operator
$\hat{a}$	Particle destruction/lowering operator
$\hat{n}$	Particle density operator
$\hat{N}$	Particle number operator
$\hat{H}$	Hamiltonian operator
$\hat{T}$	Kinetic energy operator
$\hat{V}$	Potential energy operator
J_n	Bessel function of the first kind of order n
K_n	Modified Bessel function of the second kind of order n
Γ	Gamma function
γ	Euler-Mascheroni constant
$\psi^{(n)}$	Polygamma function of order n
H_n	Hermite polynomial of order n
L_n	Laguerre polynomial of order n
δ	Dirac delta function, Kronecker delta
L^2	Lebesgue-measure two

CHAPTER 1: INTRODUCTION

Over the last few decades, the subject of ultracold atomic gases has emerged as one of the primary fields of physics. The experimental techniques developed, which involve cooling vapors of neutral atoms to near-absolute zero, have enabled such applications as atomic clocks, extremely sensitive accelerometers, and optical tweezers [1, 2, 3]. As a research tool, ultracold gases can be used to simulate a variety of physical systems relevant to condensed matter, nuclear physics, and general few- to many-body physics [4]. Through the use of Feshbach resonances [5], the effective interaction between the constituent particles can be precisely tuned to engineer a multitude of interesting phenomena, such as Bose-Einstein condensation (BEC) and Bardeen-Cooper-Schrieffer (BCS) superconductivity [6].

Ultracold gases are most commonly realized with alkali metals, where bosonic or fermionic exchange symmetry can be achieved according to the isotopes of the atoms. While BEC and BCS phenomena are typically associated with bosons and fermions, respectively, one of the achievements of ultracold gas experiments has been to demonstrate the BCS-BEC crossover, wherein a two-component Fermi gas with weak attraction passes to a weakly repulsive Bose gas of Cooper pairs when the fermionic attraction is large [7, 8, 9, 10]. This repulsion stems from the Pauli Exclusion Principle, protecting the BEC from collapsing [10]; in our study, we will come across a similar situation, but the gas will remain fermionic at both ends of the crossover.

In addition to the fine-tuning of interactions, ultracold gas experiments are also able to control the effective dimensionality of a system. By applying a strong harmonic trapping potential along one axis, the gas is compressed into a 2D "pancake"; by applying another along a perpendicular axis, the gas is confined to a 1D "cigar." As long as the trap frequencies are much larger than the enery scales of the gas, transverse excitations are suppressed [6, 11], and the problem can be successfully described by a lower-dimensional theory. One of the central themes in this work regards the profound impact that the dimension of a system can have on its physical properties, so we now examine this question in the context of the most common force—the two-body (pairwise) interaction.

Section 1.1: Effect of dimension on the two-body interaction

In electrostatics, Gauss's Law implies that the behavior of point charges differs vastly depending on the dimension in which the charges live. In 3D, the inverse-square law for the electric field dictates that charges

separated by large distances exert little force on each other. The constant field emanating from charges in 1D, on the other hand, reveals that distance plays no part in determining the charges' mutual forces: One will equally feel the influence of the other at separations of light-years or of angstroms.

Similarly, the forces studied in the present work exhibit markedly diverse behaviors according to the spatial dimension in which they operate. The d-dimensional two-body contact (zero-range) interaction takes the form $g\delta^d(\mathbf{x}-\mathbf{y})$, where $\mathbf{x}$ and $\mathbf{y}$ are the positions of the two particles, and the coupling g determines the strength of the interaction (positive for repulsive, negative for attractive).[1] At first glance, the δ-function interaction would appear to behave similarly regardless of dimension—particularly when expressed in Cartesian form,

$$\delta^3(\mathbf{x}-\mathbf{y}) = \delta(x_1-y_1)\delta(x_2-y_2)\delta(x_3-y_3), \tag{1.1}$$

to use the 3D case as an example. However, just as $\delta^3(\mathbf{r}-\mathbf{r}')$ is modified under spherical symmetry,

$$\frac{\delta(r-r')}{4\pi r^2} \neq \frac{\delta(r-r')}{r^2}\delta(\phi-\phi')\delta(\cos\theta-\cos\theta'), \tag{1.2}$$

the inherent radial symmetry of the contact interaction[2] prevents the d-dimensional system from factoring into a d-fold product of 1D systems and is responsible for the variation seen across dimensions. While a detailed derivation is reserved for later on, we provide here an overview of results and their implications for the two-body interaction.

For sufficiently large attractive coupling $-g > 0$, a bound state with negative energy $E \equiv -E_B$, $E_B > 0$, will form. In the center-of-mass (c.m.) frame, the momentum-space wave function for such a bound state is

$$\phi(\mathbf{p}, -\mathbf{p}) \propto \frac{1}{\mathbf{p}^2 + E_B}, \ \forall d, \tag{1.3}$$

where normalization has been omitted. In the course of obtaining Eq. (1.3), consistency demands a strict relationship between the coupling, g, and the binding energy, E_B:

$$-\frac{(2\pi)^d}{g} = \int d^d\mathbf{p}\ \frac{1}{\mathbf{p}^2 + E_B}. \tag{1.4}$$

The relation (1.4) constitutes the *renormalization* condition [12, 13, 14, 15], connecting the physically measurable binding energy to the numerical coupling in the theory. While the integral in (1.4) converges for

[1] To ensure that the interaction term has units of energy, the coupling takes on the appropriate units given the dimension: $[g] = L^{d-2}$, where L is the unit of length.

[2] Since wave functions with nonzero angular momentum vanish at the origin, δ-potentials only operate in the s-wave channel.

$d = 1$, for $d > 1$, the infinite bounds must be replaced by a UV momentum cutoff, $\Lambda \gg \sqrt{E_B}$; we discuss renormalization and momentum cutoffs in detail in the next section. For now, let us examine the three dimensions of interest.

With the cutoff Λ applied as necessary, Eq. (1.4) evalutes to

$$g_{1\mathrm{D}} = -2\sqrt{E_B}, \tag{1.5}$$

$$g_{2\mathrm{D}} = -\frac{4\pi}{\ln\left(\frac{\Lambda^2}{E_B}\right)}, \tag{1.6}$$

$$g_{3\mathrm{D}} = -\frac{2\pi^2}{\Lambda - \frac{\pi}{2}\sqrt{E_B}}, \tag{1.7}$$

where only the leading-order terms in E_B/Λ^2 have been kept.[3] Consider gradually decreasing the binding energy in each case, so that $E_B \to 0$. In 1D, g tends smoothly to zero, connecting with the noninteracting case at zero energy. Here, a bound state may form for infinitesimally small attractive couplings. In 3D, g decreases slightly until hitting a small, but finite, negative value, indicating that there is a threshold attractive value of g that must be met before a bound state can form. In 2D, though, the situation is dramatically different. The coupling indeed approaches zero as E_B does; however, $E_B = 0$ is expressly forbidden by the logarithmic singularity. A bound state forms for arbitrarily small attractive couplings, but unlike in 1D, it is *not* smoothly connected to the noninteracting case [16].

The position-space wave functions shed further light on the small-E_B behavior. Taking the Fourier transform of (1.3),

$$\psi_{1\mathrm{D}}(x, y) \propto \exp\left(-\sqrt{E_B}\,|x - y|\right), \tag{1.8}$$

$$\psi_{2\mathrm{D}}(\mathbf{x}, \mathbf{y}) \propto K_0\left(\sqrt{E_B}\,|\mathbf{x} - \mathbf{y}|\right), \tag{1.9}$$

$$\psi_{3\mathrm{D}}(\mathbf{x}, \mathbf{y}) \propto \frac{1}{|\mathbf{x} - \mathbf{y}|}\exp\left(-\sqrt{E_B}\,|\mathbf{x} - \mathbf{y}|\right), \tag{1.10}$$

where K_0 is the modified Bessel function of the second kind. As $E_B \to 0$, $\psi_{1\mathrm{D}}$ approaches a constant—the noninteracting result. On the other hand, $\psi_{3\mathrm{D}}$ approaches $|\mathbf{x} - \mathbf{y}|^{-1}$. This function is not normalizable in 3D, meaning it cannot be a bound state ($E \geq 0$); however, it still displays localization around $\mathbf{x} = \mathbf{y}$, indicating an attractive coupling. The 2D case is the most interesting: For small arguments, $K_0(x) \sim \ln x$, revealing that as $E_B \to 0$, instead of approaching the noninteracting wave function (or some other sensible configuration), $\psi_{2\mathrm{D}}$ diverges logarithmically.

[3] For $d = 3$, the $\sqrt{E_B}$ term is not leading order; we include it here for illustrative purposes.

All of the arguments based on the renormalization of the couplings are supported by the features of the spatial wave functions. In 1D and 3D, the bound two-body system connects continuously to the unbound problem—at $g = 0$ in 1D, and at some finite value of $g < 0$ in 3D. The bound 2D system stands alone, fundamentally disconnected from its unbound counterpart.

Section 1.2: Regularization, renormalization, and the taming of the δ-potential

As we saw in the previous section, δ-potentials in $d > 1$ lead to divergent integrals. This may not appear surprising, given the singular nature of the δ-function; after all, the Dirac delta is not truly a *function*, but rather (upon combination with an integral) a *linear functional* (or *distribution*) [17]. Accordingly, the introduction of a seemingly *ad hoc* regularization parameter (Λ)—to remedy the obviously unphysical divergence of the δ-function at saturation—is highly suspect and must be justified.

Divergent quantities came into the spotlight during the development of quantum electrodynamics (QED). The "bare" electron charge, e, and mass, m, were predicted to diverge [18]; experimental measurements of e and m, on the other hand, clearly showed that these were finite quantities. By replacing the infinite parameters of the Lagrangian with finite, experimental values, the infinities of QED were effectively swept under the rug. Combinations of infinite quantities that yielded finite numbers, such as ratios and differences, enabled sensible predictions, and the "shut up and calculate" attitude prevailed over consternations stemming from the formal divergences. As part of this procedure of *renormalization*, the electron charge e was shown to vary with the energy scale (rather than remaining constant) and acquired the self-contradictory label of "running" coupling constant.

In the following years, Wilson [19] built on the ideas of Kadanoff [20] to develop a satisfying interpretation of the renormalization group (RG) equations. The core of the idea is to reduce the number of degrees of freedom in a problem by progressively examining the problem at different scales. For instance, Wilson [21] illustrates the concept with the case of hydrodynamics (Fig. 1.1). While one *could* attempt to keep track of individual molecules and their pairwise interactions, in hydrodynamics, one "zooms out" and instead considers blocks of space that contain many such molecules. The degrees of freedom transition from molecules to local densities within the blocks; the process of renormalization then consists of relating the coupling constants of the interactions between molecules to the coupling constants of the interactions between neighboring blocks. The detailed behavior of the molecules is absorbed into and captured by the evolution of the renormalized coupling constants in the density picture.

Importantly, the renormalized picture of blocks of density comes with a range of applicability. At length scales much larger than the size of the blocks, we expect not to see problems; however, once we try to apply

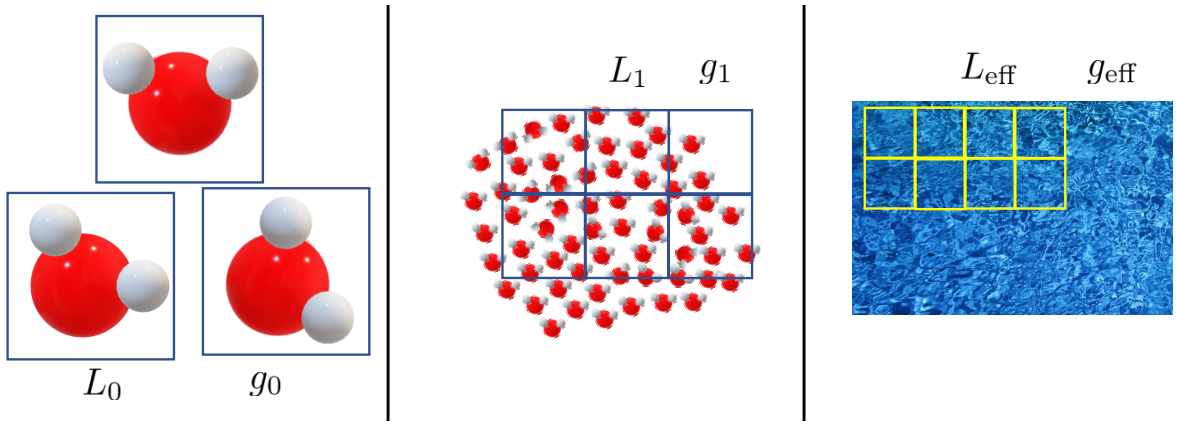

Figure 1.1: Schematic depiction of the progression of length scales and couplings in hydrodynamics. The size of what constitutes a "unit" grows from individual water molecules until the collection can be well approximated as a continuous fluid characterized by the density in each cell.

this model to scales of the order of the block size or smaller, the approach breaks down. Essentially, the zoomed-out model, by construction, neglects the detailed physics that goes on within each block, so there is no sense in asking such details of it. The minimum length scale supplied by the block size is known as a UV cutoff; instead of being an *ad hoc* regulator, we see that it serves as the boundary between two different conceptual pictures.

Another example of renormalization as the separation of length scales arises in the field of nuclear physics. In low-energy chiral effective field theory (χEFT) [22, 23, 24], hadrons are regarded as the primary degrees of freedom. Explicitly, the dynamics of quarks and gluons inside the hadrons is neglected; implicitly, the running of the coupling constants in the effective theory accounts for the short-scale physics. In connection with the previous example, nucleons and mesons are the "blocks," and quarks and gluons are the "molecules." Thus, while χEFT provides reasonable predictions in its area of applicability (energies lower than $\Lambda_\chi \sim 1$ GeV), one cannot expect it to provide a description of parton dynamics.

In the present work, the divergence of the δ-potential when its argument vanishes is cause for discomfort. Here, as in the examples discussed above, the separation of scales is essential. The singular behavior of the δ-function is confined to an infinitesimal neighborhood; if our theory has a finite spatial resolution (UV momentum cutoff, Λ), then it never "sees" the divergent peak of the δ-function. If we disregard the details of the smallest spatial scales and "smear" the potential over a finite (but small) interval,[4] then the δ-potential is no longer problematic and instead takes on the character of a generic short-range potential. Of course, the strength of the potential will depend on the chosen Λ; the precise relationship between these two quantities

[4]For a pedagogical discussion of such a treatment of singular potentials, see Ref. [25].

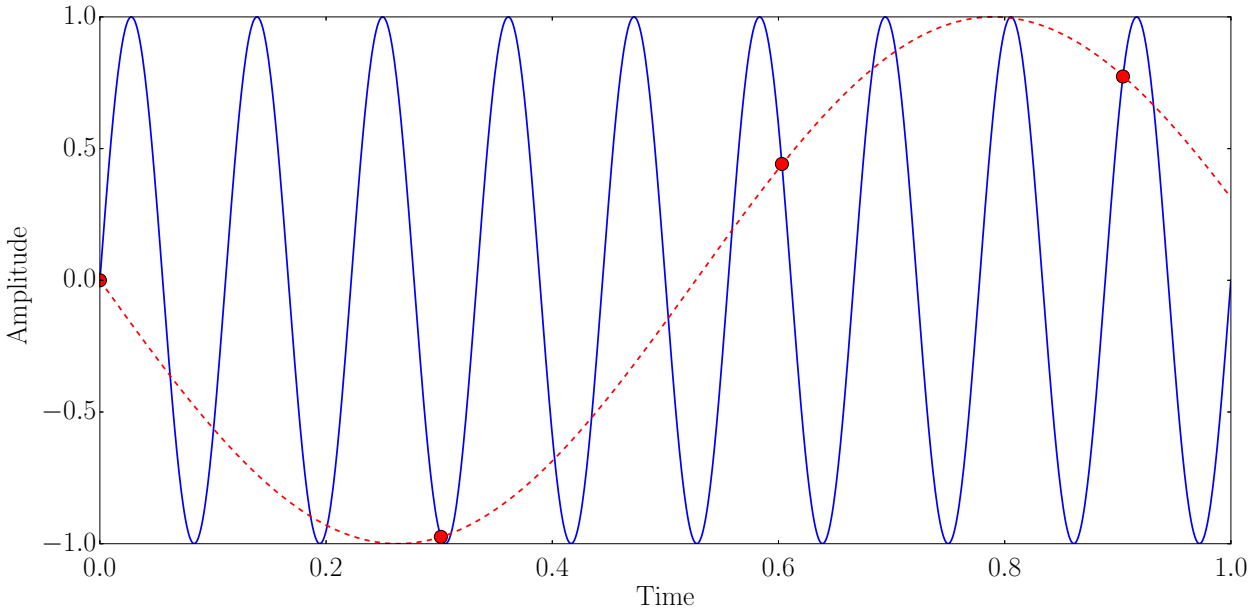

Figure 1.2: If a signal (blue curve) is sampled (red dots) too infrequently—below the Nyquist frequency—the apparent signal will be distorted (red dashed curve). Units arbitrary.

is furnished by renormalization.

When space is represented by a discrete lattice, the spacing ℓ between lattice sites provides a natural UV cutoff: Since the wave function does not have support in the gap between lattice sites, there is no physical content at scales smaller than ℓ. Furthermore, as the δ-function is replaced with the Kronecker-δ on the lattice, there is no issue of divergence.

Still, the cutoff must not be neglected. With an increasingly attractive coupling, a bound state will become more and more localized in space. Once the size of a physically relevant object like a bound molecule approaches the lattice spacing ℓ, the lattice loses the ability to resolve the internal structure of the object. Mathematically speaking, the discretization of space implies a finite number of basis states; increasingly localized distributions in position space require larger and larger momentum modes. Eventually, the spatial localization exceeds the resolution possible for a fixed-size momentum basis, and the theory breaks down. However, the breakdown will not be apparent without proper attention. Numerical evaluation at invalid coupling strengths will still yield energy values, but in accordance with the Nyquist-Shannon Sampling Theorem [26], the values will be nonsensical (see Figs. 1.2 and 1.3). As a result, one must ensure that the separation of scales assumed by the renormalization scheme is maintained at all times.

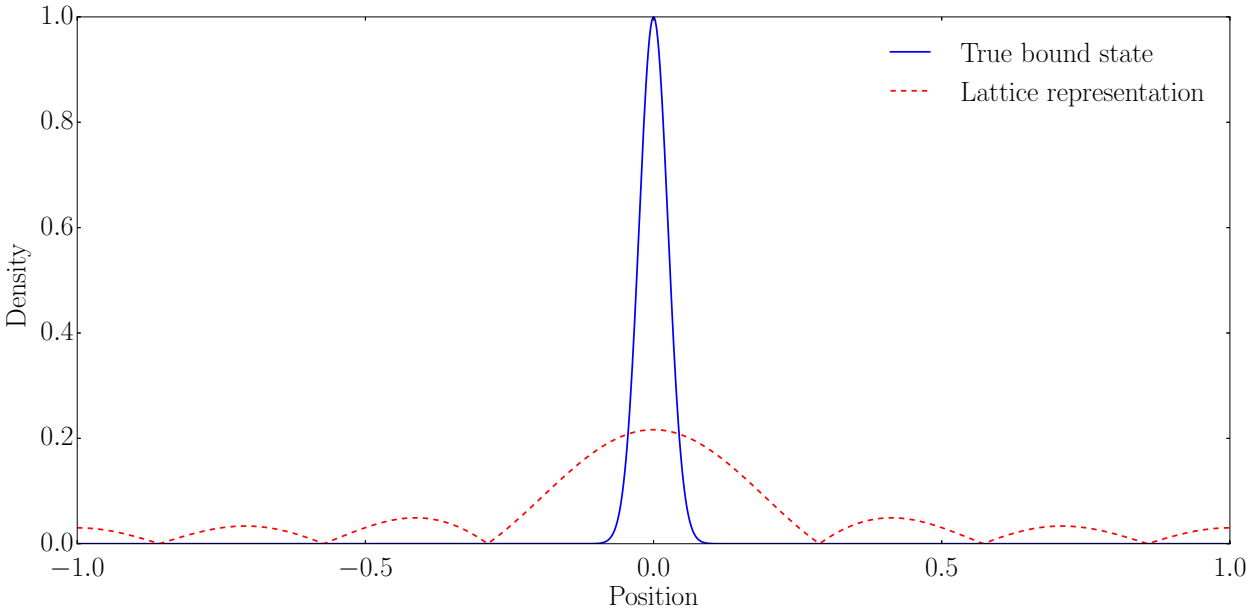

Figure 1.3: If the size of a tightly bound molecule (blue curve) cannot be resolved by the lattice spacing, a numerical result will still be produced, but the apparent density (dashed red curve) and its associated energy will be misleading. Units arbitrary.

Section 1.3: The few-body problem, n-body forces, and experimental prospects

Since the time of Newton, the three-body problem has eluded attempts at exact solutions. Even today, the three-body problem remains of interest to various fields, such as astrophysics and nuclear physics [27, 28, 29]. The real difficulty lies not just in the number of particles, but in the number of particles *in relation to* the number of particles that take part in the basic interaction (the primitive vertex, in field theory language). Particularly with a contact interaction, the n-body problem can always be solved exactly for an m-body force if $n = m$, where the relative problem (factoring out the center of mass) reduces to a one-body problem in dimension $d = n - 1$ (similar to Eq. (1.3)). When $n > m$, however, the center-of-mass frame is not sufficient to enable an exact solution; as a result, numerous approximate and numerical methods have been applied in the $n = 3$, $m = 2$ problem [30, 31, 32, 33, 34].

Even with only a two-body interaction, three-body (and higher) forces can be induced among bosons as effective corrections to the unphysical pure δ-function interaction [35, 36, 37, 38, 39, 40, 41, 42]. Many theoretical studies have investigated the properties of bosons with such three-body forces [43, 44, 45], revealing deeply bound "droplets" for increasing numbers of particles [46]. For fermions, both theory and experiment have also explored higher-body interactions [47, 48, 49], where additional fermionic components (beyond two) become necessary for contact interactions. A number of groups have studied [50, 51, 52, 53, 54, 55, 56, 57]

and realized [58, 59] multi-component Fermi gases—especially for three-components [60, 61, 62]—by using hyperfine states to tune the number of spin components [63]. While two-body forces may be suppressed to achieve a dominant three-body interaction among bosons [64], we are not yet aware of a theoretical or experimental study which has claimed that the same is true for fermions. Nevertheless, in this work, we still study the three-component Fermi gas with exclusive three-body interactions, furnishing predictions in the hope that experimentalists will discover a way of realizing this system.

Section 1.4: Overview

We begin in Ch. 2 by introducing the 1D, nonrelativistic, three-component Fermi system with three-body interactions in the simplest case of three distinguishable particles. This problem, which we solve exactly, enables a first estimate of the many-body thermodynamic properties of this model. In Ch. 3, we extend the analysis of this model for up to six particles, where numerical methods become necessary. Here, the six-particle case gives further insight to the possible behavior of the many-body problem. We introduce a harmonic oscillator potential in Ch. 4, where, while a three-body exact solution is still possible, the few-body method of Ch. 3 fails. Still, we obtain approximate results for the many-body thermodynamics in a trap. In Ch. 5, we turn to the full many-body problem, where we employ stochastic methods to obtain thermodynamic quantities numerically. The results therein constitute the pinnacle of the preceding chapters. The final chapter, Ch. 6, introduces a version of the three-body model adapted to a 2D lattice, where we explore thermodynamic properties and the existence of a phase transition.

CHAPTER 2: QUANTUM SCALING ANOMALY IN 1D SYSTEMS WITH THREE-BODY INTERACTIONS

Classically, three particles interacting via a point-like attractive potential will mostly behave as if they were noninteracting. Since classical particles have no spatial extent, they will only experience a force if they coincide at the *exact* same location at the *exact* same time. In the event of such a collision, the infinite strength of the δ-potential will cause the particles to become irreversibly bound and subsequently drift along with the center-of-mass momentum. Since mathematical points are infinitesimal at all scales, these dynamics are unaffected by the size of the system; we say that the classical problem is invariant under spatial rescaling, with the symmetry group SO(2,1) (the Lorentz group of $2+1$ spacetime).

Quantum mechanically, however, the wave function describing a particle may take non-zero values at more than one location in space, effectively giving the particle a spatial extent. For example, a plane wave state, which has non-zero amplitude at all spatial locations, would *always* feel the presence of a point-like potential. Let us examine in detail how the quantum mechanical problem differs from the classical one.

Representing the spatial coordinates of the three particles by x, y, and z, the Hamiltonian is[1][2]

$$\hat{H} = -\frac{1}{2m}\left(\frac{\partial^2}{\partial x^2} + \frac{\partial^2}{\partial y^2} + \frac{\partial^2}{\partial z^2}\right) + g\delta(x-y)\delta(y-z). \tag{2.1}$$

From (2.1), we see already that the dynamics appear to be invariant under spatial rescaling: With all coordinates scaled by a factor λ ($x \to \lambda x$, etc.), the Hamiltonian is only modified by an overall factor,[3] $\hat{H} \to \hat{H}/\lambda^2$. As the coupling, g, is dimensionless,[4] its magnitude is unaffected by such rescaling, indicating that the relative strengths of the kinetic and potential energies are fixed by g and are constant at all energy scales. As a result, *if* a bound state can form for a given value of $g < 0$, then that value of g will induce a bound state regardless of how small or large the system is. As we show in the following sections—perhaps surprisingly—a bound state will form for *any* value of $g < 0$. Such a bound state will have a characteristic

[1] Note that an additional term of $\delta(z-x)$ is not required since $\int dy\ \delta(x-y)\delta(y-z) = \delta(z-x)$ [65].

[2] While we rely on different spin states to achieve three components, they are fixed quantum numbers rather than dynamic variables in this model and do not enter the Hamiltonian [11].

[3] Recall that $\delta(ax) = \frac{1}{|a|}\delta(x)$.

[4] With $\hbar = 1$, the units of energy are inverse squared length.

size, destroying the scale invariance seen classically and giving rise to the "anomaly."

Section 2.1: Wave function solution

As outlined in Ref. [66], we employ the center-of-mass (c.m.) variables $Q = \frac{1}{3}(x+y+z)$, $q_1 = y - x$, and $q_2 = \frac{1}{\sqrt{3}}(x+y-2z)$. In these coordinates, the Schrödinger equation separates into one equation for the c.m.,

$$-\frac{1}{2M}\frac{\partial^2 \Phi(Q)}{\partial Q^2} = E_{\text{c.m.}}\Phi(Q), \tag{2.2}$$

where $M = 3m$ and $\Phi(Q)$ is the c.m. wave function; and one for the relative motion,

$$\left[-\frac{1}{2\bar{m}}\nabla_q^2 + \tilde{g}\delta^2(\mathbf{q})\right]\phi(\mathbf{q}) = E_r\phi(\mathbf{q}), \tag{2.3}$$

where the reduced mass $\bar{m} = m/2$, $\mathbf{q} = (q_1, q_2)$, $\tilde{g} = 2g/\sqrt{3}$, $\phi(\mathbf{q})$ is the relative wave function, and E_r is its energy. In this form, Eq. (2.3) is equivalent to the problem of one particle in 2D with a δ-potential at the origin. As detailed in Appendix A, the momentum-space solution is given by[5]

$$\tilde{\phi}(\mathbf{p}) \propto \frac{1}{p^2 + \epsilon_B}, \tag{2.4}$$

where $\epsilon_B = -E_r$ is the trimer binding energy.

The position-space wave function may be obtained by Fourier transformation of Eq. (2.4). If one retains a finite momentum cutoff Λ, the Fourier transform may be carried out in 2D polar coordinates by first performing the azimuthal integral [67, 68], followed by repeated integration by parts, yielding the series solution

$$\phi(\mathbf{q}) \propto \sum_{n=1}^{\infty} 2^{n-1}(n-1)!\frac{J_n(q\Lambda)}{(q\Lambda)^n}. \tag{2.5}$$

If the UV momentum cutoff is instead taken to infinity, then the wave function is [69]

$$\phi(\mathbf{q}) \propto K_0\left(\sqrt{\epsilon_B}q\right). \tag{2.6}$$

For $\sqrt{\epsilon_B}q \ll 1$, $K_0\left(\sqrt{\epsilon_B}q\right) \propto \ln\left(\sqrt{\epsilon_B}q\right)$, again reflecting the close relationship between the 1D three-body interaction and 2D systems.[6]

[5] Assuming a solution energy $E_r < 0$, to be verified later.

[6] The magnitude $q \equiv |\mathbf{q}|$ is known as the *hyperradius*.

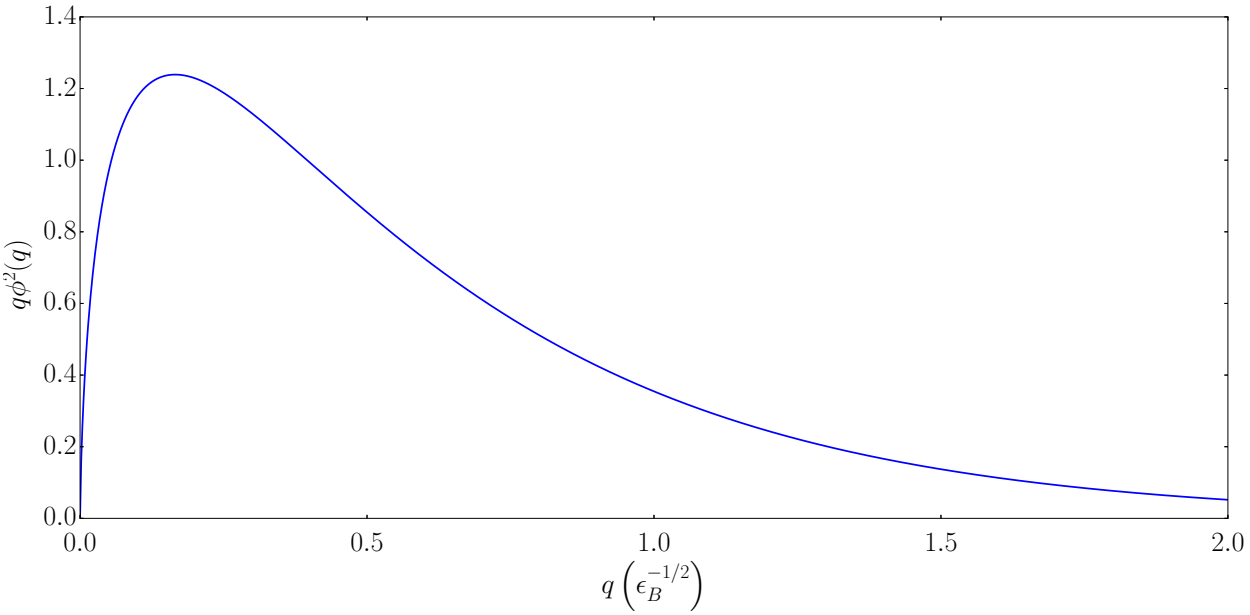

Figure 2.1: Probability density of trimer hyperradius.

Even though the wave function (2.6) diverges at the origin, the associated probability density is finite $\left(\lim_{x\to 0} xK_0^2(x) = 0\right)$, and $\phi(\mathbf{q})$ is L^2-integrable. Figure 2.1 demonstrates the relationship between trimer size and binding energy, indicating that the most probable trimer size is roughly $q_0 \approx \epsilon_B^{-1/2}/6$. While either q_0 or the expectation value $\langle q\rangle = \pi^2/16\ \epsilon_B^{-1/2}$ may be used as the characteristic trimer size, both demonstrate that the trimer grows or shrinks proportionally with space upon dilatation. In contrast, the classical problem is completely immune to spatial scales.

Section 2.2: Renormalization

The normalization factor of wave functions is typically a marginally relevant afterthought, and the previous section only stated the functional form of $\tilde{\phi}$. However, as both sides of Eq. (A.7) contain $\tilde{\phi}$, the normalization drops out, leaving behind a condition that must be obeyed by the coupling $\tilde{g}$. Integrating both sides of Eq. (A.7) leads to

$$-\frac{2\pi}{\tilde{g}} = \int_0^\Lambda dp\ \frac{p}{p^2+\epsilon_B} = \frac{1}{2}\ln\left(\frac{\Lambda^2}{\epsilon_B}+1\right), \tag{2.7}$$

where a UV momentum cutoff Λ has been introduced to keep the integral finite. Since $\Lambda^2 \gg \epsilon_B$, we may neglect the unit term in the logarithm and write

$$\epsilon_B = \Lambda^2 \exp\left(\frac{4\pi}{\tilde{g}}\right). \tag{2.8}$$

The essential singularity at $\tilde{g} = 0$ highlights the nonperturbative nature of the three-body problem and verifies that a bound state forms at arbitrarily weak couplings.

In the discrete (periodic ring or spatial lattice) case, g is not modified like $\tilde{g}$, and the integral becomes a sum:

$$-\frac{1}{g} = \frac{1}{4\pi^2} \sum_{n,m=-\Lambda}^{\Lambda} \frac{1}{n^2 + nm + m^2 + \varepsilon_B}, \tag{2.9}$$

where $\varepsilon_B = \epsilon_B (L/2\pi)^2$ (L is the length of the lattice) and Λ is imposed by the maximum momentum mode possible for the lattice size. On the lattice, then, the UV momentum cutoff Λ is natural and unavoidable, reflecting the fact that the lattice spacing imposes a finite spatial resolution. The logarithmic character is still seen here, however, as Eq. (2.9) diverges like the harmonic series in the $\Lambda \to \infty$ limit.

Now that we have solved the three-body problem, let us examine what it can reveal about the many-body problem.

Section 2.3: The grand canonical ensemble and the virial expansion

In the grand canonical ensemble, the system may exchange energy and particles with a "reservoir"[7] to reach thermal and chemical equilibrium. The relevant parameters for these equilibria are the (inverse) temperature β and the chemical potential μ, which measures the energy associated with adding or removing a particle. As is typical in thermodynamics, the system is completely described by its partition function. For a (quantum) Hamiltonian $\hat{H}$, the grand canonical partition function is given by (see [75])

$$\mathcal{Z} = \mathrm{Tr}\left[e^{-\beta(\hat{H} - \mu\hat{N})}\right], \tag{2.10}$$

where $\hat{N}$ is the particle number operator, and the trace is over the whole Hilbert space. The expectation value of an operator $\hat{\mathcal{O}}$ is defined as

$$\langle\hat{\mathcal{O}}\rangle = \frac{1}{\mathcal{Z}}\mathrm{Tr}\left[\hat{\mathcal{O}} e^{-\beta(\hat{H} - \mu\hat{N})}\right]. \tag{2.11}$$

[7] We note that the traditional "reservoir" picture need not be limited to the somewhat nebulous notion of a heat bath. Instead, thermodynamics can apply when attention is restricted to a small region of an otherwise deterministic system, and "random" (or thermal) behavior emerges as a result of neglecting the details of the region's exterior (see [70, 71, 72, 73, 74]).

Expectation values may thus be obtained by taking log-derivatives of (2.10); for instance, the average energy is

$$\langle \hat{H} \rangle = -\left(\frac{\partial \ln \mathcal{Z}}{\partial \beta} \right)_{\beta\mu} = -\frac{1}{\mathcal{Z}} \left(\frac{\partial \mathcal{Z}}{\partial \beta} \right)_{\beta\mu}, \tag{2.12}$$

where fixing $\beta\mu$ prevents $\mu \langle \hat{N} \rangle$ from being included. Similarly to the Helmholtz free energy in the canonical ensemble, the *grand potential* $\Omega = -PV$ may be used in place of $\ln \mathcal{Z}$ as

$$\Omega = -\frac{1}{\beta} \ln \mathcal{Z}. \tag{2.13}$$

Of course, while the formalism is neat and tidy, the difficulty lies in *obtaining* the partition function. A first step in this direction is to recognize that $[\hat{H}, \hat{N}] = 0$, which allows us to factor the exponential in (2.10) and expand the trace over N-body states as

$$\mathcal{Z} = \sum_{N=0}^{\infty} \langle N | e^{\beta\mu \hat{N}} | N \rangle \operatorname{Tr} \left[e^{-\beta \hat{H}_N} \right] = \sum_{N=0}^{\infty} z^N \mathcal{Q}_N, \tag{2.14}$$

where $z = e^{\beta\mu}$ is the fugacity, and $\mathcal{Q}_N = \operatorname{Tr} \left[e^{-\beta \hat{H}_N} \right]$ is the canonical partition function for N particles. At this point, all we have shown with Eq. (2.14) is that we can solve the general problem by individually solving all of the different N-body cases—not much of a simplification. However, if we restrict our attention to the low-fugacity regime ($z \ll 1$), we can build up an approximate solution by solving the simplest cases and successively adding more particles. Since this means neglecting the contributions from large N, this *virial* expansion will be most accurate when the particle density is low.

Since all observables are computed from $\ln \mathcal{Z}$—not just $\mathcal{Z}$—the virial expansion relies on the Taylor series expansion of the natural logarithm,

$$\ln(1 + x) = x - \frac{x^2}{2} + \frac{x^3}{3} + \ldots, \tag{2.15}$$

valid for $|x| < 1$. In our case,

$$x = z\mathcal{Q}_1 + z^2 \mathcal{Q}_2 + \ldots, \tag{2.16}$$

and the virial expansion is

$$\ln \mathcal{Z} = \mathcal{Q}_1 \left(b_1 z + b_2 z^2 + \ldots \right), \tag{2.17}$$

where $b_1 = 1$,[8] and the remaining b_n (known as the virial coefficients) are found by collecting the coefficients

[8] Factoring out $\mathcal{Q}_1$ is a convention which allows the virial coefficients to be intensive quantities.

of powers of z after applying the expansion (2.15) to Eq. (2.14). In general, each b_n depends on all canonical partition functions up to and including $\mathcal{Q}_n$. As a result, finding b_2 amounts to solving the two-body problem; b_3, the three-body problem; etc.

Section 2.4: Mapping between 1D and 2D problems and the Beth-Uhlenbeck formula

As seen in Eq. (2.3), the Hamiltonian for the relative coordinates of the 3-body problem is equivalent to the Hamiltonian of a particle in 2D subject to a δ-potential located at the origin. The relative Hamiltonian of two particles in 2D interacting via a δ-potential is also equivalent, so by means of (2.3), there is a mapping from the 3-body interaction for 3 particles in 1D to the 2-body interaction for 2 particles in 2D. Since the virial coefficients b_n are determined by the n-body problem, the existence of such a mapping suggests a relationship between b_3 for our 1D system and b_2 in the 2D system.[9]

In Ref. [66], the relationship between the virial coefficients is laid out in detail. In particular, given their identical[10] Hamiltonians, it must be the case that $\mathcal{Q}^{\text{rel}}_{1,1,1} = \mathcal{Q}^{\text{rel,2D}}_{1,1}$, where subscripts denote the particle content by flavor. It is convenient to only consider the deviation of the interacting problem from the noninteracting one, which we denote by $\Delta\mathcal{Q} = \mathcal{Q} - \mathcal{Q}^{(0)}$. Then, $\Delta\mathcal{Q}_3 = \Delta\mathcal{Q}_{1,1,1}$, since contributions to $\mathcal{Q}_3$ containing more than one particle of a given flavor, such as $\mathcal{Q}_{2,1,0}$, are unaffected by the three-body interaction. Similarly, $\Delta\mathcal{Q}^{\text{2D}}_2 = \Delta\mathcal{Q}^{\text{2D}}_{1,1}$. Now, given the separability of the relative and c.m. Hamiltonians in both problems, the partition functions are the product of their respective relative and c.m. partition functions, and we have $\Delta\mathcal{Q}_3 = \mathcal{Q}^{\text{c.m.}}_{1,1,1}\Delta\mathcal{Q}^{\text{rel}}_{1,1,1}$ and $\Delta\mathcal{Q}^{\text{2D}}_2 = \mathcal{Q}^{\text{c.m.,2D}}_{1,1}\Delta\mathcal{Q}^{\text{rel,2D}}_{1,1}$ (the interactions are absent from the c.m. Hamiltonians). From the initial equality of the relative partition functions, we can finally relate

$$\Delta\mathcal{Q}_3 = \frac{\mathcal{Q}^{\text{c.m.}}_{1,1,1}}{\mathcal{Q}^{\text{c.m.,2D}}_{1,1}}\Delta\mathcal{Q}^{\text{2D}}_2. \tag{2.18}$$

After the manipulations above, we still need to relate (2.18) to the virial coefficients. Writing $\Delta b = b - b^{(0)}$ as we did for the ΔQ's, we have (from matching the Taylor series coefficients)

$$\Delta\mathcal{Q}_3 = \mathcal{Q}_1\Delta b_3 \tag{2.19}$$

in 1D and

$$\Delta\mathcal{Q}^{\text{2D}}_2 = \mathcal{Q}^{\text{2D}}_1\Delta b^{\text{2D}}_2 \tag{2.20}$$

[9] Higher virial coefficients in the 1D and 2D systems are not expected to share a direct relationship, as additional particles break the correspondence between the two systems.

[10] See Appendix B.

in 2D. Combining all of the above, we arrive at the desired relationship,

$$\Delta b_3 = \frac{\mathcal{Q}_{1,1,1}^{\text{c.m.}}}{\mathcal{Q}_{1,1}^{\text{c.m.,2D}}} \frac{\mathcal{Q}_1^{\text{2D}}}{\mathcal{Q}_1} \Delta b_2^{\text{2D}}. \tag{2.21}$$

Each of the prefactors can be simply evaluated (see Appendix B), giving the direct proportionality

$$\Delta b_3 = \frac{1}{\sqrt{3}} \Delta b_2^{\text{2D}}. \tag{2.22}$$

From the Beth-Uhlenbeck formula [66, 76, 77, 78], we have the exact expression

$$\Delta b_2^{\text{2D}} = e^{\beta \varepsilon_B} - \int_0^\infty \frac{dy}{y} \frac{2e^{-\beta \varepsilon_B y^2}}{\pi^2 + 4 \ln^2 y}, \tag{2.23}$$

providing a way to evaluate Δb_3 and access the complete thermodynamics of the three-body problem in 1D. With the variable substitution $u = y^2$ in Eq. (2.23), the integral takes on a known form [69], such that

$$\Delta b_3 = \frac{\nu\left(\beta \varepsilon_B\right)}{\sqrt{3}}, \tag{2.24}$$

where

$$\nu(x) \equiv \int_0^\infty dt \ \frac{x^t}{\Gamma(t+1)}. \tag{2.25}$$

Noting that $\nu(x)$ resembles a continuous version of the Taylor series of e^x (integral rather than sum), it is tempting to compare the two functions. In fact, as shown in Fig. 2.2, e^x approximates $\nu(x)$ remarkably well for $x \gtrsim 2$.

Section 2.5: Hubbard-Stratonovich transformation and approximations of the pressure

So far, we have treated the three-body problem in terms of wave functions. To make further progress towards the many-body problem, however, we must turn to second quantization. In particular, the Hamiltonian (2.1) is written in second-quantized form as

$$\hat{H} = \sum_{\sigma=1}^{3} \int dp \ \frac{p^2}{2} \ \hat{a}_\sigma^\dagger(p) \hat{a}_\sigma(p) + g \int dx \ \hat{n}_1(x) \hat{n}_2(x) \hat{n}_3(x), \tag{2.26}$$

where $\hat{a}_\sigma^\dagger(p)$ and $\hat{a}_\sigma(p)$ are the fermionic creation and annihilation operators of species σ at momentum p, and $\hat{n}_\sigma(x) = \hat{a}_\sigma^\dagger(x) \hat{a}_\sigma(x)/L$ is the spatial density operator at position x.

Following Ref. [66], we cast the problem on a spacetime lattice and discretize Eq. (2.26); our goal is to

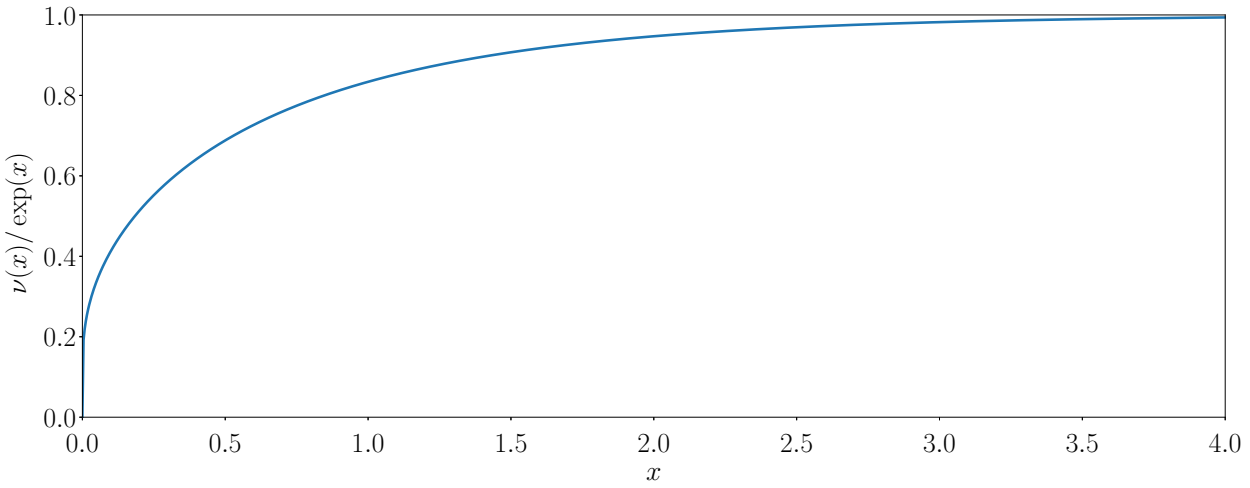

Figure 2.2: $\nu(x)$ is well approximated by e^x for $x \gtrsim 2$, providing a simple way of evaluating Δb_3 at strong coupling.

arrive at a path integral formulation of the partition function. With the imaginary time (inverse temperature) discretized as $\beta = \tau N_\tau$, where N_τ is the number of temporal lattice sites and τ is the spacing between them, we have

$$e^{-\beta \hat{H}} = \prod_{i=1}^{N_\tau} e^{-\tau \hat{H}}. \tag{2.27}$$

The benefit of this expansion derives from a Trotter-Suzuki decomposition [79]—a form of Baker-Campbell-Hausdorff formula—which enables a separation of the kinetic and potential operators inside the exponential:

$$e^{-\tau \hat{H}} = e^{-\tau \hat{T}/2} e^{-\tau \hat{V}} e^{-\tau \hat{T}/2} + \mathcal{O}\left(\tau^3\right), \tag{2.28}$$

where $\hat{T}$ and $\hat{V}$ are the kinetic and potential terms of the Hamiltonian, respectively. As the kinetic terms are diagonal in momentum space, we focus on the potential terms,

$$e^{-\tau \hat{V}} = \prod_x e^{-\tau g \hat{n}_1(x)\hat{n}_2(x)\hat{n}_3(x)}. \tag{2.29}$$

As fermionic operators, the $\hat{n}_\sigma$ are idempotent, so that

$$e^{-\tau g \hat{n}_1 \hat{n}_2 \hat{n}_3} = 1 + \left(e^{-\tau g} - 1\right) \hat{n}_1 \hat{n}_2 \hat{n}_3. \tag{2.30}$$

While we have exchanged an exponentiated operator for a linear one, it is still a three-body operator. With a Hubbard-Stratonovich transformation, though, we may separate this three-body operator into multiple

one-body operators.

The central idea of Hubbard-Stratonovich transformations is to decouple n-body operators into one-body operators by introducing one (or more) scalar fields, which must then be integrated out [80]. Despite the formality of this description, the core of the transformation is nothing more than a mathematical identity which (usually) involves a Gaussian integral [81]. For example, upon completing the square and shifting the integration variable, we have the following identity:

$$\int_{-\infty}^{\infty} d\sigma \; e^{-\sigma^2 - 2a\sigma(x+y)} = \sqrt{\pi} e^{-a^2(x+y)^2}, \tag{2.31}$$

for some real parameter a and variables x and y. If x and y are idempotent operators, then Eq. (2.31) can be rearranged to yield

$$e^{-2a^2 xy} = \frac{1}{\sqrt{\pi}} \int_{-\infty}^{\infty} d\sigma \; e^{-\sigma^2 + (a^2 - 2a\sigma)(x+y)}. \tag{2.32}$$

We thus see that in this example, we have bought the separation $xy \to x + y$ for the price of an integral. When applied to each potential term in the product (2.27), the various $d\sigma$ contributions coalesce into the path integral measure $\mathcal{D}\sigma = \prod_{i=1}^{N_\tau} d\sigma_i$.

In our case, while the idea is essentially the same, we do not employ a Gaussian integral. Instead, we have [66]

$$e^{-\tau g \hat{n}_1 \hat{n}_2 \hat{n}_3} = \frac{1}{3\pi} \int_{\Gamma} d\sigma \; \prod_{i=1}^{3} \left[1 + B\hat{n}_i f(\sigma)\right], \tag{2.33}$$

where $B^3 = \frac{64}{15}\left(e^{-\tau g} - 1\right)$, $f(\sigma) = e^{i2\sigma/3}\cos^2\sigma$, and $\Gamma = [-3\pi/2, 3\pi/2]$. Unfortunately, due to the complex exponential in $f(\sigma)$, this transformation does not yield a positive-definite weight for potential energy. As a result, the "phase problem" prevents this form from being used effectively in Monte Carlo calculations, where a real, positive-definite sampling distribution is required.[11]

Although the complex phase in $f(\sigma)$ is problematic for stochastic methods, we may still find a use for Eq. (2.33). Writing the partition function as

$$\mathcal{Z} = \int \mathcal{D}\sigma \; e^{-S[\sigma]} = \int \mathcal{D}\sigma \; \det{}^3 M[\sigma], \tag{2.34}$$

where $M[\sigma]$ is the fermion matrix [66], the effective action $S[\sigma] = -3 \ln \det M[\sigma]$ may be expanded in powers

[11] Fixed-node methods [82], as well as complex Langevin [83, 84], may be able to treat the complex weight; we do not employ either in this work.

of B [85]. Keeping only the leading term,

$$\ln\left(\mathcal{Z}/\mathcal{Z}_0\right) = N_\tau N_x \ln\left[\int_\Gamma \frac{d\sigma}{3\pi} e^{3KBf(\sigma)}\right], \tag{2.35}$$

where

$$K = \frac{1}{N_x}\sum_p \frac{ze^{-\beta p^2/2}}{1+ze^{-\beta p^2/2}}. \tag{2.36}$$

As outlined in Appendix C, the integral in (2.35) may be carried out exactly, yielding

$$\ln\left(\mathcal{Z}/\mathcal{Z}_0\right) = N_\tau N_x \ln\left[{}_2F_4\left(\frac{1}{6},\frac{5}{6};\frac{1}{4},\frac{1}{2},\frac{3}{4},1;\frac{1}{2}\left(\frac{9KB}{8}\right)^3\right)\right], \tag{2.37}$$

where ${}_2F_4$ is a hypergeometric function. Given (2.13), Eq. (2.37) provides an approximation to the pressure:

$$\beta V\left(P-P_0\right) = \ln\left(\mathcal{Z}/\mathcal{Z}_0\right), \tag{2.38}$$

where P_0 is the noninteracting pressure. In Fig. 2.3, the resulting pressure is plotted alongside the pressure computed from the virial expansion.

Section 2.6: Summary

In this chapter, we introduced the 1D three-body problem, showing that a bound state—the trimer—forms for arbitrarily small attractive coupling strengths, breaking the classical scale invariance. In doing so, we showed that this breaking of scale invariance constitutes the same SO(2,1) scaling anomaly as seen in the well-studied 2D two-body problem. Through this correspondence, we established a relationship between the first non-trivial virial coefficients of the two systems, providing a first glimpse at the many-body properties of the three-body interaction. Having laid out the properties of the three-body contact interaction for the simplest non-trivial case of three particles, we will now aim to study the same interaction for increasing numbers of particles.

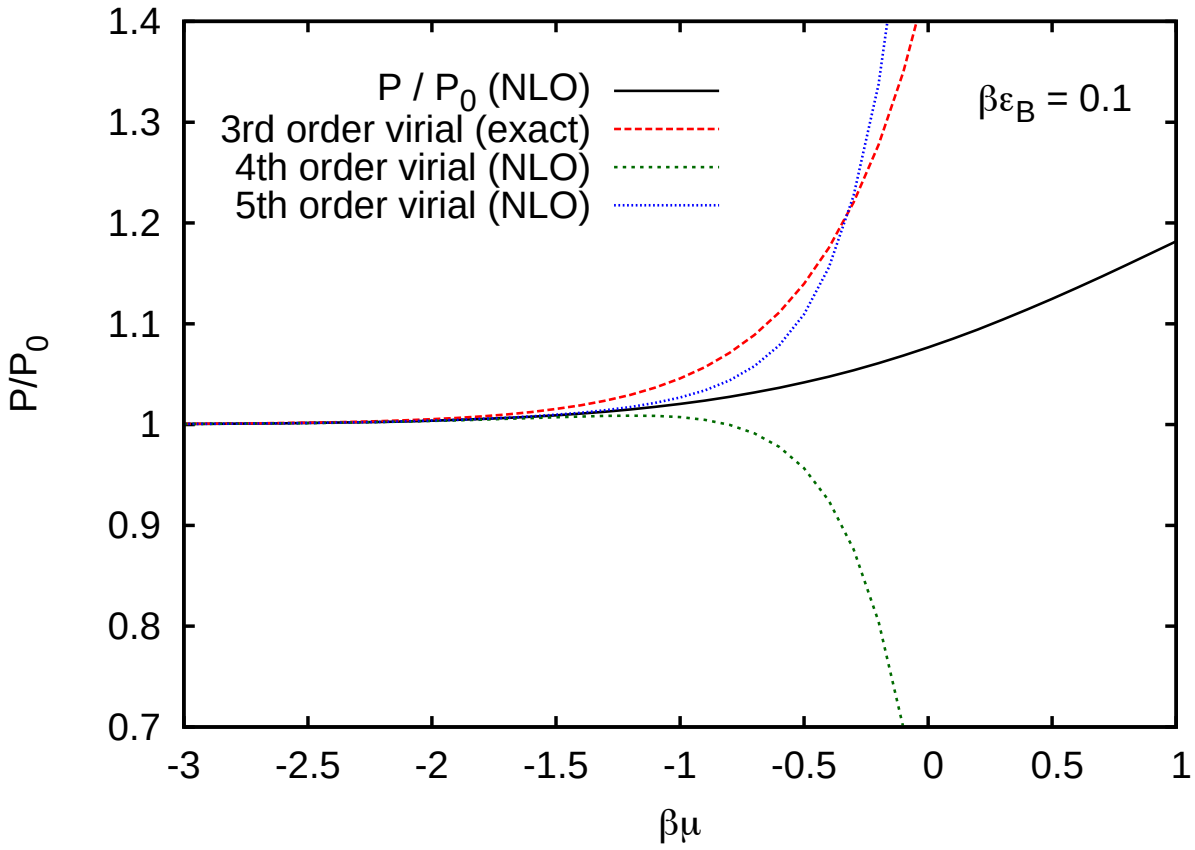

Figure 2.3: Approximate results for the pressure of the three-body attractive interaction as a function of the chemical potential, provided by both perturbation theory and the virial expansion. Reproduced from [66].

CHAPTER 3: INTEGRAL EQUATIONS FOR FEW-BODY WAVE FUNCTIONS

Our aim in this chapter is to build a bridge between the exact three-body solution of Ch. 2 and the general many-body problem because, to quote Ref. [11], "Systems of a few quantum particles form a natural link between one-, two-body physics and the many-body physics." Each domain requires a different approach, so we must first develop a few-body formalism: While 1D systems with two-body interactions can be solved by the Bethe Ansatz [86], the three-body interaction invalidates that method here.

In the typical position-space representation, the Schrödinger equation is a differential equation. Fourier transforms are routinely employed to convert differential equations into algebraic equations, and for the three-body problem of Chapter 2, Fourier transformation indeed achieved this goal. There, the δ-potential was easily integrated, yielding momentum conservation and an integral over the wave function which amounted to a constant. Things are not so simple for less trivial cases, however.

As soon as a fourth particle is added, the three-body interaction may include only one of two identical fermions at a time; the other fermion takes on the role of a spectator. As in the three-body case, the integral over the wave function absorbs the momentum dependence of the three interacting particles. The spectator, however, retains its momentum dependence in the wave function. Thus, instead of becoming algebraic equations, Schrödinger equations containing $N > 3$ particles become integral equations. In the following sections, we will show that while these integral equations are complex, it is not necessary to solve the whole N-dimensional wave function. Instead, it suffices to consider only the behavior of the $N - 3$ spectator particles. Still, given the exchange symmetry obeyed by spectators and interacting particles of the same species, this is no trivial task, and we will often discretize the problem to make progress by numerical methods.

Section 3.1: Mathematical background

To provide context and appreciation for the difficulty of the integral equations in this work, we here briefly examine the relevant mathematical theory of integral equations. In particular, we will highlight common methods of solution and point out why these fail for the equations of interest.

The general form of the integral equations we will encounter is the Fredholm integral equation of the

second kind,

$$f(x) = g(x) + \lambda \int_a^b K(x,y) f(y)\ dy, \tag{3.1}$$

where $K(x,y)$ is the integral kernel, $g(x)$ is known, and $f(x)$ is the desired solution. When $g(x) \neq 0$, the equation is inhomogeneous, and a series solution may be employed. To see this, consider Eq. (3.1) rewritten as

$$f(x) = \left(\mathbb{1} - \hat{K}\right)^{-1} g(x), \tag{3.2}$$

where $\hat{K}$ represents the integral operator, $\lambda \int_a^b dy\ K(x,y)$. In the discrete case where $\hat{K}$ is an $n \times n$ matrix, if the appropriate norm $||K|| < 1$, then the (geometric) series

$$(\mathbb{1} - K)^{-1} = \sum_{n=0}^{\infty} K^n \tag{3.3}$$

converges [87]. The continuous analog is nearly identical [88], with the matrix product replaced by iterated applications of the integral operator, $\hat{K}$, where we again must have $||\hat{K}|| < 1$. Unfortunately, there are two complications that immediately preclude the usage of this "Neumann series" solution. First, the integral operators stemming from the 3-body interaction are unbounded [89], with $||\hat{K}|| \to \infty$. Second, the equations we encounter are homogenous, with $g(x) = 0$. As a result, even if $\left(\mathbb{1} - \hat{K}\right)^{-1}$ *were* invertible by (3.3), Eq. (3.2) would vanish identically. While stochastic methods exist for solving Fredholm integral equations of the second kind [90, 91, 92], they fail for the same reasons as the Neumann series.

For integral kernels that depend only on the difference of the arguments, as $K(x,y) = K(x-y)$, Eq. (3.1) is readily solved by Fourier or Laplace transformation. In that case, the integral is a convolution, and we have [93]

$$\mathcal{L}\left[K * f\right] = \mathcal{L}\left[K\right] \mathcal{L}\left[f\right], \tag{3.4}$$

where the $*$ denotes convolution and $\mathcal{L}$ the transform. The integral kernels we encounter, however, do not have this property. Similarly, methods of solution that rely on the symmetry and/or separability of the kernel do not apply in any case we study [94, 95].

Other failed attempts at solving these integral equations include series expansions, contour integration, changes of variable, integration by parts, and Feynman parametrization. Numerical results suggest potential localized singular behavior, which may partially explain the failure of some of these methods, as several rely on the smoothness of the integrated function for their validity. While we do not apply it in this work, Refs. [96, 97] describe a promising stochastic method for ground-state studies.

Section 3.2: Symmetrized Fourier expansion

As is well known from the spin-statistics theorem [98], bosons (particles with integer spin) are symmetric under particle exchange, while fermions (particles with half-integer spin) are antisymmetric. Whenever a quantum system is described theoretically, this exchange symmetry must be accounted for. In field theory language, (anti)commutators enforce exchange symmetry: For bosonic fields $\phi(x)$, $\phi^\dagger(x)$, the canonical commutation relations are

$$[\phi(x), \phi(y)] = \left[\phi^\dagger(x), \phi^\dagger(y)\right] = 0, \ \left[\phi(x), \phi^\dagger(y)\right] = \delta(x-y), \tag{3.5}$$

while for fermionic fields $\psi(x)$, $\psi^\dagger(x)$, the anticommutation relations read

$$\{\psi(x), \psi(y)\} = \left\{\psi^\dagger(x), \psi^\dagger(y)\right\} = 0, \ \left\{\psi(x), \psi^\dagger(y)\right\} = \delta(x-y). \tag{3.6}$$

When working with wave functions, exchange symmetry is captured by

$$\psi(x,y) = \pm\psi(y,x), \tag{3.7}$$

where the plus (minus) sign holds for bosons (fermions).

Since the current approach is in terms of wave functions, Eq. (3.7) is more relevant. Typically, exchange symmetry in wave functions is only applied *after* solving the Schrödinger equation: A nonsymmetric solution is found, and linear combinations of the solution that obey Eq. (3.7) are constructed. As we demonstrate below, however, exchange symmetry may be accounted for from the outset by taking advantage of the orthogonality of symmetric and antisymmetric subspaces with respect to the inner product.

The essential idea is similar to the fact that if a function is known to have even (odd) parity, its Fourier series may be limited to cosine (sine) basis functions (Fig. 3.1). The cosine and sine subspaces are orthogonal to one another, and as a result, any pure cosine series will be orthogonal to any pure sine series. While the restriction to even (odd) basis functions may be viewed as merely a convenient trick, it may conversely serve to *enforce* a given parity. In fact, calculating the Fourier cosine (sine) series of a function that is *not* of a definite parity is equivalent to projecting the function onto the symmetric (antisymmetric) subspace. The full Fourier series always acts as an identity operator; the Fourier cosine and sine series only do so when acting on functions of their same parity.

Now, consider a set of orthonormal basis functions $e_i(x)$, where i runs over the dimension of the space

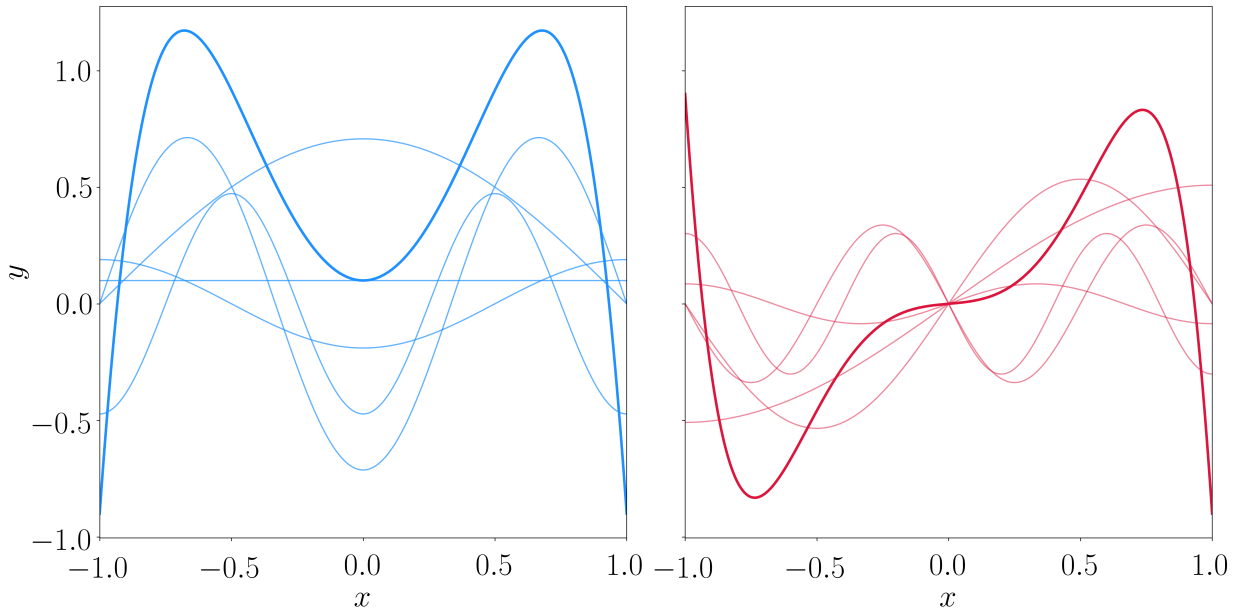

Figure 3.1: Even (left) and odd (right) functions with their first five Fourier components (faint), demonstrating that when the parity is definite, the basis functions share the same parity.

under consideration. A two-particle wave function such as (3.7) can then be expanded as

$$\psi(x,y) = \sum_{i,j} c_{ij} e_i(x) e_j(y), \tag{3.8}$$

with $\langle e_i,\ e_j\rangle \equiv \int dx\ e_i^*(x)e_j(x) = \delta_{ij} \implies \sum_{i,j} |c_{ij}|^2 = 1$. From the basis functions, construct the symmetrized linear combinations

$$e_{ij}^{\pm}(x,y) = \frac{1}{2}\big[e_i(x)e_j(y) \pm e_j(x)e_i(y)\big], \tag{3.9}$$

which may be shown to obey

$$\big\langle e_{ij}^{+},\ e_{mn}^{-}\big\rangle = 0, \tag{3.10}$$

$$\big\langle e_{ij}^{\pm},\ e_{mn}^{\pm}\big\rangle = \frac{1}{2}\Big[\delta_{im}\delta_{jn} \pm \delta_{in}\delta_{jm}\Big]. \tag{3.11}$$

Note that the symmetric and antisymmetric basis functions are orthogonal to one another and that

$$e_i(x)e_j(y) = e_{ij}^{+}(x,y) + e_{ij}^{-}(x,y). \tag{3.12}$$

Suppose that $\psi(x,y) = \psi(y,x)$, which implies $c_{ij} = c_{ji}$. Inserting (3.12) into (3.8) yields

$$\psi(x,y) = \sum_{i,j} c_{ij} \left[e^+_{ij}(x,y) + e^-_{ij}(x,y) \right] = \sum_{i,j} c_{ij} e^+_{ij}(x,y), \tag{3.13}$$

where the $e^-_{ij}(x,y)$ terms drop out because $c_{ij}e^-_{ij}(x,y) = c_{ji}e^-_{ji}(x,y) = -c_{ij}e^-_{ij}(x,y) = 0$, where the Einstein summation convention has been used along with the symmetry and antisymmetry of c_{ij} and $e^-_{ij}(x,y)$, respectively. When $\psi(x,y) = -\psi(y,x)$, the $e^+_{ij}(x,y)$ terms drop out instead, revealing that the symmetrized basis functions are sufficient to expand bosonic and fermionic wave functions. More importantly, expanding a function in terms of the symmetrized basis functions *guarantees* that the function will have the desired exchange symmetry.

While the preceding discussion focused on two-particle wave functions, the reasoning may be extended to an arbitrary number of particles by forming symmetrical permutations of the basis functions. For fermions, the basis function for an N-particle state becomes

$$\prod_{k=1}^{N} e_k(x_k) \to \frac{1}{N!} \sum_{k_1,k_2,\ldots,k_N=1}^{N} \epsilon_{k_1 k_2 \ldots k_N} e_1(x_{k_1}) e_2(x_{k_2}) \ldots e_N(x_{k_N}), \tag{3.14}$$

where $\epsilon_{k_1 k_2 \ldots k_N}$ is the N-dimensional Levi-Civita tensor. Equation (3.14) may be seen as a Slater determinant of the original basis functions (in the Leibniz form); for bosons, the Levi-Civita tensor is replaced by its totally symmetric analog, which turns the determinant into a "permanent."

With δ-function interactions, it is most convenient to express the Schrödinger equation in momentum space. The N-body spatial wave function ψ can thus be Fourier transformed by symmetrizing the plane wave states as described above, automatically yielding a momentum-space wave function ϕ that is bosonic or fermionic.[1]

Section 3.3: A technique for reducing dimensionality

The three-body problem was solvable thanks to a clever choice of coordinates applied in the zero-momentum frame. However, straightforward appplication of the same ideas when the particle number $N > 3$ fails immediately: Jacobi coordinates do not accomodate the particle exchange symmetry that now must be obeyed, nor do they treat the multiple interaction terms on equal footing. Since the size of the Hilbert space of a given problem grows exponentially with N, finding a way to reduce the complexity of obtaining

[1] The Hamiltonian operator and subsequent algebraic manipulations (and even the unsymmetrized inverse Fourier transform) leave the exchange symmetry intact.

the wave function is of the utmost importance. Fortunately, the exchange symmetry of identical particles provides a degree of redundance that we may exploit.

The central idea is that for any given interaction configuration, three particles of different flavors will act as a trimer, while the other particles will be spectators. The wave function should reflect this and feature products of trimer wave functions with spectator wave functions,

$$\phi \sim \sum \phi_{\text{trimer}} \phi_{\text{spectators}}, \tag{3.15}$$

where the sum is over permutations of identical particle exchanges. Since the form of ϕ_{trimer} is known from the three-body problem, only $\phi_{\text{spectators}}$ is unknown, reducing the dimension of the problem by three. Furthermore, the functional form of $\phi_{\text{spectators}}$ must be the same for all identical particle permutations. The similarity of the present approach to that of Refs. [46, 45, 99, 30] is evident in Eq. (3.15).

From here on out, we label the particular problem by its particle content, $N_1 + N_2 + N_3$. For example, $2+1+1$ refers to two particles of one flavor and one particle of each of the other two flavors. To illustrate the technique, we here outline the fermionic $2+1+1$ solution.[2] Consistent with (3.15), we anticipate that the unknown function $\phi_{\text{spectator}}$ will have only one argument, whereas the full wave function ϕ has four.

The Hamiltonian of the $2+1+1$ system reads

$$H_{211} = \frac{1}{2m}\left(p_1^2 + p_2^2 + k^2 + q^2\right) + g\big[\delta(x_1 - y) + \delta(x_2 - y)\big]\delta(y - z), \tag{3.16}$$

where x, y, and z (p, k, and q) represent the positions (momenta) of flavors 1, 2, and 3, respectively; subsequently, we take $m = 1$. For the two identical particles, we employ the antisymmetric Fourier representation for the wave function,

$$\psi(x_1, x_2, y, z) = \frac{1}{(2\pi)^4}\int dp_1 dp_2 dk dq\ \frac{1}{2}\left(e^{ip_1x_1}e^{ip_2x_2} - e^{ip_2x_1}e^{ip_1x_2}\right)e^{iky}e^{iqz}\phi(p_1, p_2, k, q), \tag{3.17}$$

where the two distinct particles follow the ordinary Fourier transform. After inserting (3.17) into the Schrödinger equation and transforming[3] to momentum space (primed variables), we arrive at, for the inter-

[2]This problem is the three-body analog of the two-body interacting problem studied in Ref. [100].

[3]The inverse transform need not be symmetrized.

action terms,

$$\frac{g/(2\pi)^4}{2}\int dp_1 dp_2 dk dq\ \phi(p_1,p_2,k,q)\times \\ \int dx_1 dx_2\ \left(e^{ix_1(p_1-p_1')}e^{ix_2(p_2-p_2')} - e^{ix_1(p_2-p_1')}e^{ix_2(p_1-p_2')}\right)\left(e^{ix_1(k+q-k'-q')} + e^{ix_2(k+q-k'-q')}\right), \quad (3.18)$$

where the δ-functions have been integrated out. The second line of (3.18) evaluates to

$$(2\pi)^2\big[\delta(p_1+k+q-p_1'-k'-q')\delta(p_2-p_2') + \delta(p_1-p_1')\delta(p_2+k+q-p_2'-k'-q') \\ - \delta(p_2+k+q-p_1'-k'-q')\delta(p_1-p_2') - \delta(p_2-p_1')\delta(p_1+k+q-p_2'-k'-q')\big], \quad (3.19)$$

reflecting the two possible interaction configurations as well as their fermionic exchanges. In each term, the total momentum of the reactants is conserved, as is the individual momentum of the spectator. Inserting (3.19) into (3.18), integrating the spectator δ-functions, and dropping the subscripts on the p_i (since they are just integration variables at this point),

$$\frac{g/(2\pi)^2}{2}\int dp dk dq\ \times \\ \big[\phi(p,p_2',k,q) - \phi(p_2',p,k,q)\big]\delta(p+k+q-p_1'-k'-q') \\ + \big[\phi(p_1',p,k,q) - \phi(p,p_1',k,q)\big]\delta(p+k+q-p_2'-k'-q'). \quad (3.20)$$

Now, choosing the center-of-momentum frame, $p+p_i+k+q = p_1'+p_2'+k'+q' = 0$ (subscript i stands for 1 or 2), allows us to rewrite the above as

$$\frac{g/(2\pi)^2}{2}\int dp dk dq\ \times \\ \big[\phi(p,p_2',k,q) - \phi(p_2',p,k,q)\big]\delta(p+p_2'+k+q) \\ + \big[\phi(p_1',p,k,q) - \phi(p,p_1',k,q)\big]\delta(p_1'+p+k+q), \quad (3.21)$$

where it becomes clear that each term depends on only one primed variable (p, k, and q are integrated out). So, while we do not yet know the exact functional form of one of these terms, we can say that it is *some* function of just one variable. Denoting this function by f, the above simplifies to

$$\frac{g/(2\pi)^2}{2}\big[f(p_2) - f(p_1)\big], \quad (3.22)$$

where

$$f(x) = \int dpdkdq \ \big[\phi(p,x,k,q) - \phi(x,p,k,q)\big]\delta(p+k+q+x). \tag{3.23}$$

Dropping all primes, the Schrödinger equation (in momentum space) now reads

$$\frac{1}{2}\left(p_1^2 + p_2^2 + k^2 + q^2\right)\phi(p_1,p_2,k,q) + \frac{g/(2\pi)^2}{2}\big[f(p_2) - f(p_1)\big] = E\phi(p_1,p_2,k,q), \tag{3.24}$$

or, rearranging,

$$\phi(p_1,p_2,k,q) = \frac{-g/(2\pi)^2}{T-E} \times \frac{1}{2}\big[f(p_2) - f(p_1)\big], \tag{3.25}$$

where T stands for the total kinetic energy. Strictly speaking, the left-hand side should properly be $\frac{1}{2}\big(\phi(p_1,p_2,k,q) - \phi(p_2,p_1,k,q)\big)$ at this point. However, for a wave function ϕ that is antisymmetric in p_1 and p_2—which ours is, given the Fourier representation—this is equal to just $\phi(p_1,p_2,k,q)$. Moreover, the right-hand side explicitly shows the antisymmetry.

Now, we need to find out what the function f is. By substituting the expression for ϕ in terms of f into the one for f in terms of ϕ, we obtain

$$f(x) = -\frac{g}{(2\pi)^2}\int dp\ dk\ dq\ \frac{1}{T-E}\big[f(x) - f(p)\big]\delta(x+p+k+q). \tag{3.26}$$

This is now an implicit integral equation for f which, in its current form, cannot be solved. With periodic boundary conditions and/or a spatial lattice, however, the integrals become discrete sums. The discrete form of (3.26) can be cast as a matrix equation and solved by exact diagonalization, but such an approach becomes much more expensive numerically once more particles are added, so iteration is preferable.

As shown in Appendix D, most of the integrals in (3.26) can be carried out analytically, yielding the continuum, free-space form as

$$f(x)\left[\ln\left(4x^2+6\epsilon\right) + 2\gamma\right] = -\int dp\ \frac{f(p)}{\sqrt{\left(p+\frac{x}{3}\right)^2 + \frac{2}{9}\left(4x^2+6\epsilon\right)}}, \tag{3.27}$$

where all variables are in appropriate units of ϵ_B, $\epsilon = -E/\epsilon_B$, and γ is the Euler-Mascheroni constant. Even without the solution of Eq. (3.27), we may still gain insight by inspecting the features of the integral kernel. First, notice that the coupling g does not appear anywhere—the only scale present is the trimer binding energy,[4] ϵ_B. Second, the kernel takes the form of the square-root of a Breit-Wigner distribution [101]

[4]This assumes that the integral converges with infinite bounds. If f does not tend to zero (or oscillate) at large momenta, the integral must be regulated by the cutoff Λ, and g will again appear.

centered at $x = -3p$ with a width related to the energy of the system. We thus see that the kernel embodies the exchange symmetry of the identical fermions: the center of the distribution corresponds to zero total momentum, where the free fermion's momentum is multiplied by three to balance the momentum of the trimer. As a homogeneous Fredholm integral equation of the second kind with infinite bounds and an asymmetric, non-separable kernel, Eq. (3.27) does not submit to any presently known method of solution; we now proceed with the discretized form[5] of Eq. (3.26).

Notice that the function f is fully determined up to an overall scale—multiplying f by a constant has no effect on its defining equation—and the energy, E. Since the wave function must be normalized, however, f will share the same normalization factor, and we obtain a sort of eigenvalue equation for the energy. Excluding overall constants (which are just absorbed into the normalization),[6] the quantity we need is

$$|\phi(p_1, p_2, k, q)|^2 \propto \frac{1}{(T-E)^2}\big[f^2(p_1) + f^2(p_2) - 2f(p_1)f(p_2)\big], \tag{3.28}$$

which will be integrated over all momentum variables. Considering this integration, the two squared terms will give the same contribution, so we can relabel the p_2 integration variable to p_1 and combine them. Then, dropping the overall factor of 2 now present, the final normalization condition is

$$\int dp_1\ dp_2\ dk\ dq\ \frac{f(p_1)}{(T-E)^2}\big[f(p_1) - f(p_2)\big]\ \delta(p_1 + p_2 + k + q) = 1. \tag{3.29}$$

Similar derivations can be carried out for additional particles; the corresponding expressions are collected in Table 3.3. Recognizing that Eq. (3.29) can alternatively be written as

$$\int dp_1\ dp_2\ dk\ dq\ \frac{f(p_1)}{T-E}\ \phi(p_1, p_2, k, q)\ \delta(p_1 + p_2 + k + q) = 1, \tag{3.30}$$

we note that *all* systems' normalizations share this form (with additional arguments of f and ϕ as necessary) and omit them from Table 3.3.

[5]The authors of Ref. [46] use a discrete approximation of the Fredholm determinant [102] of their analog to Eq. (3.27) to find the spectrum of the bosonic problem. We were unable to find a stable bound state for that problem by our approach; it is also not immediately clear how one would relate such a solution to the discretized form of Eq. (3.26).

[6]Dropping constants is valid for the normalization, but the prefactor $-g/(2\pi)^2$ *must* remain in the implicit equation for f—this is where the coupling dependence enters the problem.

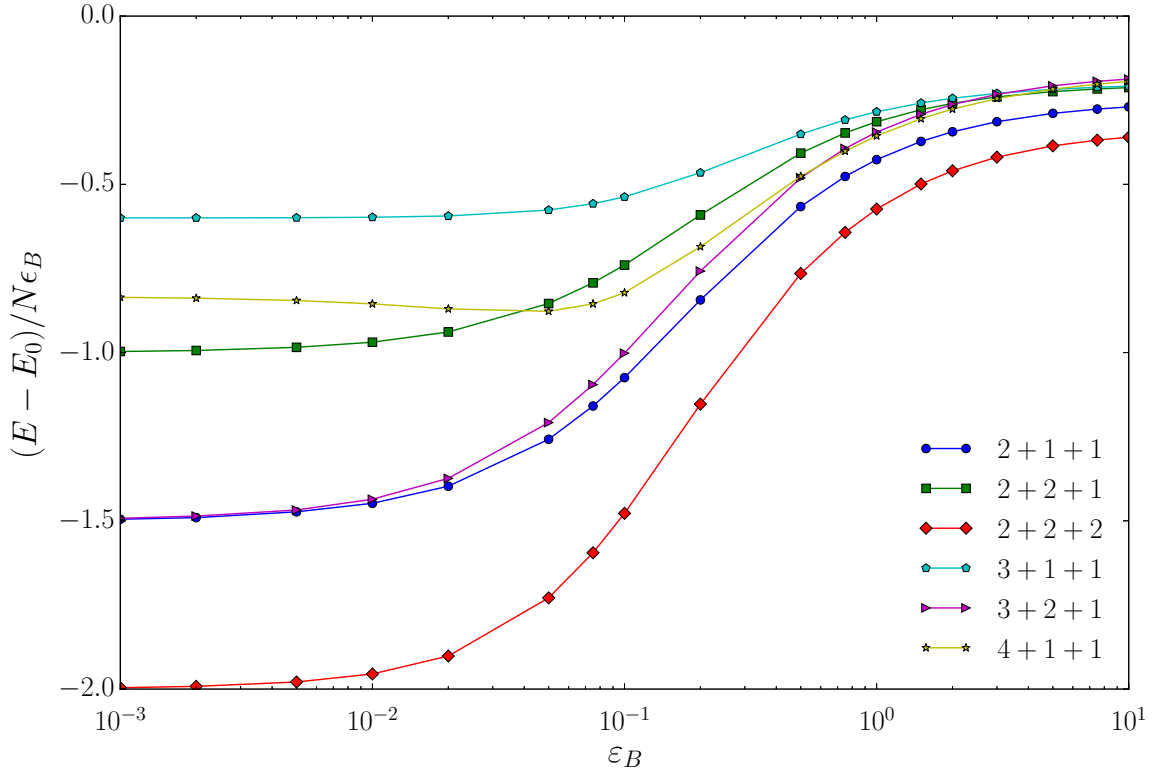

Figure 3.2: Few-body energies from the small- to large-coupling limits (E_0 indicates the noninteracting ground-state energy).

Table 3.1: Wave functions and auxiliary functions for various systems. The collective index $(p_1 p_2 u)$, appearing in sums in the third column, indicates a summation over cyclic permutations of p_1, p_2, u as the first three arguments of ϕ, which correspond to like-flavor fermions. All f expressions are summed over u and v. The variable ς is the negation of all other momenta in each system to ensure zero total momentum, and the operators $\hat{P}_{ij}$ exchange arguments i and j in the wave function. Modified from [103].

System	ϕ	f summand
2+1+1	$-\dfrac{g/L^2}{T-E}\displaystyle\sum_i (-1)^i f(p_i)$	$\dfrac{1}{2!}(1-\hat{P}_{up})\phi(u,p,v,\varsigma)$
2+2+1	$-\dfrac{g/L^2}{T-E}\displaystyle\sum_{i,j} (-1)^{i+j} f(p_i,k_j)$	$\dfrac{1}{(2!)^2}\left(1-\hat{P}_{up}\right)\left(1-\hat{P}_{vk}\right)\phi(u,p,v,k,\varsigma)$
3+1+1	$-\dfrac{g/L^2}{T-E}\displaystyle\sum_{i,j,k} \epsilon_{ijk} f(p_i,p_j)$	$\dfrac{1}{3!}\displaystyle\sum_{(p_1p_2u)} \phi(p_1,p_2,u,v,\varsigma)$
2+2+2	$-\dfrac{g/L^2}{T-E}\displaystyle\sum_{i,j,k} (-1)^{i+j+k} f(p_i,k_j,q_k)$	$\dfrac{1}{(2!)^3}\left(1-\hat{P}_{up_1}\right)\left(1-\hat{P}_{vk_1}\right)\left(1-\hat{P}_{\varsigma q_1}\right)\phi(u,p_1,v,k_1,\varsigma,q_1)$
3+2+1	$-\dfrac{g/L^2}{T-E}\displaystyle\sum_{i,j,k,l} (-1)^l \epsilon_{ijk} f(p_i,p_j,k_l)$	$\dfrac{1}{3!\cdot 2!}\displaystyle\sum_{(p_1p_2u)}\left(1-\hat{P}_{vk_1}\right)\phi(u,p_1,p_2,v,k_1,\varsigma)$
4+1+1	$-\dfrac{g/L^2}{T-E}\displaystyle\sum_{i,j,k,l} \epsilon_{ijkl} f(p_j,p_k,p_l)$	$\dfrac{1}{4!}\left\{1-\left[1-\left(1-\hat{P}_{up_3}\right)\hat{P}_{up_2}\right]\hat{P}_{up_1}\right\}\phi(u,p_1,p_2,p_3,v,\varsigma)$

Section 3.4: Boundary conditions and limits

As detailed previously, integral equations in free, continuous space like Eq. (3.27) are intractable. In the absence of exact solutions, then, we can make progress by choosing suitable boundary conditions. With periodic boundary conditions, the 1D space becomes a ring of length L (which replaces factors of 2π in the previous section), and the momentum integrals become discrete sums: $p \to 2\pi n/L$, with n integer. The momentum cutoff Λ still applies, which restricts the discrete momentum values to a finite number. Since the dimension of the Hilbert space is independent of the chosen basis, the finitude of momentum space also applies to position space. The continuum limit thus corresponds to an increasing number of spatial support points around the ring, which coincides with the $\Lambda \to \infty$ limit. Because attractive forces lead to enhanced localization, the continuum limit becomes more difficult to reach as the interaction becomes stronger. Conversely, a fairly small Λ is sufficient to capture continuum behavior for weak couplings.

An important point to notice is that, by imposing periodic boundary conditions, we have introduced a length scale (L), whereas the only length scale in the free-space problem is dictated by the trimer binding energy. To free ourselves of the scale L, then, we must ensure that the spatial extent of the system under study is much smaller than L. Such localization occurs in the strong coupling limit $\varepsilon_B \gg 1$ and may be seen schematically as

$$\sum_{n,m} \frac{\cdots}{n^2 + m^2 + \ldots + \alpha\varepsilon_B} = \sum_{n,m} \frac{\varepsilon_B^{-1} \cdots}{n^2\varepsilon_B^{-1} + m^2\varepsilon_B^{-1} + \ldots + \alpha} \to \int dp\, dk\, \frac{\cdots}{p^2 + k^2 + \ldots + \alpha}, \tag{3.31}$$

where $\alpha \sim \mathcal{O}(1)$. As ε_B grows, the integer momentum values approximate continuous variables, and the integral equations seen previously are recovered. Thus, while exact solutions in free space remain elusive, we may approach them by solving the discrete problem and examining the simultaneous limits $1 \ll \varepsilon_B \ll \Lambda^2$.

Having seen that the discrete strong-coupling limit approximates the free-space problem, one may wonder: What of the weak-coupling limit? The apparent[7] answer is that the problem in free space is equivalent *at all couplings*. Since its integral equations may be cast in totally dimensionless form, with the only parameter being a ratio of energies, the system is simply rescaled by a change in the coupling. However, the weak-coupling limit *is* meaningful on the periodic ring. There, the size of the ring, L, imposes an infrared momentum cutoff, Λ_{IR}, which determines the minimum possible (nonzero) value of kinetic energy. The three-body binding energy may thus be made small in comparison to this minimum kinetic energy when more than three fermions are present. Since $L \to \infty$ in free space, however, $\Lambda_{\mathrm{IR}} \to 0$, and the binding energy and kinetic energy may both take on arbitrarily small values.

[7] If the integral equations (such as Eq. (3.27)) must be regulated by Λ to converge, this argument may be invalid.

Section 3.5: Numerical method

By substituting the expressions from the second column of Table 3.3 into those of the third column, the discrete analogues of Eq. (3.26) are obtained for all systems with up to six particles. These implicit summation equations form the basis of the iterative approach employed in this work, which we now examine in detail.

In each case, a lattice size $L = \ell N_x$ must be chosen (N_x is the number of lattice sites; we take the lattice spacing $\ell = 1$), which determines the size of the Hilbert space and fixes $\Lambda = \frac{1}{2}(L-1)$.[8] A three-body binding energy must also be chosen to fix the interaction strength; we write this quantity in dimensionless form as $\varepsilon_B = \dfrac{\epsilon_B L^2}{4\pi^2}$. The coupling g corresponding to the given length L and binding energy ε_B is then obtained according to Eq. (2.9).

The function f is stored in an $(N-3)$-dimensional array, where each dimension has N_x entries (N is the number of particles in the system); we initialize f by applying the expressions of the third column of Table 3.3 to an antisymmetrized, uniform wave function ϕ. We iteratively apply the discrete analogues of Eq. (3.26) to f, where, following the Gauss-Seidel method [87], updated values of f are used as soon as they are computed. This choice speeds up convergence compared to the Jacobi method, where one would build the subsequent iteration f_{i+1} by sweeping over the entire f_i array before updating its values.

With any iterative procedure, if the magnitude of the array is changed during an update, these changes will compound over many iterations. As a result, the computed values may become too large or too small, leading to numerical breakdown. To avoid this issue, we normalize the array f with the corresponding wave function normalization after each update. As noted previously, since the defining equations are insensitive to overall constants, this procedure has no effect on the functional form of f and is only a practical convenience.[9]

After a few thousand iterations, we begin to search for energy eigenvalues by measuring the wave function normalization constructed from f after updating the array, but *before* normalizing it. Only f arrays built with valid energy eigenvalues will be fixed points of the wave function normalization under application of the implicit summation equations. The condition of being equal to unity, as seen in Eq. (3.29), is not essential; rather, the normalization simply must not *change* after an update. We exploit this fact by constructing and iterating over many f arrays for various proposed energy values and finding those energy values which lead to fixed points. In practice, we have observed that there is a minimum energy eigenvalue beyond which the normalization changes as a monotonic function of the energy; this minimum energy corresponds

[8] Using an odd number of lattice sites N_x includes zero-momentum modes while maintaining left/right symmetry.

[9] While the wave function normalization was used in this work, any reasonable normalization applied after each update would achieve the same effect.

to the ground state. Once an energy eigenvalue is converged to a desired tolerance (regarding iterations as well as increasing N_x), the f array associated with this energy may be used to reconstruct the complete momentum-space wave function, from which all observables may be computed.

Finally, let us note a potential pitfall. The equations for f obtained from Table 3.3 sometimes display (anti)symmetry in their arguments in a way that suggests simplification. As a toy example, consider the equation

$$f(x,y) = \sum_z f(x,z) - f(z,x) - f(z,y) + f(y,z). \tag{3.32}$$

In this case, it is true that $f(y,x) = -f(x,y)$, making it tempting to simplify the equation to

$$f(x,y) = \sum_z 2f(x,z) - 2f(z,y). \tag{3.33}$$

While this equation *is also true* for solutions of (3.32), it contains less information and is less restrictive. If the iterative procedure is carried out without the complete information contained in the first version, the solution obtained will satisfy (3.33), but it may *not* satisfy (3.32).

Section 3.6: Weak-coupling expansion

Although the three-body problem is inherently nonperturbative, at weak couplings, the few-body problem can be described as a perturbation on the corresponding noninteracting problem. With periodic boundary conditions, the three distinct fermions of the trimer are each free to occupy the zero-momentum mode. The kinetic energy thus remains very small at weak coupling, where the trimer is large and diffuse. As soon as a fourth particle is added, however, fermionic antisymmetry dictates that at least one nonzero momentum state must be occupied. As a result, the kinetic energy becomes the dominant contribution to the total energy:

$$E = E_0 - \epsilon, \tag{3.34}$$

where E_0 is the energy of the corresponding noninteracting problem, and the deviation $\epsilon \ll E_0$ is of the order of the trimer binding energy ϵ_B.

If one attempts ordinary perturbation theory—calculating the expectation value of the interaction, $\hat{H}_I$, for noninteracting states, $|\alpha_0\rangle$, as $\langle\alpha_0|\hat{H}_I|\alpha_0\rangle$—the results will not align with the numerical data. There are multiple noninteracting ground states, but they are not equivalent under the interaction. Some ground state wave functions even vanish where the interaction saturates and do not experience any change in energy. As a result, degenerate perturbation theory becomes necessary.

The only relevant states—noninteracting ground states—have energy E_0. Given (3.34), the propagator term $(T-E)^{-1}$ becomes simply ϵ^{-1}. In the limit $\epsilon_B \to 0^+$, Eq. (2.9) reduces to

$$-\frac{g}{L^2} \approx \epsilon_B, \tag{3.35}$$

such that the discrete version of (3.26) simplifies to

$$f(x) = \frac{\epsilon_B}{\epsilon} \sum_{p,k,q \in \{E_0\}} \big[f(x) - f(p)\big]\delta(x+p+k+q), \tag{3.36}$$

where the sum is restricted to noninteracting ground-state momentum values. Now, as a tractable matrix equation, Eq. (3.36) may be solved by exact diagonalization.[10] Written in matrix form, we have [103]

$$\begin{pmatrix} 3 & -2 & -1 \\ -2 & 4 & -2 \\ -1 & -2 & 3 \end{pmatrix} \begin{pmatrix} f(-1) \\ f(0) \\ f(1) \end{pmatrix} = \frac{\epsilon}{\epsilon_B} \begin{pmatrix} f(-1) \\ f(0) \\ f(1) \end{pmatrix}, \tag{3.37}$$

with the eigenvalues $\epsilon = 6\epsilon_B$ and $\epsilon = 4\epsilon_B$.[11] The results of this procedure for all systems studied here are presented alongside the iterative data in Fig. 3.3, showing perfect agreement in all cases in the limit of weak coupling.

The eigenvectors of (3.37) (and its analogs) allow for the complete determination of the functional form of the wave function at weak coupling [103]. For instance, in the ground state ($\epsilon = 6\epsilon_B$), the eigenvector requires that $f(-1) = f(1) = -\frac{1}{2}f(0)$. Equation (3.36) then establishes

$$f(p) = \sqrt{2}\Big[\delta(p-1) - 2\delta(p) + \delta(p+1)\Big], \tag{3.38}$$

which, when combined with (3.25), determines the spatial wave function:

$$\psi\left(x_1, x_2, y, z\right) = \frac{1}{\sqrt{2}L^2}\left[\cos\left(\frac{2\pi(x_2-y)}{L}\right) + \cos\left(\frac{2\pi(x_2-z)}{L}\right) - \cos\left(\frac{2\pi(x_1-y)}{L}\right) - \cos\left(\frac{2\pi(x_1-z)}{L}\right)\right]. \tag{3.39}$$

The spatial density associated with this wave function, as well as that of the excited state ($\epsilon = 4\epsilon_B$) are plotted in Fig. 3.4, revealing a distinctive difference in structure. In the ground state, three particles exist as

[10] While only the 4-body problem examined here may be efficiently treated with matrices at all energy scales, all systems studied in this work have a small enough number of noninteracting ground states to be treated this way in the weak-coupling limit.

[11] The third eigenvalue, $\epsilon = 0$, is inconsistent with the initial assumption of $\epsilon > 0$. Systems with more particles feature more null eigenvalues, which only reflect redundancy in the defining equations of f.

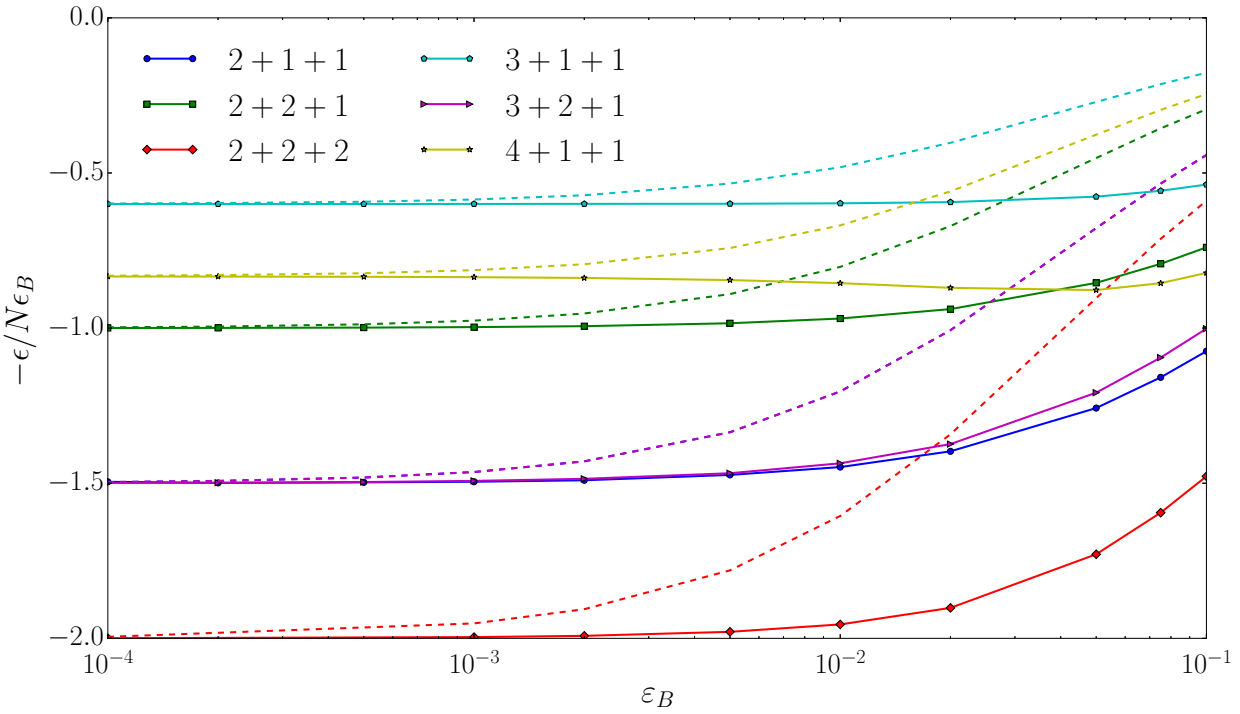

Figure 3.3: Few-body energies compared to degenerate perturbation theory (dashed curves) at weak coupling.

a diffuse trimer, while the fourth particle is repelled as far away as possible. In the excited state, however, all four particles aggregate around a central location, suggesting a four-body molecular state. Space-filling models of these two structures are presented in Fig. 3.5.

Section 3.7: Strong-coupling expansion

In the limit of strong attraction, three fermions of different flavors will bind tightly into a localized trimer. Any individual fermion will be repelled from the trimer by the Pauli Exclusion Principle. Since the number of fermions in the trimer is odd, though, the trimers themselves will act as composite fermions, analogously to three fermionic quarks forming a fermionic nucleon.

With periodic boundary conditions, when one tightly bound trimer forms, it acts as an impenetrable barrier, effectively severing the periodic ring into a linear interval with hard walls. While the trimer still may possess kinetic energy, its mass is three times larger than that of the other particles in the system, as long as a second trimer cannot form. As such, at leading order in the ratio of particle mass to trimer mass—$\lambda = 1/3$—the trimer may be treated as stationary, and the problem becomes equivalent to that of

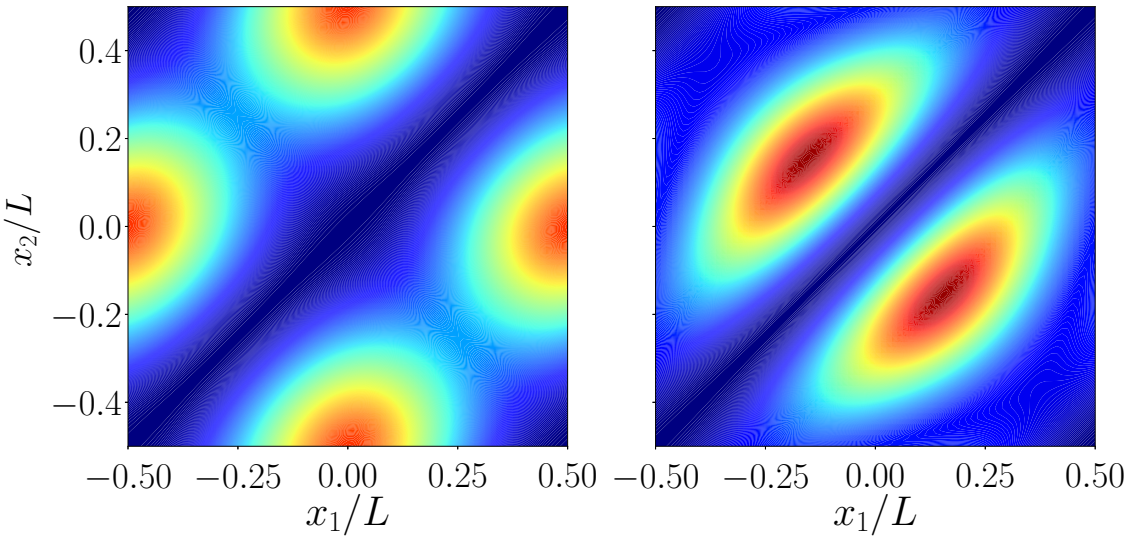

Figure 3.4: Ground (left) and excited (right) state spatial densities of the two identical fermions in the $2+1+1$ system at weak coupling, where one unique fermion is fixed at the origin and the other is integrated out. Red (blue) indicates high (low) density.

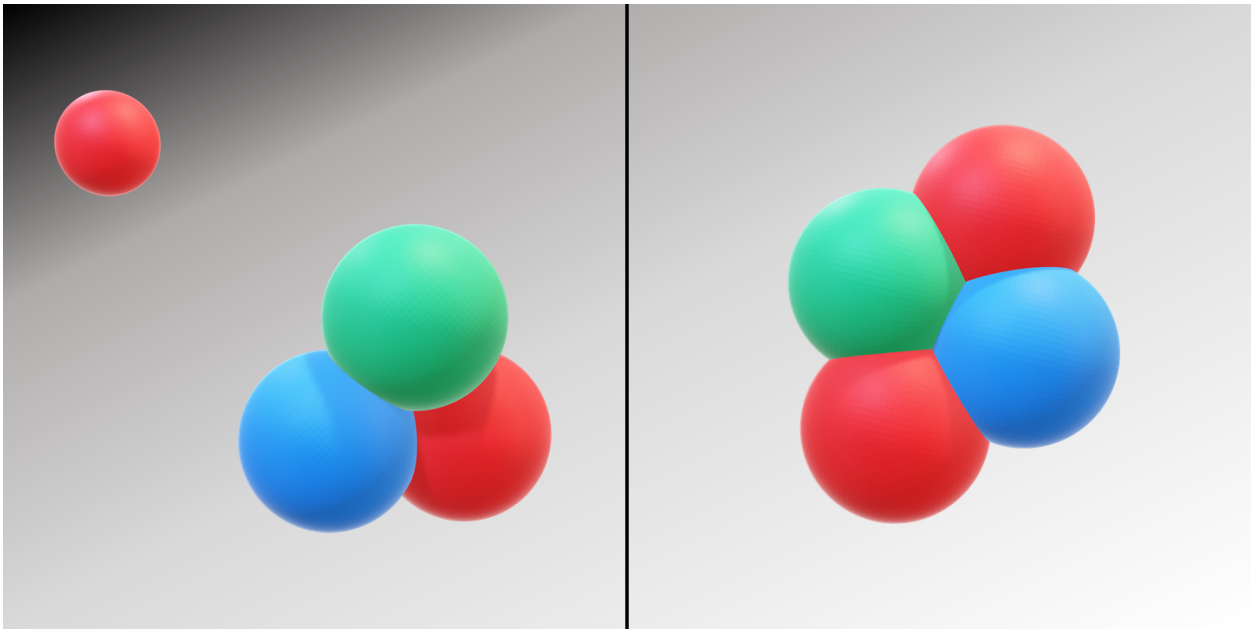

Figure 3.5: Molecular structures corresponding to the density distributions of Fig. 3.4. In the ground state (left), the system forms a trimer and an isolated fermion. In the excited state (right), the system forms a single tetramer molecule.

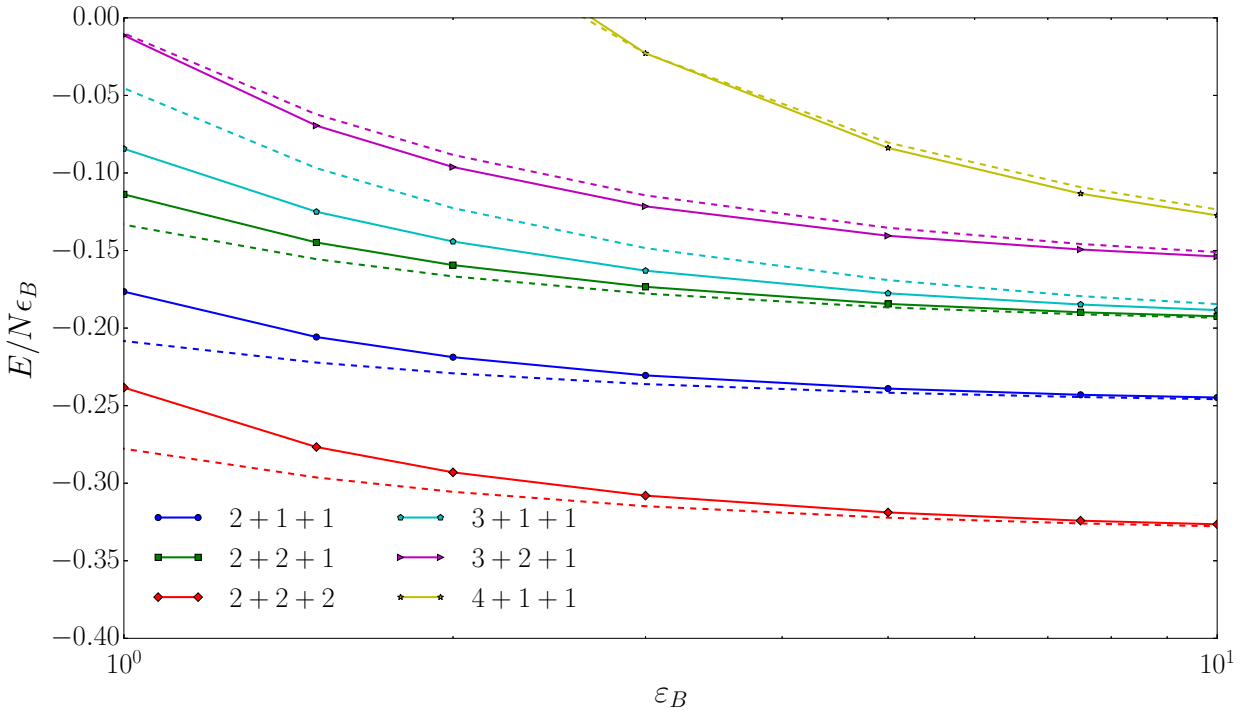

Figure 3.6: Few-body energies compared to "particle-in-a-box" approximation (dashed curves) at strong coupling.

the "particle in a box," with the effective Hamiltonian [103]

$$\hat{H}_{\text{eff}} = \frac{1}{2m}\left(\hat{p}^2_{\text{unbound}} + \lambda \hat{p}^2_{\text{trimer}}\right) - \epsilon_B. \tag{3.40}$$

After constructing the antisymmetrized, noninteracting hard-wall box states $|\alpha\rangle$, the first-order correction to the energy $E^{(1)}$ is given by

$$E^{(1)} = \frac{\lambda}{2m}\langle\alpha|\hat{p}^2_{\text{trimer}}|\alpha\rangle\,. \tag{3.41}$$

When the system comprises two complete trimers, it should instead be treated as two fermions of mass $3m$. The comparison of numerical results to the particle-in-a-box approximation is presented in Fig. 3.6, demonstrating a remarkably strong agreement for a simple first-order approximation in λ. This quantitative agreement directly supports the idea that compact, composite fermions form at strong coupling.

Section 3.8: Molecular structure and the absence of a bound hexamer state

In a previous section, we determined the spatial wave function through a suitable approximation at weak coupling. As the method employed here gives access to the complete momentum-space wave function, though,

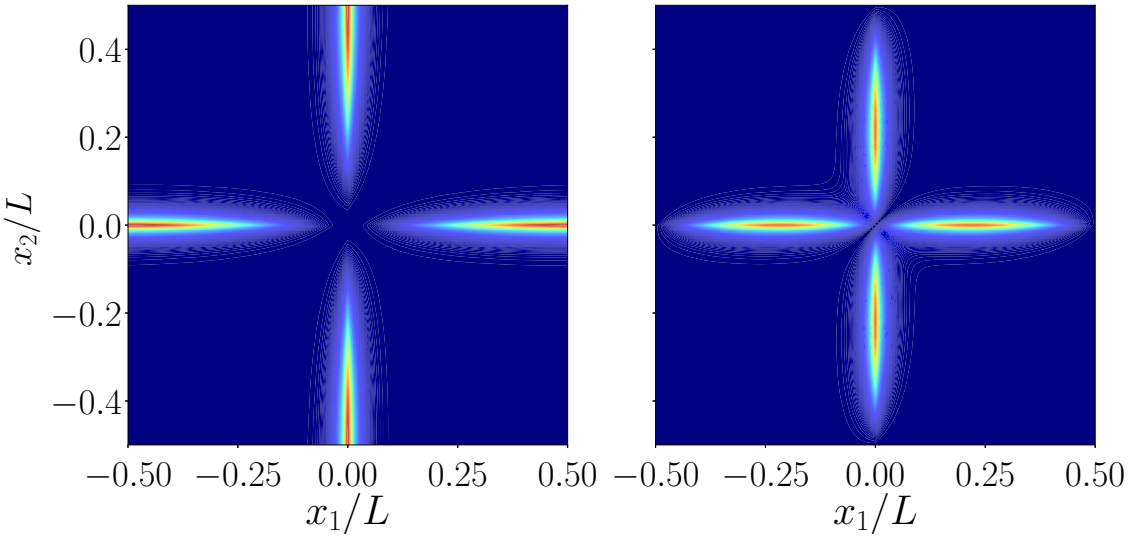

Figure 3.7: Ground (left) and excited (right) state spatial densities of the two identical fermions in the 2+1+1 system at strong coupling, where one unique fermion is fixed at the origin and the other is integrated out. Red (blue) indicates high (low) density.

we may obtain the spatial wave function numerically at *any* coupling strength by Fourier transformation. Examining the resulting density distributions then gives insight as to how the relative positions of particles evolve as a function of the interaction strength.

At weak coupling, the 2+1+1 system displayed different spatial structures in the ground and first excited states (Figs. 3.4 and 3.5). Although the ground state tended to exist in a configuration of a trimer and an isolated particle, it had some probability of being found in a tetramer-like state (the light-blue gaps between high-density regions in Fig. 3.4, left); similarly, the first excited state preferred existing as a tetramer, but could also be found as a trimer plus an isolated particle (the yellow-green tips of the high-density regions in Fig. 3.4, right).

In contrast, at strong coupling ($\varepsilon_B = 20$), the system becomes rigidly fixed, and the tetramer structure disappears altogether. Figure 3.7 shows the analogous densities, revealing a strong asymmetry between the two identical fermions. In the ground state (left), one of the two is tightly bound to the trimer center, while the other tends to be as far away as possible. In the excited state (right), while the excluded fermion does tend to be closer to the trimer center than in the ground state, there is still a clear division into trimer plus isolated particle. As the attraction grows from weak to strong, then, the tetramer ejects one of the identical fermions to enable a more tightly bound trimer with the remaining fermion.

While the spatial densities of the other few-body systems can also be obtained in this way, the compu-

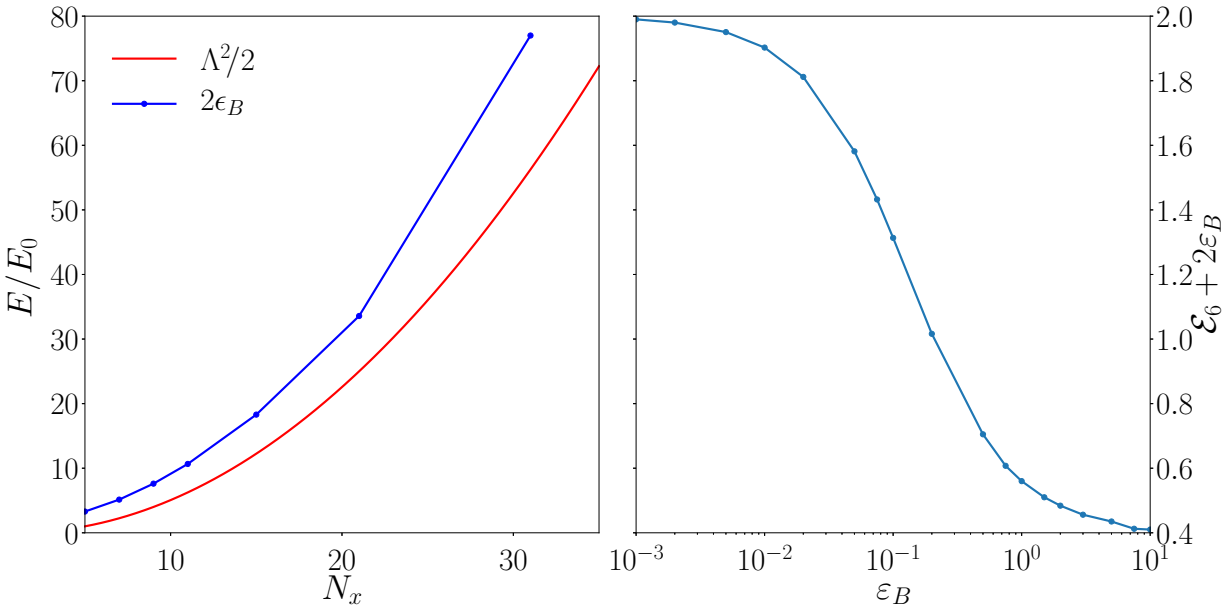

Figure 3.8: Left: Hexamer bound-state energy at threshold (in units of noninteracting problem), showing incompatibility with the lattice cutoff energy and divergence in the continuum limit. Right: Relative energies of six-body system and two isolated trimers across various couplings, showing that the trimer-trimer interaction is repulsive. Modified from [103].

tational cost increases significantly with each additional particle. Rather than constructing the full wave function of the $2+2+2$ system (with its N_x^6 entries), we will examine other quantifiers to gain information about its structure. The $2+2+2$ system is particularly interesting because it is the first case in which two complete trimers may form. The question then arises, do the six particles differentiate into two distinct trimers, rather than forming a six-body bound state? If so, what is the nature of the interaction between the two trimers?

The appearance of a six-body bound state would be marked by an energy $\mathcal{E}_6 = E_6 \left(L/2\pi\right)^2$ *lower* than the energy of two isolated trimers at the same interaction strength, as this would indicate a mutual attraction between the trimers (or some other bound configuration). The threshold for the appearance of a bound "hexamer" state is then $\mathcal{E}_6 = -2\varepsilon_B$ (recall the sign convention on ε_B); numerically, then, we can simply *force* the system's energy to have the threshold value and then solve for the corresponding coupling strength. The result of this procedure, displayed in Fig. 3.8, shows that no bound hexamer state exists. In the left panel of Fig. 3.8, the system's threshold energy is plotted alongside the kinetic energy associated with the UV momentum cutoff. The fact that the six-body energy is *higher* than the cutoff energy means that the numerical solution is unphysical (recall the discussion in Ch. 1 on lattice resolution and frequency sampling). Perhaps even more troubling is the fact that the threshold energy diverges in the continuum limit (large

N_x), whereas all other (physically valid) systems studied in this way converge.

In the right panel of Fig. 3.8, instead of forcing the system to take on the threshold energy value, we present the difference in energy between the six-body system and two isolated trimers for valid physical solutions from weak to strong coupling. The six-body energy is always greater than the two-trimer energy, again indicating that a bound hexamer does not form. These results, combined with the accuracy of the two-trimer approximation in Fig. 3.6, provide strong evidence for the formation of trimers that act as composite fermions.[12] Confirmation of this behavior in the many-body case, however, requires additional study.

Section 3.9: Excited states

For systems where exact diagonalization is feasible—such as the $2+1+1$ system seen previously—excited states are found at the same time as the ground state. For most systems of interest, however, this is not the case. As a remedy, we introduce an iterative method to extract excited states based on Gram-Schmidt orthogonalization. While this approach does avoid exact diagonalization, each successive excited state carries a higher computational cost.

Gram-Schmidt orthogonalization is a standard procedure for generating a set of orthonormal vectors. Starting from a set of non-orthogonal vectors, one selects one vector as the base case and normalizes it to yield $\mathbf{e}_1$. One then chooses a second vector $\mathbf{v}_2$ and computes its projection onto the first, then subtracts this projection:

$$\mathbf{e}_2 \propto \mathbf{v}_2 - \mathbf{e}_1 \left(\mathbf{v_2} \cdot \mathbf{e}_1\right), \tag{3.42}$$

where $\mathbf{e}_2$ is assumed to be normalized. This process is repeated for all the vectors in the set, where each subsequent vector must have its projections onto all previous vectors subtracted.

Given that eigenstates of the Hamiltonian are orthogonal, it is possible to incorporate Gram-Schmidt orthogonalization into the iterative process described in previous sections. The key is to recognize that Eqs. (3.23) and (3.25) apply to *all* valid energy eigenstates. Then, by removing the projection onto the ground state as

$$\phi_1 = \tilde{\phi} - \phi_0 \left\langle \tilde{\phi} | \phi_0 \right\rangle, \tag{3.43}$$

where $\tilde{\phi}$ is a guess state, (3.43) may be inserted into (3.23) to reveal

$$f_1(x) = \tilde{f}(x) - I f_0(x), \tag{3.44}$$

[12] In Cooper pairing, since each dimer contains two fermions, the exchange symmetry of two dimers is bosonic. In the present system, since each trimer contains *three* fermions, the exchange symmetry of two trimers is fermionic.

where $I \equiv \langle\tilde{\phi}|\phi_0\rangle$. Taking advantage of (3.25), we may write

$$I = \frac{g^2}{64\pi^4}\int dp_1 dp_2 \left[\tilde{f}(p_2) - \tilde{f}(p_1)\right]\left[f_0(p_2) - f_0(p_1)\right]W(p_1,p_2), \tag{3.45}$$

where

$$W(p_1,p_2) = \int dk\ dq\ \frac{\delta(p_1+p_2+k+q)}{(T-\tilde{E})(T-E_0)} \tag{3.46}$$

may be calculated without prior knowledge of f. Thus, once the ground state f_0 is known, it may be incorporated into a new iterative process whereby the guess state $\tilde{f}$ will converge to the first excited state f_1 as $\tilde{E} \to E_1$ and $I \to 0$. This procedure may be repeated for higher excited states, where the projection onto all previously found states must be subtracted, making each additional state more difficult to obtain.

Section 3.10: Trimer dissociation by repulsive two-body forces

While two-body forces may be tuned to be weaker than three-body forces in experiments, they may not be entirely absent [37, 104, 64]. As a result, the competition between these interactions is of interest. In particular, the question of dissociation of a trimer by repulsive two-body forces merits investigation.

With the Hamiltonian

$$H = -\frac{1}{2}\left(\frac{\partial^2}{\partial x^2} + \frac{\partial^2}{\partial y^2} + \frac{\partial^2}{\partial z^2}\right) + g_3\delta(x-y)\delta(y-z) + g_2\Big[\delta(x-y) + \delta(y-z) + \delta(z-x)\Big], \tag{3.47}$$

the procedure of previous sections may be applied to express the momentum-space wave function as

$$\phi(p,k,q) = -\frac{g_3/L^2}{T-E}\left(c + \lambda\Big[f(p) + f(k) + f(q)\Big]\right), \tag{3.48}$$

where $\lambda \equiv g_2 L/g_3$, the constant $c = \int dp\ f(p)$, and f is given by the implicit equation

$$f(p) = -\frac{g_3}{L^2}\int dk\ dq\ \frac{\delta(p+k+q)}{T-E}\left(c + \lambda\Big[f(p) + f(k) + f(q)\Big]\right). \tag{3.49}$$

As a function of only one variable, f may be solved by exact diagonalization. We do so for $L = 201$ and $\varepsilon_B = 10$, over a range of attractive and repulsive two-body interactions λ.

Figure 3.9 (left) shows the energy of the three-body system with two- and three-body forces relative to the binding energy in the absence of two-body forces. As expected, the trimer becomes more deeply bound with attractive two-body interactions ($\lambda > 0$), while repulsive two-body interactions ($\lambda < 0$) cause its energy

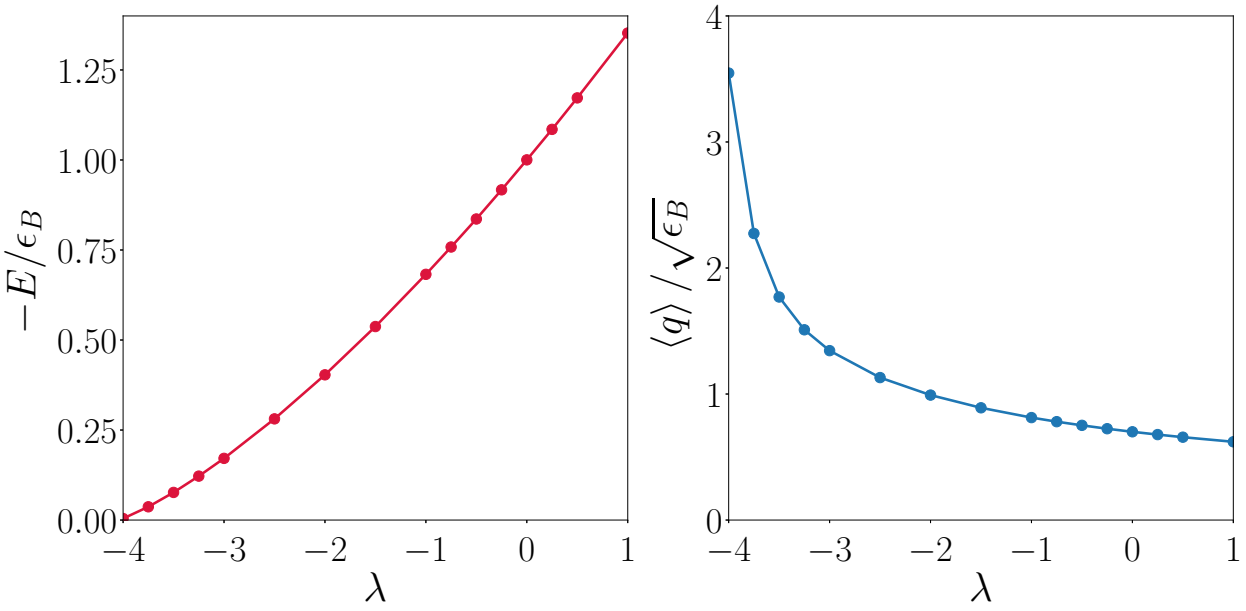

Figure 3.9: Left: Ratio of trimer energies with and without two-body forces, where increasingly repulsive two-body interactions (negative λ) cause the trimer energy to approach zero. Right: Trimer hyperradius with two-body forces, where two-body repulsion causes the trimer to expand.

to rise. At $\lambda \simeq -4$, the trimer dissociates as its energy approaches zero.[13] As the trimer approaches the dissociation threshold, it grows rapidly, as reflected by the sharp increase in the hyperradius in the right panel of Fig. 3.9.

We may also observe the dissociation of the trimer by studying the spatial wave function, which we may again obtain upon solving for f. To visualize the spatial density information contained in the wave function, we fix one of the three particles at the origin[14] and plot

$$\rho_{\text{rel}} = \frac{|\psi_\lambda(x, y, 0)|^2}{|\psi_0(x, y, 0)|^2}, \tag{3.50}$$

where ψ_0 indicates the case without two-body forces.

With $\lambda > 0$, we expect an increase in the density ρ_{rel} at the origin, as both types of interactions benefit from a more compact trimer. In Fig. 3.10 (left), such a tightening of the trimer is indeed seen but is also accompanied by a perhaps unexpected accumulation in other regions. In particular, compared to the case with $\lambda = 0$, attractive two-body forces increase the likelihood that the three particles are maximally

[13] The precise value of λ at which dissociation occurs varies with system size L. While we have not yet carried out a systematic finite-size analysis, our results may be compared to those of Refs. [45, 43].

[14] The periodic boundary conditions, with the translation invariance they provide, make this choice completely general.

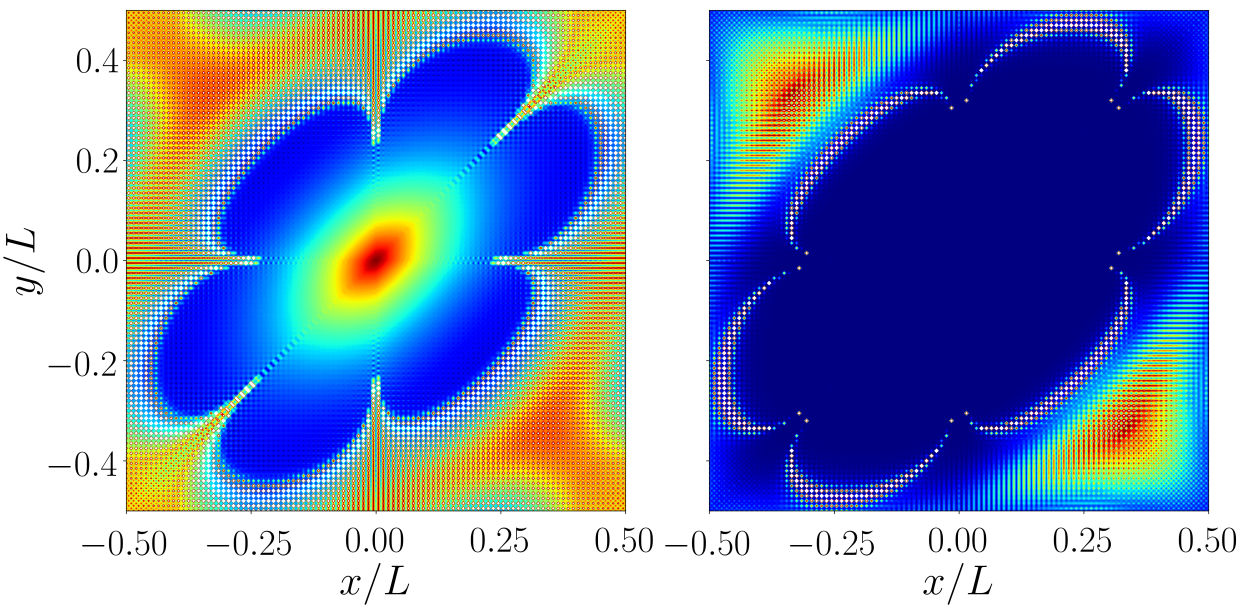

Figure 3.10: Densities of the three-body problem with attractive (left; $\lambda = 1$) and repulsive (right; $\lambda = -4$) two-body forces relative to the density with no two-body force. The two axes represent two particle positions, while the third is fixed at $z = 0$. Note that the color gradations follow an exponential scale, where red is large and blue is small.

separated.

With repulsive two-body forces, on the other hand, a maximal separation of the three particles is not surprising. Figure 3.10 (right), which depicts the trimer on the verge of dissociation, shows a high tendency towards such separation (indicated by the red triangular regions at the corners along the anti-diagonal). Importantly, there is a stark depletion of density at the origin, where the trimer was previously situated.

Both attractive and repulsive two-body forces exhibit the curious formation of six crescent-shaped lobes which, together, give the appearance of a flower (Fig. 3.10). These regions reflect the six possible orderings of the three particles when the central particle is approximately equidistant from the other two, but not maximally separated. The changes in density relative to the $\lambda = 0$ case associated with these lobes characterize the competition between two- and three-body forces.

Section 3.11: Summary

In this chapter, by incorporating new analytical and numerical methods, we have extended the solution of the three-body interacting problem to the cases of four, five, and six particles. The formalism we introduced facilitated approximations at both weak and strong coupling that agreed extremely well with the numerical results.

With access to the full wave function, we were able to probe structural information, highlighting the $2+1+1$ system of four particles. In that system, the ground state across all coupling strengths indicated the formation of a bound trimer plus an excluded, lone fermion. The formation of trimers was further indicated by the $2+2+2$ system, where we found that two trimers repel one another rather than forming a bound hexamer.

At this stage, we postulate that in the many-body problem, the three-component Fermi gas with attractive three-body interactions will form a gas of composite trimers that interact repulsively. Confirmation of this prediction, however, requires an entirely new approach to the problem, as the methods of this chapter fail for large particle numbers. Before exploring that topic, we will briefly examine this model in the presence of a harmonic oscillator potential.

CHAPTER 4: A FEW COLD ATOMS IN A HARMONIC TRAP

Unlike in free space, the classical three-body problem in a harmonic oscillator potential *does* have a characteristic length scale, governed by the trap frequency ω. Despite this difference, the trapped quantum problem shares many similarities with the free quantum case, such as a close correspondence with the 2D two-body problem.

While the trap potential preserves rotational invariance—$\mathbf{r} \cdot \mathbf{r} = \mathbf{r}' \cdot \mathbf{r}'$, where primes denote rotated coordinates—it manifestly breaks scale invariance. Under a dilatation $\mathbf{r} \to \lambda \mathbf{r}$,

$$H \to H_\lambda = -\frac{1}{2m\lambda^2}\left(\frac{\partial^2}{\partial x^2}+\frac{\partial^2}{\partial y^2}+\frac{\partial^2}{\partial z^2}\right)+\frac{g}{\lambda^2}\delta(x-y)\delta(y-z)+\frac{\lambda^2}{2}m\omega^2\left(x^2+y^2+z^2\right), \tag{4.1}$$

so that $\lambda^2 H_\lambda \neq H$. The harmonic term scales inversely with λ in comparison to the rest of the Hamiltonian, and the simple argument for scale invariance in the untrapped case fails. Even so, Ref. [105] demonstrated that the trapped case retains SO(2,1) symmetry. Defining $L_1 = \frac{1}{2\omega}\left(H_0 - H_\omega\right)$, $L_2 = \frac{1}{4}\sum_i \left(\mathbf{p}_i \mathbf{r}_i + \mathbf{r}_i \mathbf{p}_i\right)$, and $L_3 = \frac{1}{2\omega}\left(H_0 + H_\omega\right)$ (where H_ω is the trap potential, H_0 is the remaining part of the Hamiltonian, and i runs over the three particles), we obtain the algebra of SO(2,1):[1]

$$[L_1, L_2] = -iL_3,\ [L_2, L_3] = iL_1,\ [L_3, L_1] = iL_2. \tag{4.2}$$

From these generators, raising and lowering operators can be constructed which generate the spectrum and excited states of the 2D many-body problem [105], much like in the case of the simple harmonic oscillator. As that solution is confined to 2D (where we only have correspondence in the three-body problem), we will proceed as in the untrapped case.

Section 4.1: Wave function solution

The Schrödinger equation for this system takes the form

$$\left[-\frac{\nabla_r^2}{2m}+\frac{g}{m}\delta(x-y)\delta(y-z)+\frac{1}{2}m\omega^2 r^2\right]\psi(\mathbf{r}) = E\psi(\mathbf{r}) \tag{4.3}$$

[1]The negative sign on the first commutator distinguishes this algebra from that of SO(3) and allows scale transformations.

where x, y, and z again indicate the different-flavor particles, $\mathbf{r} = (x, y, z)$, and

$$\nabla_r^2 = \frac{\partial^2}{\partial x^2} + \frac{\partial^2}{\partial y^2} + \frac{\partial^2}{\partial z^2}. \tag{4.4}$$

By performing an orthogonal transformation,[2] we may factor out the dynamics along the c.m. direction. Specifically, with $Q = \frac{1}{\sqrt{3}}(x + y + z)$, $q_1 = \frac{1}{\sqrt{2}}(y - x)$, $q_2 = \frac{1}{\sqrt{6}}(x + y - 2z)$, and $\psi(\mathbf{r}) = \Phi(Q)\phi(q_1, q_2)$, we obtain

$$\left[-\frac{1}{2m}\frac{\partial^2}{\partial Q^2} + \frac{1}{2}m\omega^2 Q^2\right]\Phi(Q) = E_{\text{c.m.}}\Phi(Q), \tag{4.5}$$

which is the familiar 1D quantum harmonic oscillator. For the remaining coordinates,

$$\left[-\frac{\nabla_q^2}{2m} + \frac{\tilde{g}}{m}\delta(q_1)\delta(q_2) + \frac{1}{2}m\omega^2(q_1^2 + q_2^2)\right]\phi(q_1, q_2) = E_r\phi(q_1, q_2), \tag{4.6}$$

where $\tilde{g} = \dfrac{g}{\sqrt{3}}$ is the effective coupling, E_r is the energy of relative motion, and

$$\nabla_q^2 = \frac{\partial^2}{\partial q_1^2} + \frac{\partial^2}{\partial q_2^2}, \tag{4.7}$$

which thus reduces the problem to that of a single particle in a 2D harmonic oscillator potential with a δ-potential at the origin. From this point, we assume azimuthal symmetry (zero angular momentum; the interaction only saturates in $l = 0$ states) and take the mass $m = 1$.

Carrying out an expansion in terms of Laguerre polynomials (see Appendix E), the oscillator-space wave function is found to be

$$\tilde{\phi}_n \propto \frac{1}{\epsilon_\omega - (2n + 1)}, \tag{4.8}$$

where $\epsilon_\omega = E_r/\omega$. The inverse transform yields the position-space wave function as

$$\phi(\rho) = \frac{1}{\sqrt{N}}e^{-\rho^2/2}\sum_{n=0}^{\Lambda_\omega}\frac{L_n(\rho^2)}{\epsilon_\omega - (2n + 1)}, \tag{4.9}$$

where Λ_ω is an oscillator-excitation cutoff and $\rho \equiv \sqrt{m\omega}q$. The normalization $N \to \frac{1}{4}\psi_1\left(\frac{1-\epsilon_\omega}{2}\right)$ in the $\Lambda_\omega \to \infty$ limit, where $\psi_1(z)$ is the trigamma function; the polygamma function of order n is defined as

$$\psi_n(z) = \frac{d^{n+1}}{dz^{n+1}}\ln\Gamma(z). \tag{4.10}$$

[2]This transformation is a normalized version of Jacobi coordinates which does not change the masses. Having equal masses on q_1 and q_2 also keeps their frequencies ω equal and is essential for maintaining azimuthal symmetry.

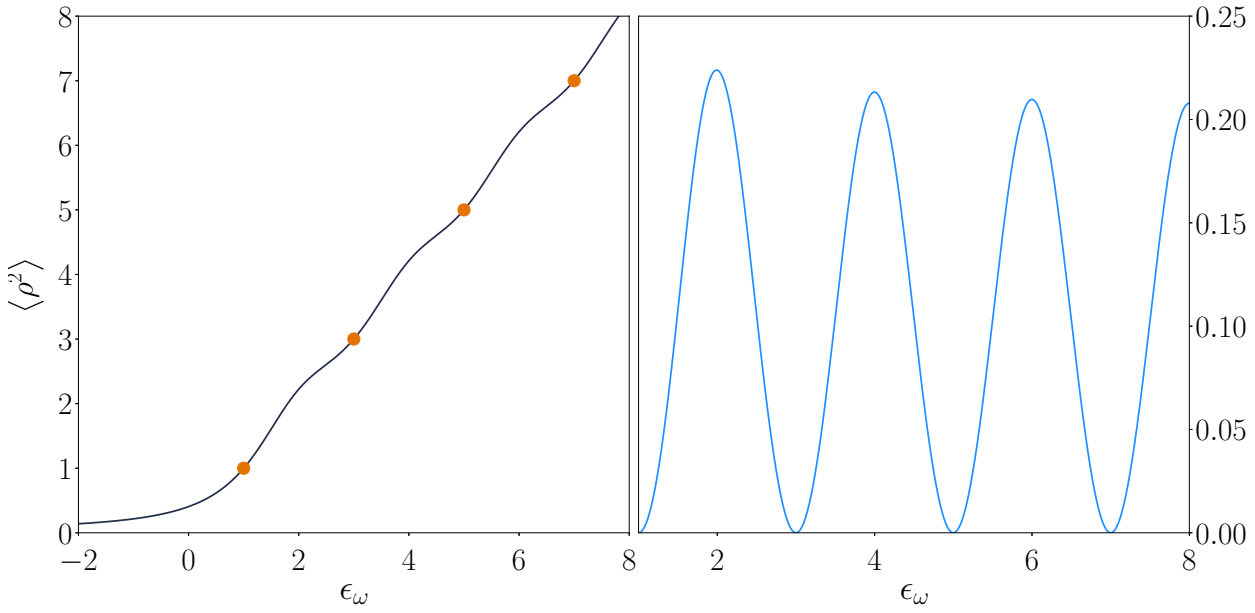

Figure 4.1: Hyperradius of the trapped three-body problem (left). The orange dots reflect the values in the noninteracting problem, indicating that the system slightly grows in size compared to a linear interpolation of the noninteracting states. This growth reaches a maximum halfway between the noninteracting energies and decreases at larger energies (right).

From Eq. (4.9), we can see that, just as in the untrapped problem, the wave function has a logarithmic singularity at the origin, in agreement with the Bethe-Peierls boundary condition discussed by Refs. [106, 107, 108]. As pointed out by Ref. [106], the summation in (4.9) can alternatively be recast in terms of the gamma function, Γ, and Kummer's confluent hypergeometric function of the second kind, U.

In the $\Lambda_\omega \to \infty$ limit, the trimer size converges to

$$\langle \rho^2 \rangle = \frac{\epsilon_\omega(\epsilon_\omega+1)^2\psi_1(-\frac{\epsilon_\omega+1}{2}) + 2(\epsilon_\omega^2+1)}{(\epsilon_\omega+1)^2\psi_1(\frac{1-\epsilon_\omega}{2})}. \tag{4.11}$$

Figure 4.1 displays this result, showing that the hyperradius roughly interpolates the values of the non-interacting problem. For very tightly bound systems (or weak trapping potentials; $-\epsilon_\omega \gg 1$), Eq. (4.11) approaches $-1/3\epsilon_\omega$.

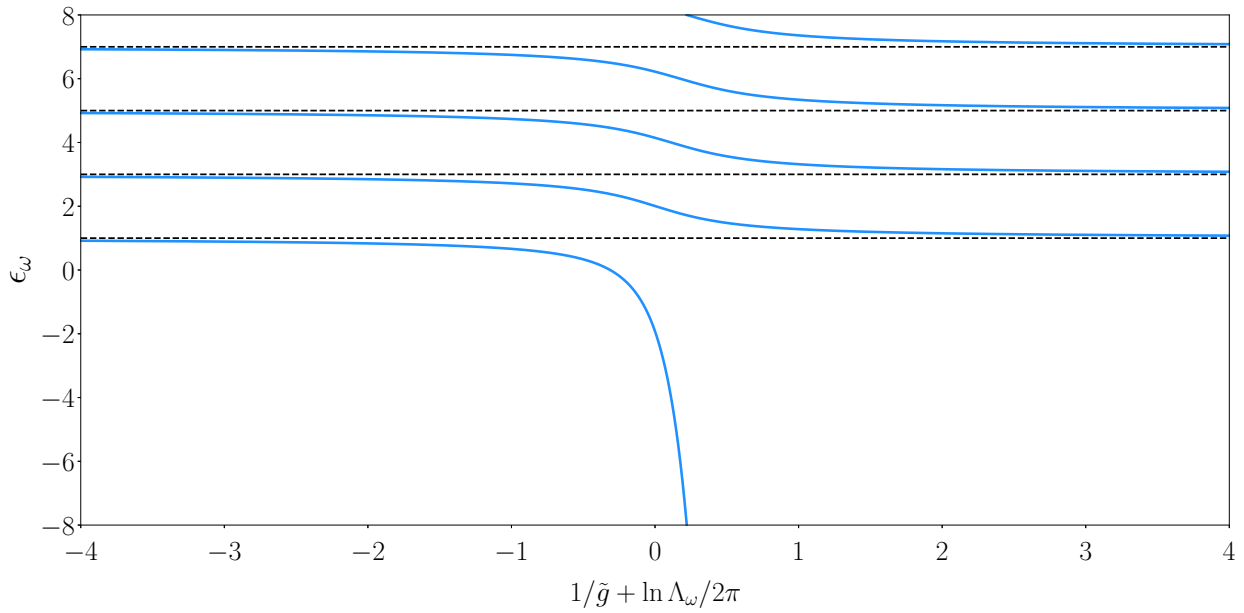

Figure 4.2: Relation of energy to renormalized coupling in the trapped three-body (relative) problem. Dashed lines indicate the noninteracting energies of the trapped problem.

Section 4.2: Renormalization

Just as in the untrapped problem, solving the wave function also furnishes the renormalization condition. In the harmonic trap, the coupling is renormalized according to

$$\frac{1}{\tilde{g}} = \frac{1}{\pi} \sum_{n=0}^{\Lambda_\omega} \frac{1}{\epsilon_\omega - (2n+1)} \to \frac{1}{2\pi} \left[\psi_0 \left(\frac{1-\epsilon_\omega}{2} \right) - \ln \Lambda_\omega \right], \tag{4.12}$$

where $\psi_0(z)$ is the digamma function. Unlike in the untrapped problem, with its unique bound state, the trapped problem admits excited states (all with positive energy); the coupling should be defined with respect to the ϵ_ω occuring in the lowest energy branch of Fig. 4.2.

A curious feature of the renormalized coupling is the appearance of $\ln \Lambda_\omega$. As Λ_ω ought to be the largest scale in the problem—indeed, as large as possible—all of the values of $\tilde{g}$ seen in Fig. 4.2 ought to be interpreted as negative. The discussion of Ref. [109] found that the 2D problem always yields a positive scattering length, consistent with our finding here that only attractive couplings are compatible with our solution.

The relative energy of the three-body system retains the discrete spectrum of the noninteracting problem, but the values are shifted down (Fig. 4.2). As pointed out by Ref. [109], in the limit of strong coupling, the entire excited-state spectrum will simply shift its energy labels by one unit, while the ground-state energy

will decrease without bound.

Section 4.3: Virial coefficient

As in the untrapped case, we have the relationship

$$\Delta b_3 = \frac{\mathcal{Q}_{1,1,1}^{\text{c.m.}}}{\mathcal{Q}_{1,1}^{\text{c.m.,2D}}} \frac{\mathcal{Q}_1^{\text{2D}}}{\mathcal{Q}_1} \Delta b_2^{\text{2D}}, \tag{4.13}$$

where all quantities here are understood to be in a trap. Both the $1+1+1$ c.m. and 1D single-particle cases have the Hamiltonian

$$H = \omega \left(n + \frac{1}{2} \right), \tag{4.14}$$

whereas both the $1+1$ c.m. and 2D single-particle cases have the Hamiltonian

$$H = \omega \left(n + m + 1 \right). \tag{4.15}$$

As a result, $\mathcal{Q}_1 = 3\mathcal{Q}_{1,0,0} = 3\mathcal{Q}_{1,1,1}^{\text{c.m.}}$ and $\mathcal{Q}_1^{\text{2D}} = 2\mathcal{Q}_{1,0}^{\text{2D}} = 2\mathcal{Q}_{1,1}^{\text{c.m.,2D}}$, so that [110]

$$\Delta b_3 = \frac{2}{3} \Delta b_2^{\text{2D}}. \tag{4.16}$$

From Ref. [106],

$$\Delta b_2^{\text{2D}} = \frac{1}{2} \sum_{n=0}^{\infty} \left[e^{-\beta\omega(2\nu_n+1)} - e^{-\beta\omega(2n+1)} \right], \tag{4.17}$$

where ν_n is the n^{th} solution of

$$\psi_0(-\nu) = \ln \left(\frac{1-\epsilon_\omega}{2} \right), \tag{4.18}$$

where ϵ_ω again refers to the ground-state energy branch. For weak interactions (in comparison to the trap frequency) [109],

$$2\nu_n + 1 \simeq 2n + 1 + \frac{2}{\ln\left[\left(1-\epsilon_\omega\right)/2 \right]}, \tag{4.19}$$

so that

$$\Delta b_3 \simeq \frac{-\beta\omega \sinh^{-1} \beta\omega}{3 \ln\left[\left(1-\epsilon_\omega\right)/2 \right]}. \tag{4.20}$$

Section 4.4: Few-body wave functions

Motivated by the success of the few-body iterative method in the untrapped problem, we now apply the same approach in the harmonic trap. However, because periodic boundary conditions are incompatible with the harmonic oscillator, and because oscillator states are not momentum eigenstates, we are unable to exploit the center-of-momentum frame. While the antisymmetric basis expansion still applies, allowing for a fermionic solution, we will not encounter the same dimensionality reduction that conservation of momentum in a fixed frame enabled outside of the trap. The solution found will thus be in terms of the full wave function, with no simpler, auxiliary functions.

As the previous chapter detailed the untrapped $2+1+1$ solution, we will only outline the trapped procedure, as most of the details are unchanged.[3] The starting point is the Hamiltonian (3.16), with the addition of the trapping potential for each particle. Instead of a Fourier (plane wave) expansion, we will expand in the trapped single-particle basis—Hermite polynomials with Gaussian weight factors, expressed generically as $\phi_n(x)$ for the n^{th} excited state.

Carrying out the antisymmetric expansion as before, the $2+1+1$ Schrödinger equation in the oscillator basis reads

$$\tilde{\psi}\left(n_1,n_2,m,l\right) = \frac{-g\omega/2}{E_0-E}\times \sum_{n',m',l'}\left[\tilde{\psi}\left(n',n_2,m',l'\right)-\tilde{\psi}\left(n_2,n',m',l'\right)\right]I_{n_1}+\left[\tilde{\psi}\left(n_1,n',m',l'\right)-\tilde{\psi}\left(n',n_1,m',l'\right)\right]I_{n_2}, \quad (4.21)$$

where $E_0/\omega = n_1+n_2+m+l+2$ is the noninteracting trap energy, and

$$I_n = \int_{-\infty}^{\infty} dx\ \phi_n(x)\phi_m(x)\phi_l(x)\phi_{n'}(x)\phi_{m'}(x)\phi_{l'}(x). \quad (4.22)$$

Expressed in terms of Hermite polynomials, Eq. (4.22) reads

$$I_n = \int_{-\infty}^{\infty} dx\ e^{-3x^2} H_n(x)H_m(x)H_l(x)H_{n'}(x)H_{m'}(x)H_{l'}(x), \quad (4.23)$$

and formal solutions are derived in Appendix F. The more compact of these solutions is given by

$$I_n = \frac{1}{\pi\sqrt{3\cdot 2^{n+m+l+n'+m'+l'}\,n!\ m!\ l!\ n'!\ m'!\ l'!}}\frac{\partial^n}{\partial t_1^n}\frac{\partial^m}{\partial t_2^m}\frac{\partial^l}{\partial t_3^l}\frac{\partial^{n'}}{\partial t_4^{n'}}\frac{\partial^{m'}}{\partial t_5^{m'}}\frac{\partial^{l'}}{\partial t_6^{l'}}\left[e^{T_1^2/3-T_2}\right]_{t_1,\ldots,t_6=0}, \quad (4.24)$$

[3] The repulsive two-body interacting analog of this problem is studied in Ref. [111].

where $T_1 = \sum_{i=1}^{6} t_i$ and $T_2 = \sum_{i=1}^{6} t_i^2$; the more explicit, albeit more lengthy, solution is given by

$$I_n = \frac{(-1)^{(n+m+l+n'+m'+l')/2}}{\pi 2^{n+m+n'+m'}} \sqrt{\frac{n!\ m!\ l!\ n'!\ m'!\ l'!}{3^{n+m+l+n'+m'+l'+1}}} \sum_{\substack{i+j+k=n \\ i'+j'+k'=n'}} \sum_{\substack{\alpha+\beta+\gamma=m \\ \alpha'+\beta'+\gamma'=m'}} \sum_{\substack{a+b=l \\ a'+b'=l'}} \delta_{k+\gamma+b,k'+\gamma'+b'} \times$$
$$\frac{(-1)^{\alpha+\alpha'+a+a'+k+\gamma+b}}{i!\ j!\ k!\ i'!\ j'!\ k'!\ \alpha!\ \beta!\ \gamma!\ \alpha'!\ \beta'!\ \gamma'!\ a!\ b!\ a'!\ b'!}\ 2^{k+k'+\gamma+\gamma'}\ 3^{(i+i'+\alpha+\alpha')} \times$$
$$(k+\gamma+b)!\ \frac{(i+\alpha)!\ (j+\beta+a)!\ (i'+\alpha')!\ (j'+\beta'+a')!}{\left(\frac{i+\alpha}{2}\right)!\ \left(\frac{j+\beta+a}{2}\right)!\ \left(\frac{i'+\alpha'}{2}\right)!\ \left(\frac{j'+\beta'+a'}{2}\right)!}, \quad (4.25)$$

where $i+\alpha$ and $j+\beta+a$ are even (as are their primed counterparts).

The complicating aspect of the harmonic trap stems from the nonseparability of the sums in Eq. (4.21). Although formal solutions of Eq. (4.23) have been found, they do not have a simple closed form. Instead of momentum, the parity of the initial and final interacting particles is conserved: $n+m+l-(n'+m'+l') \in \mathbb{Z}_2$. The number of non-vanishing matrix elements describing transitions from one state to another is thus far greater than in the untrapped case. Furthermore, the inability to fix the overall excitation number prevents any simplifying elimination of variables, so that each term in Eq. (4.21) depends on all four variables, unlike in the untrapped problem.

Unfortunately, without further simplification (if possible), Eqs. (4.24) and (4.25) are less efficient means of computing I_n than directly evaluating Eq. (4.23) numerically. Considering this difficulty alongside the enormity of the wave functions to be solved (Λ_ω^N entries, where N is the total particle number), we do not present numerical results here, leaving further analysis for future work.

Section 4.5: Summary

Solving the three-body trapped problem analytically, we found that only attractive couplings permit solutions, shifting the noninteracting spectrum lower and adding a bound state. The same correspondence with the 2D problem as in the untrapped problem enabled us to again find a direct relationship between the first non-trivial virial coefficients of the two systems. While the general virial coefficient requires numerical evaluation, we found a closed expression valid for weak couplings.

Unfortunately, the presence of the trapping potential prevented the efficient use of the iterative method that solved the untrapped problem. Moving past this setback, we now proceed with the many-body problem.

CHAPTER 5: THE FERMIONIC MANY-BODY PROBLEM AT FINITE TEMPERATURE

Although the simplifying tricks used in previous chapters can, in principle, be applied to any number of particles, they are most useful for small numbers. The combinatorial nature of the symmetrized Fourier transform causes the number of terms to grow factorially with particle number, quickly making the equations unwieldy. Even with the equations in hand, their numerical solution becomes exponentially more difficult as more particles are added—reducing the dimension by three matters little when the dimension is large to begin with. Furthermore, extending the analysis to finite temperature requires the inclusion of excited states—indeed, the entire spectrum—which is prohibitively difficult by the iterative method. The basis of our approach will be the *Hubbard* Hamiltonian, so we now turn our attention to examining some of its features.[1]

Section 5.1: The Hubbard model

Since the 1960s, the Hubbard model has been studied in condensed matter physics and related fields as a paradigm for understanding collections of fermionic spins. Despite its "oversimplified" character [113], the model captures many interesting phenomena, such as (anti)ferromagnetism and spin-charge separation [114, 81]. The Hubbard model is defined by the Hamiltonian

$$\hat{H} = -t \sum_{\sigma} \sum_{\langle ij \rangle} \hat{c}^{\dagger}_{i\sigma} \hat{c}_{j\sigma} + U \sum_{i} \hat{n}_{i\uparrow} \hat{n}_{i\downarrow} + \mu \sum_{i,\sigma} \hat{n}_{i\sigma}, \tag{5.1}$$

where t is the strength of the kinetic "hopping" term between neighboring sites i and j, provided by the creation and annihilation operators of spin σ, $\hat{c}^{\dagger}_{i\sigma}$ and $\hat{c}_{j\sigma}$, respectively; U is the interaction strength between spins of different flavors on the same site i, provided by the number operators $\hat{n}_{i\sigma} = \hat{c}^{\dagger}_{i\sigma} \hat{c}_{i\sigma}$; and μ is the chemical potential. While the general study of the Hubbard model is extensive (see [113, 115]), for the present purpose, we will focus our attention on the noninteracting case ($U = 0$) with a single spin species.

[1] We have prepared a manuscript [112] for the work in this chapter which is not yet published.

For a single flavor, setting $t = 1$ reduces (5.1) to

$$\hat{H} = \sum_i -\hat{c}_i^\dagger \hat{c}_{i+1} + \mu \hat{c}_i^\dagger \hat{c}_i, \tag{5.2}$$

or, written in a more suggestive form,

$$\hat{H} = \sum_i -\frac{1}{2}\left(\hat{c}_i^\dagger \hat{c}_{i-1} - 2\hat{c}_i^\dagger \hat{c}_i + \hat{c}_i^\dagger \hat{c}_{i+1}\right) + (\mu - 1)\,\hat{c}_i^\dagger \hat{c}_i. \tag{5.3}$$

Here, we recognize the finite-difference form of the second derivative,

$$\frac{d^2 f}{dx^2} = \lim_{h\to 0} \frac{f(x-h) - 2f(x) + f(x+h)}{h^2}, \tag{5.4}$$

where we instead have $h = 1$, corresponding to the lattice spacing. We thus see that the single-flavor Hubbard model is nothing more than a description of free fermions subject to a chemical potential[2] in discretized space. However, as we now show, the discreteness of space must be kept in mind when relating the hopping terms to the kinetic energy.

Ignoring the diagonal contribution from the chemical potential, Eq. (5.3) can be expressed in matrix form as

$$\hat{H} = -\frac{1}{2}\begin{pmatrix} -2 & 1 & 0 & \dots & 0 & 1 \\ 1 & -2 & 1 & 0 & \dots & 0 \\ 0 & 1 & -2 & 1 & \dots & 0 \\ \vdots & & & \ddots & & \vdots \\ 1 & 0 & \dots & 0 & 1 & -2 \end{pmatrix}, \tag{5.5}$$

where periodic boundary conditions have been assumed. The eigenvectors of (5.5) are analogous to those of free particles in continuous space:

$$v_k^j \propto \exp\left(i\frac{2\pi kj}{N_x}\right), \tag{5.6}$$

where v_k^j is the j^{th} component of the k^{th} eigenvector and N_x is the number of lattice sites. However, the eigenvalues of (5.5) are *not* the same as those in the continuum:

$$\epsilon_k = 1 - \cos\left(\frac{k\pi}{N_x}\right). \tag{5.7}$$

[2]The original definition of the Hamiltonian has the effect of shifting $\mu \to \mu - 1$, which will be evident in our discussion of the worm algorithm.

Although the leading-order term of (5.7) is indeed $p_k^2/2$, with $p_k = k\pi/N_x$, the subsequent terms of the cosine series lead to deviations from the continuum dispersion relation for increasing values of k. As a result, the Hubbard model is most accurate when describing low-energy excitations.[3] To capture the full spectrum, it would be necessary for the momentum to take into account *all* lattice sites—space and momentum are Fourier conjugates—rather than only the two nearest neighbors.

Before moving on, we note that the preceding equations are slightly modified when the spatial boundary conditions are open rather than periodic.[4] The lower-left and upper-right entries of (5.5) vanish; the eigenvectors of (5.6) are restricted to sine functions; and in both (5.6) and (5.7), N_x is replaced with $N_x + 1$.

Section 5.2: The Grassmann field approach

In the mid-1800s, Hermann Grassmann developed a new type of algebra which neatly encompassed linear algebra, geometry, and even quaternion and Clifford algebras. However, many years passed before other mathematicians took note of his work [116]; still more years passed before physicists recognized that the structure of Grassmann algebras could be used to represent fermionic antisymmetry.

The key feature of Grassmann numbers that makes them useful for describing fermions is their anticommutative property: two Grassmann numbers θ_1 and θ_2 satisfy $\theta_1\theta_2 = -\theta_2\theta_1$. From this property, the square of any Grassmann number vanishes: $\theta^2 = 0$, as the product may be written in either order. Already, we see connections to fermions, as fermionic creation and annihilation operators share the above properties. Since all higher powers must also vanish, functions of Grassmann variables are, at most, linear; any such function can be expressed as

$$f(\theta) = a + b\theta. \tag{5.8}$$

Of course, functions of several Grassmann variables may be multilinear.

Unfortunately, the established convention appropriates the notation of integration and differentiation to represent one operation on Grassmann variables that has nothing to do with calculus. Many authors use this convention to claim that "For Grassmann numbers, integration and differentiation are the same thing." In truth, there is no sense in which Grassmann numbers have any notion of continuity—one cannot take the limit of a Grassmann number, and the numbers themselves lack the concept of magnitude. The operation that is *represented by* the integral symbol does at least have the same *effect* as a derivative applied to a

[3] For systems in an optical lattice with nearest-neighbor hopping, the Hubbard dispersion relation is exact.

[4] "Open" boundary conditions on N_x lattice sites are equivalent to hard-wall boundary conditions on $N_x + 2$ lattice sites, where the wave function vanishes on the two endpoints. The length of the interval is thus $N_x + 1$.

linear function:

$$\int (a + b\theta)\ d\theta = b. \tag{5.9}$$

As Eq. (5.9) is not truly an integration, there are never bounds on the integral symbol. Importantly, the integration variable (which is *not* a differential) is also a Grassmann number: $\theta\ d\theta = -d\theta\ \theta$. When multiple variables are present in the integral, this fact must also be kept in mind. For a double integral, $d\theta_1 d\theta_2 = -d\theta_2 d\theta_1$, resembling the behavior of differential forms. Another aspect of Grassmann integration worth noting is that the Jacobian behaves oppositely from the way it does in actual integrals. With the change of variables $\chi = c\theta$, for Eq. (5.9) to be true in both variables, it must be the case that $d\theta = c\ d\chi$:

$$\int \theta\ d\theta = \frac{1}{c}\int \chi\ d\theta = \int \chi\ d\chi \implies d\theta = c\ d\chi. \tag{5.10}$$

Taking another step towards applying the Grassmann formalism to fermions, let us now examine the Grassmann integral of an exponential containing several variables. Let $\chi = (\chi_1, \chi_2, \ldots, \chi_n)$ and $\chi^\dagger = (\bar{\chi}_1, \bar{\chi}_2, \ldots, \bar{\chi}_n)^T$ denote vectors of n Grassmann variables,[5] and let M be an $n \times n$ matrix. Then,

$$\int e^{-\chi^\dagger M \chi}\ d\bar{\chi}_1 d\chi_1 d\bar{\chi}_2 d\chi_2 \ldots d\bar{\chi}_n d\chi_n = \det M. \tag{5.11}$$

Compare this to the analogous expression for a complex vector $\mathbf{z}$ and Hermitian matrix A, where

$$\int e^{-\mathbf{z}^\dagger A \mathbf{z}}\ dz_1 dz_1^* dz_2 dz_2^* \ldots dz_n dz_n^* = \frac{(2\pi i)^n}{\det A}, \tag{5.12}$$

where we again see the inverted behavior of the Jacobian for Grassmann variables. While the 2D case of Eq. (5.11) can be easily verified, the general case may be understood as follows. When the exponential is expanded as a Taylor series, any terms with more than one power of a single variable will vanish due to the fact that $\chi^2 = 0$, and any terms without one of the variables will vanish due to the fact that $\int d\chi = 0$. The only nonvanishing terms thus arise from the n^{th} term of the Taylor series, where each Grassmann variable appears once. There are $n!$ such terms (in accordance with the multinomial theorem, after permuting variables to reach the same form), the weight of which is cancelled by the $1/n!$ of the Taylor series. The coefficients (and their signs) on each of these terms cover all entries of M exactly once, so that the determinant appears in the Leibniz form,

$$\det M = \epsilon_{i_1 i_2 \ldots i_n} M_{1 i_1} M_{2 i_2} \ldots M_{n i_n}, \tag{5.13}$$

[5] $\bar{\chi}_1$ is not the complex conjugate of χ_1—Grassmann numbers are not elements of $\mathbb{C}$, the field of complex numbers.

where summation is implied on repeated indices. As we will see in the following formulation, the appearance of each entry of M once—and only once—corresponds to *one* fermionic creation operator and *one* fermionic annihilation operator on each spacetime lattice site. For a more linear-algebra-based derivation, as well as a deeper discussion of the Grassmann formalism, see Ref. [114]; for an in-depth analysis of multivariable Gaussian integrals, including general quadratic forms, see Ref. [117].

Adapting the approach of Ref. [118] (which treated four-component fermions), we formulate the lattice theory for the thermodynamics of the nonrelativistic, three-component Fermi gas in 1D as a Grassmann field theory in $1+1$ Euclidean spacetime. From the continuum Euclidean Lagrangian

$$\mathcal{L}_E = \psi^\dagger \left(\frac{\partial}{\partial \tau} - \frac{\nabla^2}{2m} - \mu \right) \psi - g \left(\psi^\dagger \psi \right)^3 , \tag{5.14}$$

where $\psi = (\psi_1, \psi_2, \psi_3)$, τ is the imaginary time (inverse temperature), and μ is the chemical potential, the derivatives are discretized to yield the lattice action,

$$S = \sum_{\mathbf{n}} \left[\psi_{\mathbf{n}}^\dagger \left(1 + \frac{1}{m} \right) \psi_{\mathbf{n}} - \psi_{\mathbf{n}}^\dagger e^\mu \psi_{\mathbf{n}-\mathbf{e}_0} - \psi_{\mathbf{n}}^\dagger \frac{1}{2m} \left(\psi_{\mathbf{n}+\mathbf{e}_1} + \psi_{\mathbf{n}-\mathbf{e}_1} \right) - g \left(\psi_{\mathbf{n}}^\dagger e^\mu \psi_{\mathbf{n}-\mathbf{e}_0} \right)^3 \right] , \tag{5.15}$$

where the sum is over all spacetime lattice sites $\mathbf{n}$. Both the temporal and spatial lattice spacings have been set to unity, and $\mathbf{e}_0$, $\mathbf{e}_1$ are unit vectors in the temporal and spatial directions, respectively.[6]

Upon expanding the exponential in the partition function,

$$\mathcal{Z} = \int \mathcal{D}\psi^\dagger \mathcal{D}\psi \; e^{-S}, \tag{5.16}$$

we obtain a sum over products of the individual terms in Eq. (5.15). Carrying out the integrals, only the terms in the sum that contain exactly one creation and one destruction operator of each flavor, at each site $\mathbf{n}$, will survive. Each of these terms will carry different weights, determined by the prefactors inherited from (5.15), and corresponding to what is occurring at each lattice site. For example, the weight associated with a step in the time-like direction is different from one for a step in the space-like direction. One single term in this sum represents one possible configuration of the lattice consistent with the Lagrangian (5.14); the paths traced out by the fermionic operators represent worldlines in Euclidean spacetime. Not all operators lead to paths, however, as many result in on-site number operators or vacuum fermion loops.

Of the operators that *do* trace out worldlines, visually representing the terms as paths through the lattice sheds much light on the behavior of the partition sum and reveals what kinds of configurations are possible.

[6]The perhaps unexpected appearance of e^μ on certain terms arises from a treatment of the chemical potential as the time-like component of an Abelian gauge field. First appearing in lattice QCD, this approach avoids quadratic divergences. See [119, 120].

In particular, any site with an incoming world line must also have an outgoing world line. As a result, all world lines must form closed loops in the temporal direction, leading to time-like periodic boundary conditions.[7] Additionally, vacuum loops must occur entirely within one time-step, as the nonrelativistic time derivative moves only in the forward direction.

The number of worldlines that traverse the time direction corresponds to the number of fermions on the lattice. With periodic boundary conditions, one path may loop around the temporal direction several times before closing on itself, corresponding to fermionic exchanges of as many particles are there are loops in the path. By choosing open spatial boundaries,[8] though, such exchanges are eliminated, and the sign problem is thus partially avoided. As detailed in Ref. [118], the sign problem may actually be avoided *entirely* in this scheme by recursively summing over the sites without worldlines. Such sums account for all possible loops that could exist in the loop-free, base-class configurations, such as the one shown in Fig. 5.1.

The Grassmann formulation has provided a useful graphical representation which demonstrates how worldlines must behave. Namely, fermion worldlines must close on themselves in the temporal direction; like-flavor worldlines do not intersect; and worldlines cannot move backwards in imaginary time. Further, with open spatial boundary conditions, there is no sign problem. While this formalism has certainly provided useful insights, as the authors of Ref. [121] helpfully pointed out, the fermion loops may be neglected altogether in low-energy, nonrelativistic studies. With this simplification, we proceed with their approach.

Section 5.3: The worm algorithm

While the set of worldline configurations is the same as that reached by the Grassmann integral (modulo vacuum loops), different routes exist that lead to the same worldline representation. Indeed, the worldline picture is a natural way of representing statistical field theoretical problems in position space, with several different algorithms available for performing the statistical sampling [122, 123]. Here, we follow the approach of [121], modifying as necessary to suit our 1D three-body model.

Separating the parts of the Hamiltonian that are diagonal in position space (H_d) from the hopping term (H_h), the full Hamiltonian is written $H_\mu = H_d - H_h$, where the subscript μ indicates that the chemical

[7] This is an inherent feature; the boundary conditions are not arbitrary. If temporal boundary conditions were instead open, the absences of a creation operator at one end and a destruction operator at the other would cause those terms to vanish in the Grassmann integrals.

[8] The bidirectionality of the spatial derivative makes this choice possible, in contrast to the temporal derivative.

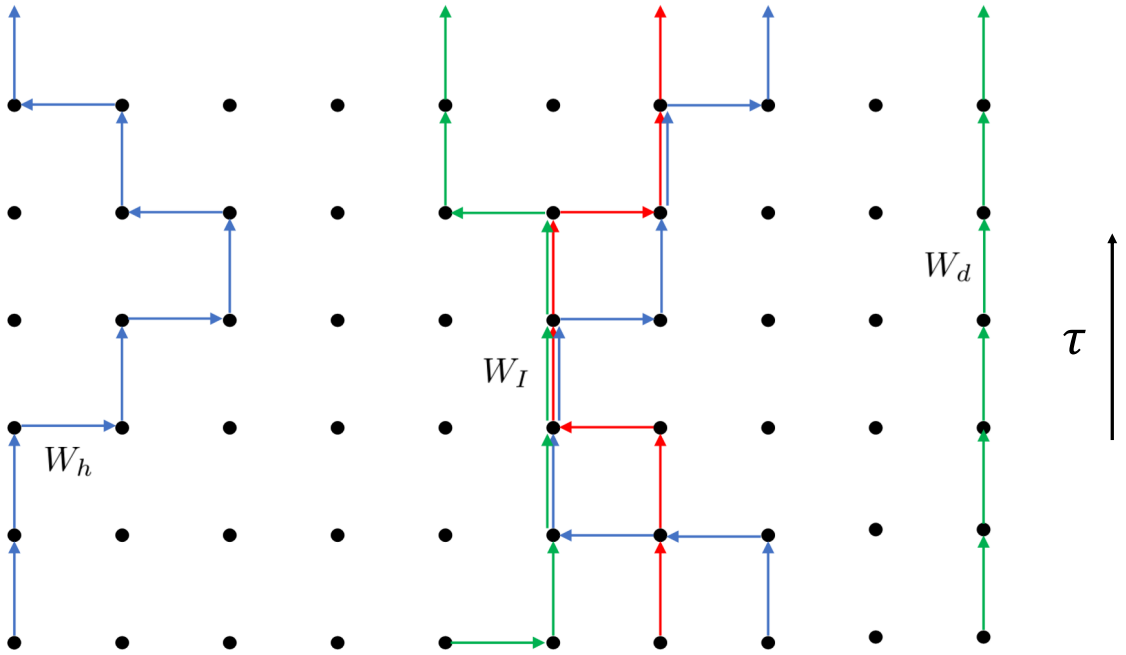

Figure 5.1: Example worldline configuration for two particles of two flavors (blue and green) and one particle of the third flavor (red), with symbols denoting weights of local configurations. Note that all worldlines close on themselves in the time-like direction.

potential has been absorbed into the Hamiltonian. The two contributions are

$$H_d = \sum_{i,\sigma} (2t_\sigma - \mu_\sigma) N_{\sigma,i} + g N_{a,i} N_{b,i} N_{c,i}, \tag{5.17}$$

$$H_h = \sum_{i,\sigma} t_\sigma \left(c^\dagger_{i,\sigma} c_{i+1,\sigma} + c^\dagger_{i+1,\sigma} c_{i,\sigma} \right), \tag{5.18}$$

where i denotes the spatial lattice site, N is the number operator, $t_\sigma = 1/(2m_\sigma \ell^2)$, and σ runs over the fermion species a, b, and c. Since we only consider balanced systems here, $t_\sigma = t$, $m_\sigma = m$, and $\mu_\sigma = \mu$; we fix $m = \ell = 1$, which also determines $t = 1/2$. The partition function can be expanded in continuous time as [121]

$$\mathcal{Z} = \sum_{k=0}^{\infty} \int_0^\beta d\tau_k \int_0^{\tau_k} d\tau_{k-1} \ldots \int_0^{\tau_2} d\tau_1 \ \mathrm{Tr} \left[e^{-(\beta-\tau_k)H_d} H_h e^{-(\tau_k - \tau_{k-1})H_d} H_h \ldots H_h e^{-\tau_1 H_d} \right]. \tag{5.19}$$

A rather formal derivation of this expansion can be found in Ref. [124]; we present a more intuitive, operator-based approach in Appendix G.

Discretizing imaginary time so that $d\tau_k = \Delta\tau$ and $\tau_k = n\Delta\tau$ (n integer), the partition function (5.19)

becomes a weighted sum over spacetime lattice configurations like the one shown in Fig. 5.1. The weight of each configuration may be broken down into a product over the local weights for all flavors at each lattice site, which correspond directly to the factors appearing in (5.19):

$$W_d = \quad e^{\tau(\mu-1)}, \tag{5.20}$$

$$W_h = \quad \tau/2, \tag{5.21}$$

$$W_I = \quad e^{-\tau g}, \tag{5.22}$$

where we have dropped the Δ in $\Delta\tau$ (as we do from hereon). The weights W_d, W_h, and W_I are depicted once each in Fig. 5.1 at instances where they appear; note that W_I only occurs when worldlines of each of the three flavors share a time-like link (the three factors of W_d *also* contribute to the weight where W_I applies). The index k may be interpreted as the number of spatial hops (factors of W_h) occurring in a given worldline, with time-like steps in between hops (factors of W_d or W_I); evidently, k must be an even number for periodic worldlines.

With the weights of lattice configurations $\Omega(c)$ computable in terms of local weights as

$$\Omega(c) = (W_d)^{N_\tau N} (W_h)^{n_h} (W_I)^{n_I}, \tag{5.23}$$

where $N_\tau = \beta/\tau$, N is the total particle number among all flavors, n_h is the number of spatial hops across all flavors, and n_I is the number of interacting time-like links, the problem now is how to efficiently sample from the distribution of configurations provided by the discrete form of (5.19). In particular, this distribution is the lattice partition function, now expressible as

$$\mathcal{Z} = \sum_c \Omega(c). \tag{5.24}$$

The *worm algorithm* solves this problem by creating, destroying, and/or modifying worldlines by a series of local updates. The "worm" is this series of updates, which traverses the lattice and effects updates along its path. As described in detail in Ref. [121], the procedure is as follows.

First, one of the three fermion species is selected at random as the subject of the update. Second, a lattice site is randomly chosen, which admits two possibilities: The lattice site is or is not occupied by an existing worldline of the chosen species. If the site is unoccupied, the "tail" of the worm is established at the lattice site, which serves as the beginning of a new worldline. This first end of the new worldline is anchored to the initial site. The "head" of the worm then makes a spatial or temporal step, and according

to probabilities that will be discussed soon, this movement of the head is accepted or rejected. If the move is accepted, the worldline grows from the tail to the site that the head has moved to. If the move is rejected, the newly created worldline is destroyed, and the update is complete. If the site is instead occupied by an existing worldline, it is designated as the tail, and the worldline is severed. The site occupied by the worldline immediately prior (in imaginary time) to the tail becomes the head of the worm, which may then move according to local updates. The movements of the head continue until reaching the tail and concluding the update. Once the head meets the tail, either an incomplete worldline has been destroyed, or it has been closed and completed.

The movement of the head of the worm constitutes the bulk of the algorithm. The simplest case arises when the head lands on a site that is occupied by a *different* worldline than it belongs to. In this case, the intersected worldline is severed, and the head moves to the site of the intersected worldline immediately prior to the intersection. The worldline that had been growing fuses to the remainder of the intersected worldline, so that the segments of the two worldlines preceding the intersection trade roles. The tail is unaffected; the head resumes its movements, now updating the severed portion of the intersected worldline. In fact, aside from the fusion of the two worldlines, this case is identical to that of an initial step landing on an existing worldline, as described in the previous paragraph.

In all other cases, the site on which the head lands is considered for an update. Given the initial state of the site, there exists a set of possible states into which the site may evolve. Which final states are possible depends on the initial state as well as the direction in which the worm entered the site.[9] If there were only one possible final state (distinct from the initial state), then the update would simply follow the Metropolis algorithm [125]. The probability of transitioning to this final state would be

$$P_{i\to f} = \min\left\{1, \frac{W_f}{W_i}\right\}, \tag{5.25}$$

where W_i and W_f are the weights of the initial and final states, respectively. With probability $1 - P_{i\to f}$, the site would remain unchanged. However, none of the updates in this system present a binary choice between states. As a result, the weights of all possible outcomes must be considered when computing transition probabilities that obey detailed balance. We now provide a discussion of the probabilities which are tabulated in detail in Ref. [121].

The first non-binary case involves three possible outcomes (one of them being the initial state—no

[9] If the site is on a spatial boundary, the number of possible final states is reduced.

change). With W_0 (initial), W_1, and W_2 being the weights of these three states, there are four possibilities:

$$W_0 > W_1 + W_2, \tag{5.26}$$

$$W_1 > W_0 + W_2, \tag{5.27}$$

$$W_2 > W_0 + W_1, \tag{5.28}$$

$$W_a \leq W_b + W_c, \tag{5.29}$$

where W_a, W_b, and W_c apply to all permutations of W_0, W_1, and W_2. In cases (5.27) and (5.28), the weight of one final state is greater than the sum of all other weights; that state is automatically chosen as the new state. In case (5.26), the initial state has a greater weight than the sum of the others. With probability $P_{0\to1} = W_1/W_0$, the state is updated to that of W_1, and similarly for W_2; failing either of these options, the state remains unchanged. In case (5.29), no state's weight dominates the others', but a new state is guaranteed—the update is rejection-free. In such a case,

$$P_{0\to1} = \frac{W_0 + W_1 - W_2}{2W_0}, \tag{5.30}$$

where the pattern may be described generally as

$$P_{i\to f} = \frac{W_i + W_f - W_{\text{excl}}}{2W_i}, \tag{5.31}$$

where i and f are the initial and final states, respectively, and W_{excl} denotes the weight of the state excluded from the transition. Given that $P_{0\to2}$ also follows this pattern, $P_{0\to1}+P_{0\to2} = 1$, demonstrating the certainty of a transition. The quaternary case follows the same reasoning, and we do not include it here. However, a simplification pointed out by [121] is that case (5.28) never arises, since $W_h \ll W_d$ for $\tau \ll 1$. We provide the complete set of possible local transitions in Table 5.1, where the configuration labels follow the scheme of Fig. 5.2.

Section 5.4: Relation of numerical results to physical quantities

As in previous chapters, a few comments are in order regarding the relation of numbers used and obtained in our application of Monte Carlo methods to physical quantities measurable in the lab. In particular, observables are reported in terms of their noninteracting values at fixed fugacity. These noninteracting

Table 5.1: Map of all possible local lattice updates in the worm algorithm, where integer labels correspond to those in Fig. 5.2. The outgoing directions are each respective to the possible final states.

Initial state	**Incoming worm direction**	**Possible final states**	**Outgoing worm direction**
0	Up	0, 1, 2, 3	Down, up, left, right
	Left	0, 5, 7	Right, up, left
	Right	0, 4, 6	Left, up, right
1	Down	0, 1, 2, 3	Down, up, left, right
	Left	5	Down
	Right	4	Down
2	Right	0, 1, 2, 3	Down, up, left, right
	Left	7	Down
3	Left	0, 1, 2, 3	Down, up, left, right
	Right	6	Down
4	Down	0, 4, 6	Left, up, right
	Up	1	Left
	Left	5	Left
5	Down	0, 5, 7	Right, up, left
	Up	1	Right
	Right	4	Right
6	Left	0, 4, 6	Left, up, right
	Up	3	Left
7	Right	0, 5, 7	Right, up, left
	Up	2	Right
8	Up	1	Update complete
	Right	4	
	Left	5	
	Down	0	
9	Up	2	Update complete
	Left	7	
	Right	0	
10	Up	3	Update complete
	Right	6	
	Left	0	

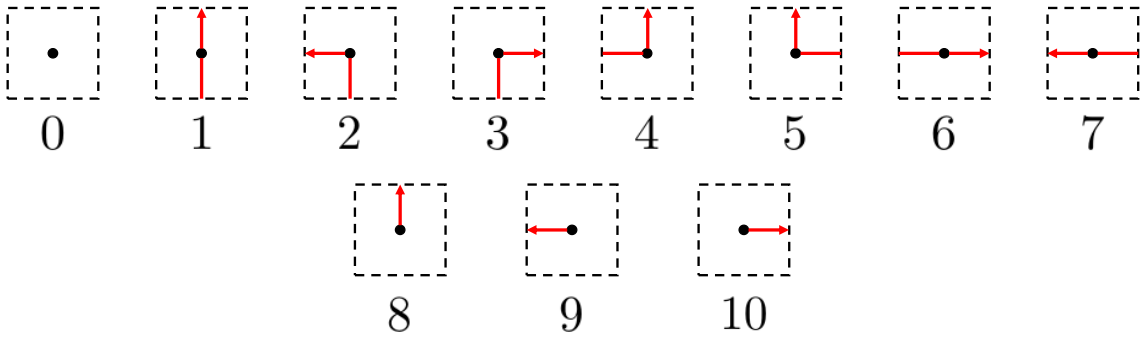

Figure 5.2: Possible configurations of individual lattice sites in the worldline representation. The bottom row depicts "tail" configurations, which only exist intermediately within an update.

quantities are easily computed from the partition function and here take the form

$$n_0 = \frac{3}{N_x + 1} \sum_{k=1}^{N_x} w_{\mathrm{FD}} \left(\beta \left[\epsilon_k - \mu\right]\right) \tag{5.32}$$

for the particle density and

$$E_0 = 3 \sum_{k=1}^{N_x} \epsilon_k \; w_{\mathrm{FD}} \left(\beta \left[\epsilon_k - \mu\right]\right) \tag{5.33}$$

for the energy, where ϵ_k is given by Eq. (5.7) (modified for open boundary conditions) and the Fermi-Dirac weight $w_{\mathrm{FD}}(x) = (1 + e^x)^{-1}$. In the worm algorithm, observables are calculated as

$$\langle \hat{\mathcal{O}} \rangle = \frac{1}{\mathcal{Z}} \sum_c \mathcal{O}(c) \; \Omega(c), \tag{5.34}$$

where $\mathcal{O}(c)$ is the observable's value in configuration c. The number of particles in a configuration is the number of worldlines in that configuration, while the energy of a configuration, found by taking the inverse temperature derivative of (5.23) and removing the chemical potential term from H_μ, is [121]

$$E(c) = N - \frac{n_h}{\beta} + g \frac{n_I}{N_\tau}. \tag{5.35}$$

Since the worm algorithm generates samples that are distributed according to the partition function, Eq. (5.34) simply becomes the arithmetic mean of the observable's value over the generated configurations.

Using thermodynamic relations and fluctuations in the grand canonical ensemble, the worldline formulation also provides access to linear response functions. In particular, the isothermal compressibility κ_T, which

measures the change in density (or volume) with respect to an applied pressure, is given by [75]

$$\kappa_T \equiv \beta L \left(\frac{\langle N^2 \rangle - \langle N \rangle^2}{\langle N \rangle^2} \right), \tag{5.36}$$

which may be computed by counting worldlines and performing the appropriate averages.

As described in Ref. [66], Tan's contact provides a measure of the quantum anomaly in the three-body interaction by quantifying the degree to which scale invariance is broken. In scale-invariant (nonrelativistic) 1D systems,

$$P - 2\frac{E}{L} = 0. \tag{5.37}$$

With scale invariance broken by the interaction, however, Eq. (5.37) is modified to

$$P - 2\frac{E}{L} = \mathcal{C}, \tag{5.38}$$

where $\mathcal{C}$ is the generalization of Tan's contact [126] (density) to three-body forces. The contact density may be computed directly from Eq. (5.38) but is also given by [66]

$$\mathcal{C} = -\frac{2}{gL} \langle V \rangle, \tag{5.39}$$

where V is the potential energy describing the interaction; we will employ both measures in this work.

Additionally, while we only consider balanced systems in this work (equal chemical potentials for all three fermion species), we may still access the isothermal magnetic susceptibility for a vanishing applied field. For a two-component gas, the difference in the number of spin-up and spin-down particles, $M = N_\uparrow - N_\downarrow$, quantifies the net polarization. The applied field h controls M, where the magnetic susceptibility χ describes the linear response. With three components, however, there are two independent polarizations, each with corresponding fields. Using scaled Jacobi coordinates, the three particle number operators may be recast as

$$\begin{pmatrix} M_1 \\ M_2 \\ M_3 \end{pmatrix} = \begin{pmatrix} 1 & 1 & 1 \\ a & -a & 0 \\ b & b & -2b \end{pmatrix} \begin{pmatrix} N_1 \\ N_2 \\ N_3 \end{pmatrix}, \tag{5.40}$$

where a and b are as yet undetermined. Similarly, replacing the three chemical potentials as

$$\begin{pmatrix} h_1 \\ h_2 \\ h_3 \end{pmatrix} = \begin{pmatrix} 1/3 & 1/2a & 1/6b \\ 1/3 & -1/2a & 1/6b \\ 1/3 & 0 & -1/3b \end{pmatrix} \begin{pmatrix} \mu_1 \\ \mu_2 \\ \mu_3 \end{pmatrix}, \tag{5.41}$$

the $\mu_1 N_1 + \mu_2 N_2 + \mu_3 N_3$ term in H_μ is transformed to $\mathbf{h} \cdot \mathbf{M}$, where $\mathbf{h} = (h_1, h_2, h_3)$, and $\mathbf{M} = (M_1, M_2, M_3)$. With the isothermal magnetic susceptibilities defined as [75]

$$\chi_i \equiv \frac{1}{\beta} \frac{\partial^2 \ln \mathcal{Z}}{\partial h_i^2} = \beta \left[\left\langle M_i^2 \right\rangle - \langle M_i \rangle^2 \right], \tag{5.42}$$

we find that[10] for balanced systems where $h_2 = h_3 = 0$ ($\mu_1 = \mu_2 = \mu_3 = \mu$), the two susceptibilities are equivalent:

$$\frac{\chi_2}{\chi_2^0} = \frac{\chi_3}{\chi_3^0} = \frac{\left\langle N_i^2 \right\rangle - \langle N_i N_j \rangle}{\left\langle N_k^2 \right\rangle_0 - \langle N_k N_l \rangle_0}, \tag{5.43}$$

where χ_i^0, $\langle \cdot \rangle_0$ indicate noninteracting quantities, and $i \neq j$, $k \neq l$ indicate any combination of fermion components. When written in terms of the noninteracting susceptibilities, the undetermined factors a and b cancel and are therefore arbitrary. For the noninteracting contribution in the denominator of Eq. (5.43), we obtain

$$\left\langle N_k^2 \right\rangle_0 - \langle N_k N_l \rangle_0 = \frac{1}{4} \sum_\epsilon \cosh^{-2} \left[\frac{\beta}{2} (\epsilon - \mu) \right], \tag{5.44}$$

where ϵ is given by the dispersion relation (5.7).

As before, the coupling g must be renormalized. However, the open spatial boundary conditions mean that (2.9) is no longer applicable, as that relation assumed periodic boundary conditions. Instead, we solve the three-body problem with hard-wall boundary conditions on an interval of length $L = N_x + 1$, expanding in a sine-wave basis. The result of this expansion,

$$\phi_{nml} = -\frac{8g/L^3}{\epsilon_{nml} + \tilde{\epsilon}_B} \sum_{i,j,k=1}^{N_x} \phi_{ijk} \; S_{nml}^{ijk}, \tag{5.45}$$

is solved iteratively for ϕ_{nml} at a given $\tilde{\epsilon}_B$, yielding the corresponding coupling g. In (5.45),

$$S_{nml}^{ijk} = \sum_{x=1}^{N_x} \sin\left(\frac{n\pi x}{L}\right) \sin\left(\frac{m\pi x}{L}\right) \sin\left(\frac{l\pi x}{L}\right) \sin\left(\frac{i\pi x}{L}\right) \sin\left(\frac{j\pi x}{L}\right) \sin\left(\frac{k\pi x}{L}\right), \tag{5.46}$$

[10] See Appendix H for details, including a derivation of Eq. (5.44).

the (effective) binding energy is $\tilde{\epsilon}_B = -(E - 3\epsilon_1)$, and the kinetic energy is $\epsilon_{nml} = \epsilon_n + \epsilon_m + \epsilon_l - 3\epsilon_1$, where ϵ_n, etc., are given by (5.7) (again, modified for open boundary conditions). The minimum hard-wall kinetic energy is subtracted in the effective binding energy so that $\tilde{\epsilon}_B$ is strictly non-negative for attractive couplings; in the limit $L \to \infty$, ϵ_1 vanishes, and $\tilde{\epsilon}_B \to -E$.

Finally, we turn to questions of convergence and dimensionless scales. The dimensionful parameters that can be tuned to control the system are the chemical potential μ, the inverse temperature β, the effective three-body binding energy $\tilde{\epsilon}_B$, the lattice spacing ℓ, and the system size L. An additional dimensionful parameter is the thermal wavelength, $\lambda_T = \sqrt{2\pi\beta}$, which is already fixed by the choice of β. As the thermal wavelength governs the "size" or extent of particles, to approach the continuum limit, particles must extend over many lattice sites. On the other hand, to approach the thermodynamic limit, the extent of the particles must be much smaller than the system size. We may capture both of these requirements with

$$\ell \ll \lambda_T \ll L, \tag{5.47}$$

where, as previously mentioned, we fix $\ell = 1$. The most useful dimensionless combinations of these parameters—which may be compared to experimental values—are $\beta\mu$, $\beta\tilde{\epsilon}_B$, and λ_T/L. For fixed λ_T/L, a given value of $\beta\tilde{\epsilon}_B$ represents equivalent interaction strengths among systems with different values of β, L, and g; the value of $\beta\mu$ controls the overall number of particles in the system. The results in this work are given for $\beta = 18$, $L = 81$, and $\tau = 0.005$.

Section 5.5: Equations of state, response functions, and other results

As seen in Fig. 5.3, the attractive interaction tends to increase the density at all values of $\beta\mu$, but especially around $\beta\mu = 0$. The largest effect occurs early on—at low density—as the interaction rapidly draws in more particles. Once the density grows and the noninteracting system begins to accumulate particles, though, the interaction effect is less pronounced. As expected, the virial expansion provides a good approximation for all couplings at low fugacity but diverges rapidly for $\beta\mu \gtrsim -2$.

The energy of the many-body system, shown in Fig. 5.4, initially closely matches the noninteracting result (at low fugacities): At low densities, the interaction does not fully take effect, as particles are less likely to encounter one another. In this regime, the virial expansion is again quite reliable. As particles accumulate, though, the interaction begins to dominate the energy, and the curves dip below the noninteracting energy. For the strongest couplings, the total energy even becomes negative.

After passing a minimum around $\beta\mu = 0$, the energy ratio begins to increase. One reason for this is

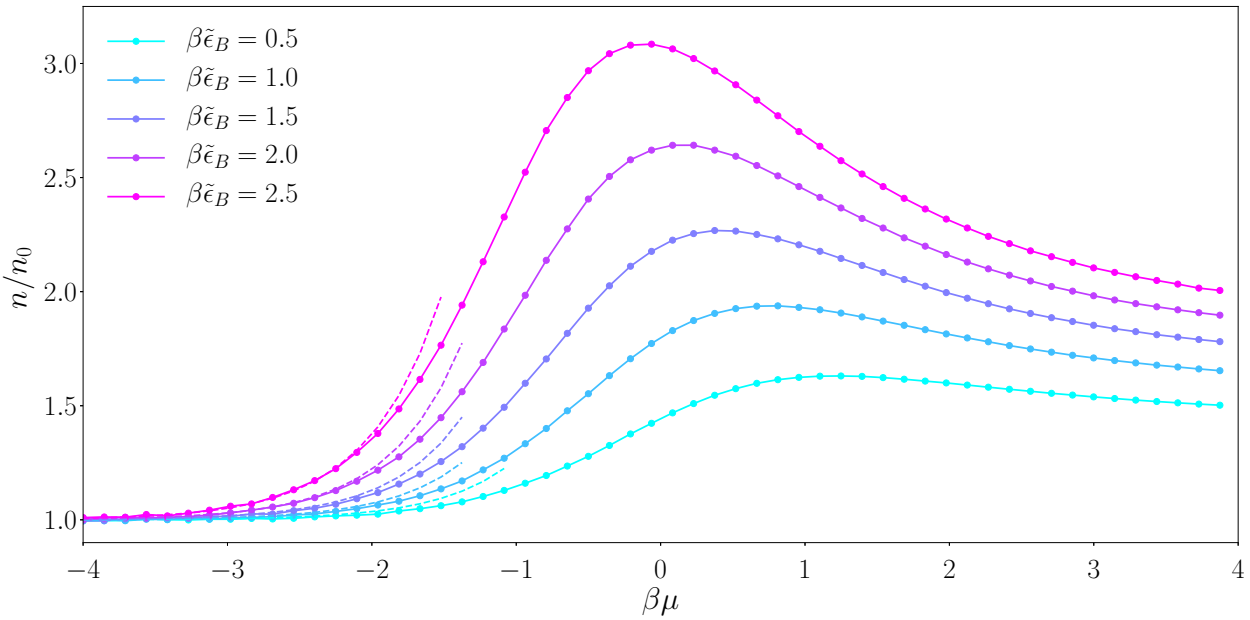

Figure 5.3: Total particle number density of the many-body system in terms of the noninteracting result, showing an increase in density with increasingly attractive interactions. Dashed curves represent third-order virial approximations.

that the noninteracting energy increases, so that the magnitude of the ratio decreases. Another possible explanation is that as the density grows, higher and higher momentum states must be occupied, driving up the kinetic energy. Trimers also come into closer contact with one another, contributing to fermionic repulsion.

Following Ref. [127], the pressure may be computed as

$$P\lambda_T^3 = 2\pi \int_{-\infty}^{\beta\mu} d(\beta\mu)' \; n\lambda_T, \tag{5.48}$$

where n is the total particle density and λ_T is the thermal wavelength. The results are plotted in Fig. 5.5, where the trend generally mirrors that of the particle density in Fig. 5.3.

The compressibility indicates how a system's density would respond to an applied pressure. In Fig. 5.6 (left), the total compressibility (accounting for all fermion flavors) initially *increases* over that of the noninteracting system. This increase is likely due to the fact that, for small densities, a compression is likely to bring the previously sparse particles into closer proximity to one another, leading to a favorable decrease in energy through the attractive interaction. Once the particles no longer need an outside "push" to help them find each other, the fermionic trimers prefer to keep their distance, and the compressibility drops significantly in comparison to the noninteracting case.

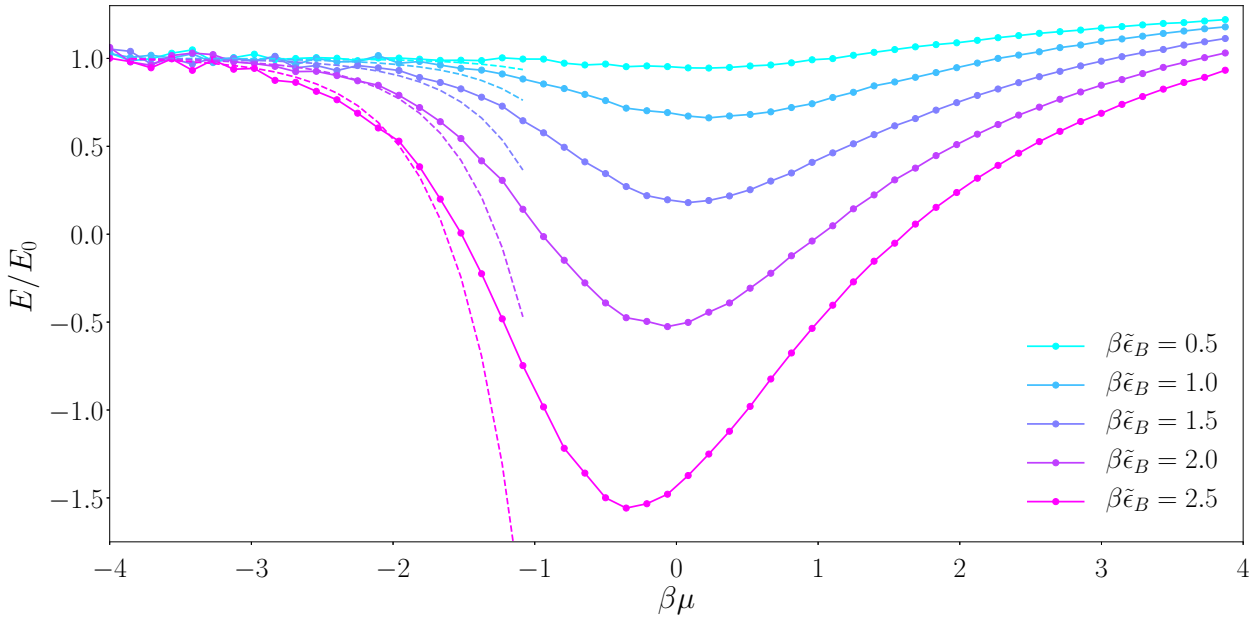

Figure 5.4: Total energy of the many-body system in terms of the noninteracting result, showing the expected decrease in energy for increasingly attractive interactions. Dashed curves represent third-order virial approximations.

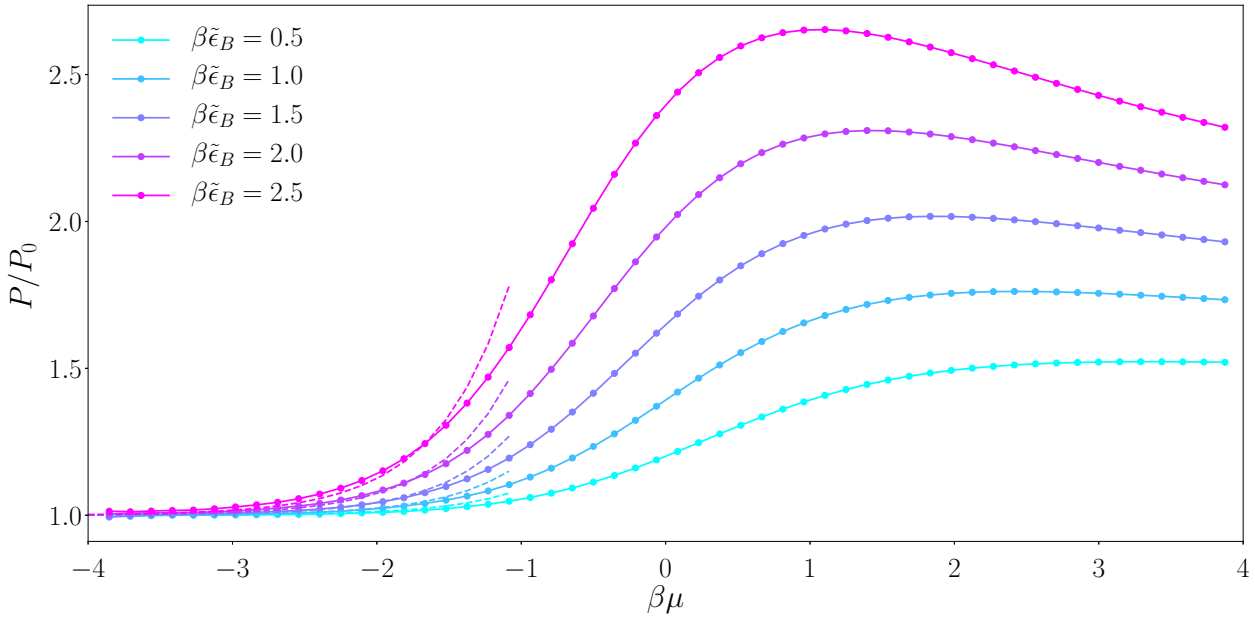

Figure 5.5: Pressure of the many-body system in terms of its noninteracting counterpart, where dashed curves represent the third-order virial approximation.

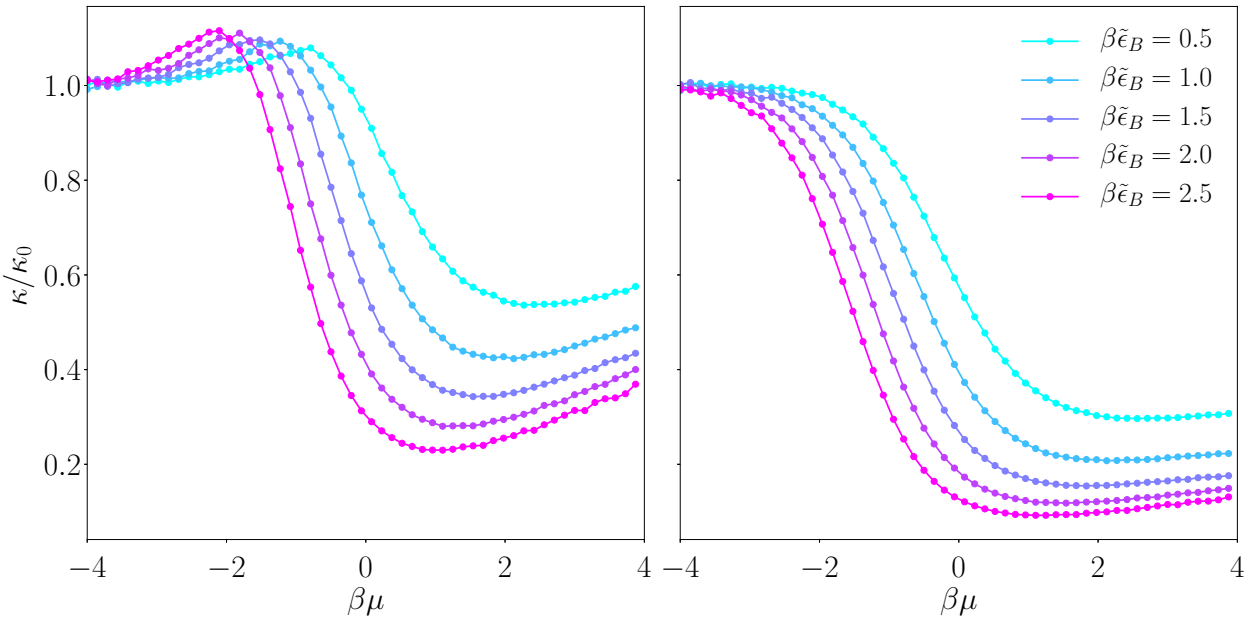

Figure 5.6: Total (left) and per-flavor (right) isothermal compressibility of the many-body system in terms of the noninteracting result.

In the right panel of Fig. 5.6, the compressibility of an individual fermionic species does not show the initial peak seen in the total compressibility; instead, it differs little from the noninteracting system. Since all three flavors are required for an interaction to take place, compressing only one flavor would not appreciably raise the likelihood of an interaction.[11] It *would*, however, bring like-flavor fermions closer together, which is generally unfavorable. Once the density is high enough that a considerable number of interactions are taking place, the individual fermion flavors' compressibility decreases below that of the noninteracting system: The fermions are already situated favorably, and compression would only push them away from their attractive centers. This stiffness against compression is more pronounced for individual flavors than for the total system, as compressing all flavors equally would not disrupt the favorable interactions.

The magnetic susceptibility quantifies the response (typically, degree of polarization) to an applied magnetic field. In our case, χ_1 responds an overall chemical potential that would tend to affect the total density, while χ_2 and χ_3 correspond to imbalances among the three fermion flavors. Similarly to the total compressibility,[12] χ_1 shows (Fig. 5.7, left) an initial increase over the noninteracting case, as the dilute system can quickly decrease its energy by adding more particles—up to a point. Past a certain density, it becomes increasingly difficult to accomodate more fermions in an increasingly crowded space.

[11] For a two-body interaction, this may not be the case.

[12] In fact, χ_1 is closely related to the total compressibility: $\kappa \langle M_1 \rangle^2 = L\chi_1$.

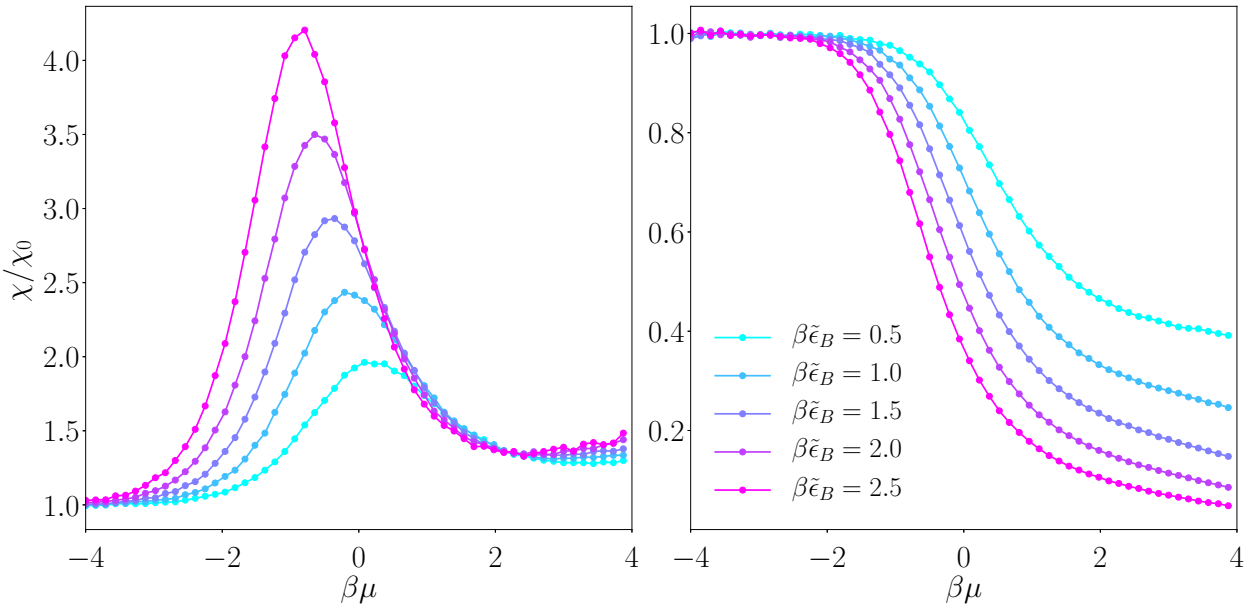

Figure 5.7: Overall (χ_1; left) and polarizing (χ_2, χ_3; right) isothermal magnetic susceptibility of the many-body system in terms of the noninteracting result.

The two susceptibilities associated with polarization (Fig. 5.7, right) also parallel the results for the flavor-wise compressibility. At low densities, polarization has little effect because interactions are scarce. Adding or removing particles of only one or two flavors would have a negligible impact on the potential energy but a sizable effect on the kinetic energy, so that the susceptibility is approximately equal to the noninteracting case. Once the density allows significant contributions from the interactions, however, no amount of polarization is beneficial: Adding particles of a single flavor increases kinetic energy with no corresponding decrease in potential energy, and removing particles of a single flavor destroys favorable interactions that were taking place. The system is thus "locked in" once a certain density is reached and largely resists external influences.

The contact is a thermodynamic quantity which, in our case at least, measures the likelihood of particles of all three species co-occurring at one location. As we saw earlier, in classical, continuous space, this likelihood is infinitesimal, and the contact vanishes. With a δ-function interaction, the system is scale-invariant, and no bound state forms. As we also saw, this is not the case quantum mechanically; at last, we encounter results for the breaking of scale invariance in the many-body problem.

The two measures of the contact density, given by Eqs. (5.39) and (5.38), are plotted in dimensionless, intensive form in Fig. 5.8 (left and right, respectively). Unsurprisingly, in both panels, the contact increases with coupling strength and with density—the stronger the interaction, the greater the anomaly. The pressure-energy difference of Eq. (5.38), however, gives lower magnitudes for the contact, which also appears to taper

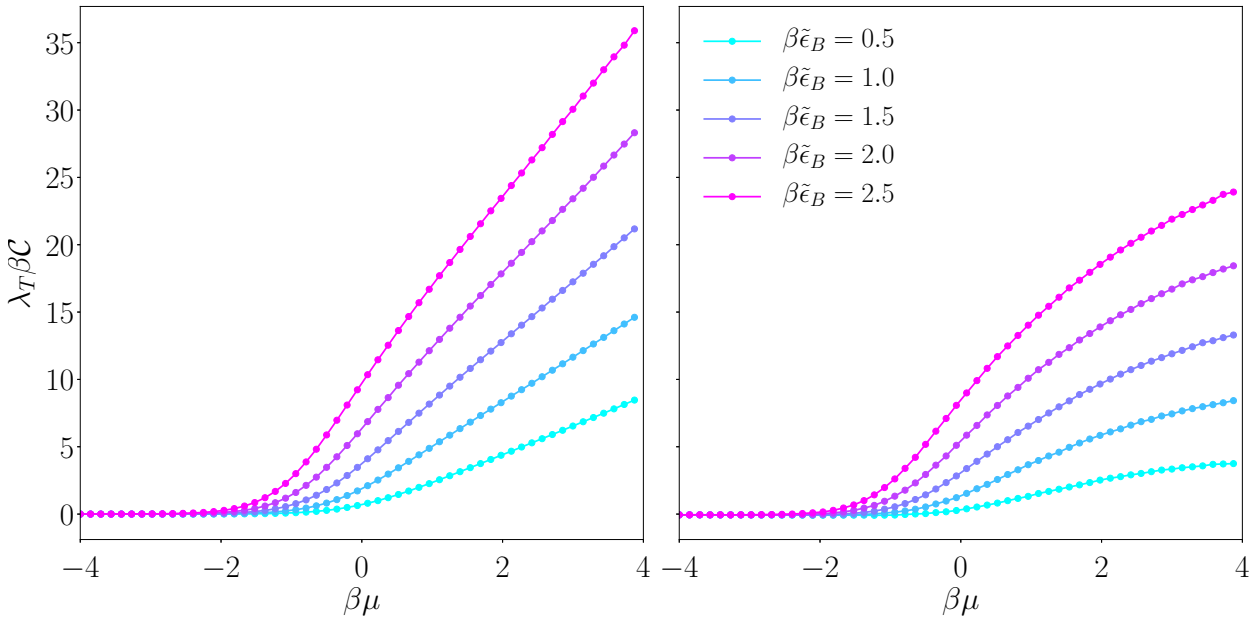

Figure 5.8: Contact density from expectation value of potential energy (left) and from pressure-energy difference (right).

off at larger fugacities. We suspect that this decrease is due primarily to lattice effects which are exaggerated in Eq. (5.38) but are not as severe in Eq. (5.39).

First, the derivation of Eq. (5.38) (not shown here) assumes Galilean invariance, which is broken by the discrete lattice. Second, the calculation of the pressure relies on an integral over $\beta\mu$ (Eq. (5.48)). The effective intervals of μ in this integral are shortened by the fact that the Hubbard dispersion relation for the kinetic energy decreases from $p^2/2m$ at an increasing rate for higher momentum modes, which become occupied at larger fugacities. As a result, the "area under the curve" is diminished, yielding a smaller pressure and thus smaller contact. Still, this effect may be offset by the corresponding decrease in E due to the smaller kinetic energy. The potential energy may also be affected by these considerations, and its apparently more correct results for the contact may be misleading. However, in this work, we regard Eq. (5.39) (Fig. 5.8, left) as the more reliable result; more careful analysis would require further numerical investigations that account for corrections to the Hubbard dispersion.

Finally, we return to the question of the formation of composite fermions first addressed in Ref. [66] and further explored in Ref. [103]. As previously intimated, we expect a "Fermi-Fermi crossover," whereby in the passage from noninteracting to strongly interacting, the system transitions from a mixture of three ideal Fermi gases to a single ideal Fermi gas of composite trimers (equivalent to a hard-core Bose gas [128]).

Just as we ruled out a bound hexamer state by comparing the six-body energy to the energy of two isolated trimers at the same coupling strength, we may compare the many-body energies to the corresponding energies

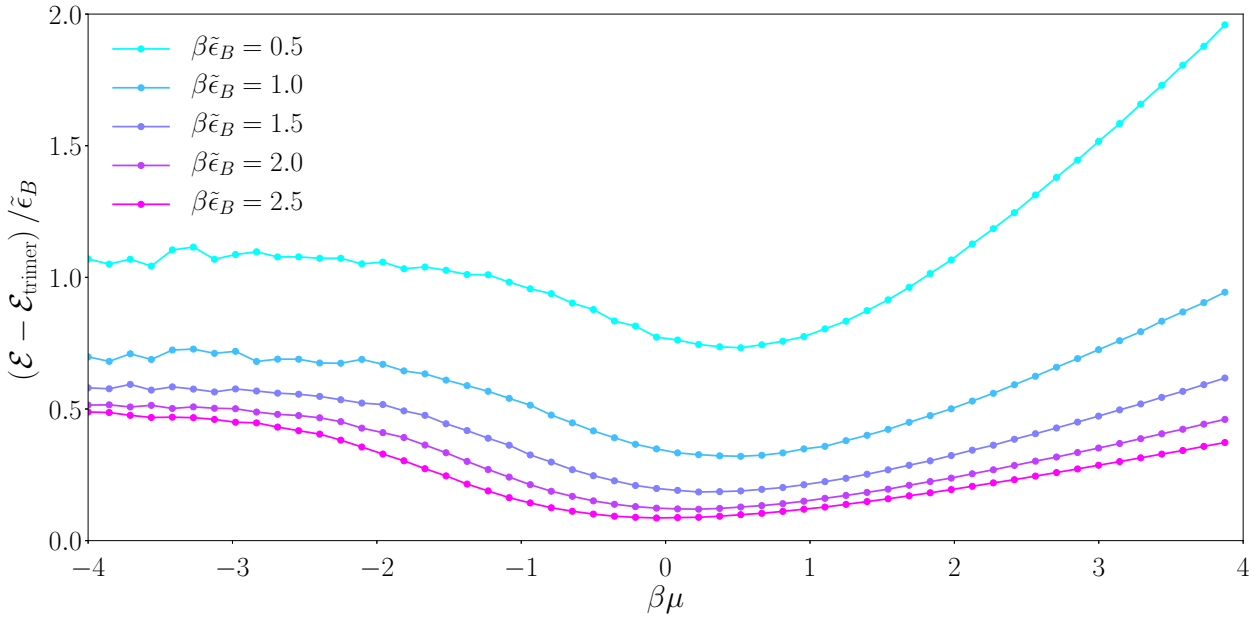

Figure 5.9: Difference in energy per particle from ideal gas of fermionic trimers (in units of $\tilde{\epsilon}_B$), suggesting that the residual interaction between real trimers is repulsive.

of gases composed of ideal trimers at the same temperature, coupling, and particle number. Specifically, we first tune the ideal trimer chemical potential so that $3N_{\text{trimer}} = N$, where N_{trimer} is found from the grand canonical expectation for an ideal Fermi gas with mass $3m$. The energy of the trimer gas then takes the binding energies into account as $E_{\text{trimer}} = \langle E \rangle_{\text{trimer}} - \tilde{\epsilon}_B N_{\text{trimer}}$, where the energy expectation is the kinetic energy of a grand canonical ideal Fermi gas with mass $3m$.

In Fig. 5.9, the result of this procedure is displayed for each coupling strength, where energy per particle is shown in units of the binding energy $\tilde{\epsilon}_B$. The positivity of each curve indicates that, just as for the six-body case, the effective interaction between trimers is repulsive—no attractive many-body effects develop (which could not be ruled out by few-body considerations alone). Additionally, the fact that each successively larger coupling strength is closer to the ideal Fermi gas of trimers suggests that the Fermi-Fermi crossover is the correct interpretation of the transition from weak to strong coupling in the many-body problem. As the attraction grows, large, repulsive trimers become point-like, noninteracting composite particles.

Section 5.6: Summary and conclusion

By formulating the problem in the lattice worldline representation, using the Hubbard dispersion relation and the worm algorithm, we have obtained thermodynamic information about the fermionic many-body problem with a three-body interaction in 1D. By analyzing the energy and linear response functions, we

provided evidence for the formation of repulsive trimers which resist being broken up by external fields. With a high degree of confidence, we claim that our earlier predictions have been verified: As the coupling increases from weak to strong attraction, the system undergoes a Fermi-Fermi crossover. Three initially noninteracting ideal Fermi gases pass through a phase of existing as diffuse, repulsive trimers to become, once again, an ideal Fermi gas—only composed of more massive, composite particles. Furthermore, we directly quantified the breaking of classical SO(2,1) scale invariance in the many-body problem, posited already in the simplest (three-body) case, by means of the contact density.

While we did not study the many-body problem in the presence of a harmonic oscillator potential, the worm algorithm as described in this chapter can easily be adapted to include one. The algorithm may also be modified to include two- and four-body forces, as well as additional species of fermions, providing several new avenues of worthwhile research.

This concludes our study of the anomalous three-body contact interaction in 1D. While the experimental feasibility of our model is as yet unknown, our results provide a first set of predictions for the few- to many-body behavior of the model. While this chapter has a flavor of finality, our investigations into three-body interactions are not quite through [129].

CHAPTER 6: TRIANGULAR LATTICE MODEL FOR THREE-BODY INTERACTIONS

In this final chapter, we change gears slightly and examine a lattice model with a three-body interaction. Here, the lattice is not a numerical approximation to the continuum; rather, it forms the backbone of the model itself, where classical "spins" are situated at fixed lattice sites and may "flip" or "rotate" to achieve an optimal configuration.

Before delving into the details of the proposed model, we give a brief introduction to the study of lattice models. Using the well-known Ising model as a case study, we will illustrate the relevant principles, including the choice of update algorithm, analysis and characterization of numerical results, and relation to physical theory.

Section 6.1: The Ising model

In 1925, Ising [130] introduced the simple model that now bears his name. Hoping to capture the behavior of ferromagnetism from first principles—namely, the spontaneous transition from a disordered phase to bulk magnetization at the Curie temperature—Ising proposed a lattice model consisting of "up" spins and "down" spins (magnetic dipoles) with short-range interactions. After solving his model in 1D and finding no phase transition, Ising concluded that his model had failed [131].

In reality, had Ising solved his model in a dimension $d > 1$, he would have found the phase transition he sought. In 1941, Kramers and Wannier [132, 133] studied the model in 2D, finding the critical temperature by relating high- and low-temperature expansions (the so-called Kramers-Wannier duality [114, 134]). Still, this solution was only approximate; the transfer matrix formalism they introduced, which solved the 1D problem exactly, could not be easily extended to the 2D case. Three years later, Onsager [135] finally solved the 2D problem exactly (using quaternions), firmly establishing the existence of a phase transition in the Ising model.

While more sophisticated lattice models followed the Ising model—such as the Potts, XY, and Heisenberg models—the Ising model has remained the most well known. Its basic importance stems from its demonstration that short-range, local interactions can give rise to long-range, collective phenomena such as phase transitions. As a result, the Ising model continues to be a valuable tool for developing intuition in related models and is commonly introduced in undergraduate courses.

The Hamiltonian for the Ising model is

$$H = -J \sum_{\langle ij \rangle} s_i s_j + h \sum_i s_i, \tag{6.1}$$

where $\langle ij \rangle$ denotes pairs of nearest-neighbor lattice sites, and the "spins" take on the values $s_i = \pm 1$. The model is ferromagnetic for couplings $J > 0$ and antiferromagnetic for $J < 0$; here, we focus on $J > 0$. The external magnetic field strength h can be positive, negative, or zero, and determines whether a particular spin orientation is preferred; unless otherwise specified, we set $h = 0$. We will now briefly outline the solution of the 1D Ising model to introduce the idea of the transfer matrix.

Defining $K = \beta J$, the 1D Ising partition function is given by

$$\mathcal{Q} = \sum_{\{c\}} e^{K \sum_i s_i^c s_{i+1}^c} = \sum_{\{c\}} \prod_i e^{K s_i^c s_{i+1}^c}, \tag{6.2}$$

where c indicates the 2^N lattice configurations, and we have assumed periodic boundary conditions so that $s_0 = s_N$. Introducing the *transfer matrix*

$$T = \begin{pmatrix} e^K & e^{-K} \\ e^{-K} & e^K \end{pmatrix}, \tag{6.3}$$

the partition function may be rewritten as

$$\mathcal{Q} = \mathrm{Tr}\left(T^N\right), \tag{6.4}$$

where N is the number of spins. Casting the partition function as a series of matrix products incorporates the necessary sums and products in $\mathcal{Q}$ while also maintaining the connectivity between neighboring sites imposed by the Hamiltonian. In general,

$$\mathrm{Tr}\left(T^N\right) = \sum_i \lambda_i^N, \tag{6.5}$$

where the λ_i are the eigenvalues of T, and thanks to the Perron-Frobenius theorem [114], there is guaranteed to be a largest eigenvalue λ which dominates all others as $N \to \infty$. For the matrix T, this eigenvalue is $\lambda = 2 \cosh K$, so that

$$\mathcal{Q} = 2^N \cosh^N K. \tag{6.6}$$

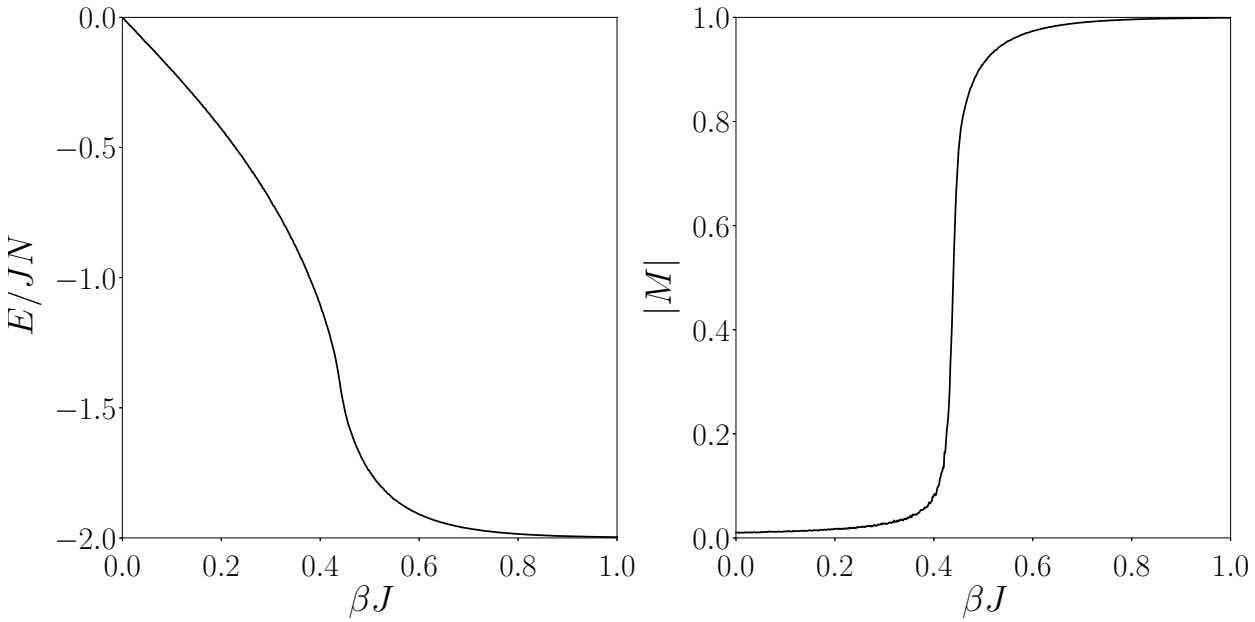

Figure 6.1: Energy (left) and magnetization (right) in the 2D Ising model for a square 80×80 lattice.

From this result, the energy may be obtained as

$$E = -\frac{\partial}{\partial \beta} \ln \mathcal{Q} = -JN \tanh(\beta J). \tag{6.7}$$

If the magnetic field h is retained, the average magnetization may similarly be found as

$$M = \frac{1}{N} \left\langle \sum_i s_i \right\rangle = -\frac{1}{N} \frac{\partial}{\partial (\beta h)} \ln \mathcal{Q} = \frac{e^{\beta J} \sinh(\beta h)}{\sqrt{e^{2\beta J} \sinh^2(\beta h) + e^{-2\beta J}}}. \tag{6.8}$$

For $h \to 0$, M vanishes, as the "up" and "down" orientations of the fully aligned lattice are equally likely and cancel. More importantly, consistent with Ising's findings, the energy and magnetization per lattice site are both smooth functions at all temperatures, showing no evidence of a phase transition.

Turning to the 2D model, where we *do* expect a phase transition, we employ Monte Carlo rather than using Onsager's solution. In Fig. 6.1, the slope of the energy approaches an asymptote at the critical inverse temperature $\beta_c \approx 0.4\ J^{-1}$; the slope of the magnetization is even sharper. Both of these curves reflect the behavior of thermodynamic quantities in the vicinity of a second-order phase transition (where the second derivative of the partition function diverges). With increasing lattice sizes, both curves would become infinitely steep at β_c.

In Fig. 6.2, 2D Ising lattices are displayed at several temperatures on both sides of the phase transition.

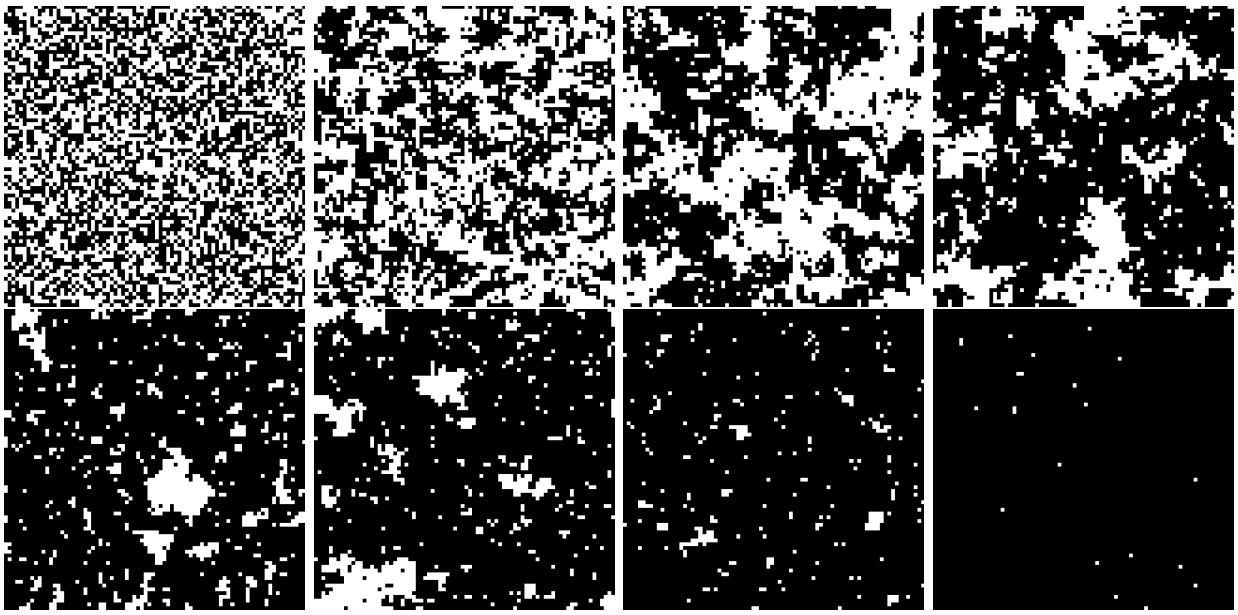

Figure 6.2: Ising spins on an 80×80 lattice, where black and white indicate opposite spins. In reading order from top left: $\beta J = 0$, $\beta J = 0.3$, $\beta J = 0.41$, $\beta J = 0.43$, $\beta J = 0.44$, $\beta J = 0.45$, $\beta J = 0.5$, $\beta J = 0.8$.

At temperatures above T_c (top row), black and white (up and down) appear in roughly equal numbers, and domains grow in area as the temperature drops. Once the temperature falls below T_c (bottom row), black dominates the lattice, which becomes one large domain as the temperature approaches zero.

As a final characterization of the 2D Ising model, we now apply Principal Component Analysis (PCA) to the Monte Carlo data. PCA reduces the dimensionality of a problem by taking a rectangular matrix X and performing an eigenvalue decomposition on the (symmetric) square matrix $X^T X$. The "principal components" are those eigenvectors with the largest eigenvalues,[1] and these vectors account for the greatest amount of variation in the data. For example, PCA carried out on a 2D Gaussian distribution would yield the principal components as the two axes of the ellipse (Fig. 6.3).

The matrix X is constructed from many lattice configurations at different temperatures as follows. Each row is formed by linearizing the 2D lattice of spin values at a given temperature into a 1D vector, so that each column of X corresponds to a single lattice site. As a result, provided that the possible values of spin s are symmetrically distributed around zero, the components of $X^T X$ can be interpreted as spin correlations

[1]The non-negativity of the eigenvalues of $X^T X$ can be proven as follows. As a real symmetric (Hermitian) matrix, the eigenvalues of $X^T X$ are real. For an eigenvector $\mathbf{v}$ with eigenvalue λ, consider the scalar product $\mathbf{v}^T X^T X \mathbf{v} = \lambda |\mathbf{v}|^2$. In a normed vector space, $|\mathbf{v}| > 0$ for $\mathbf{v} \neq \mathbf{0}$. Regrouping the product, we also have $\mathbf{v}^T X^T X \mathbf{v} = |X\mathbf{v}|^2 \geq 0$. As a result, $\lambda |\mathbf{v}|^2 = |X\mathbf{v}|^2 \geq 0$, so that $\lambda \geq 0$ in general, and eigenvalues can be assigned a definite order (up to degeneracy).

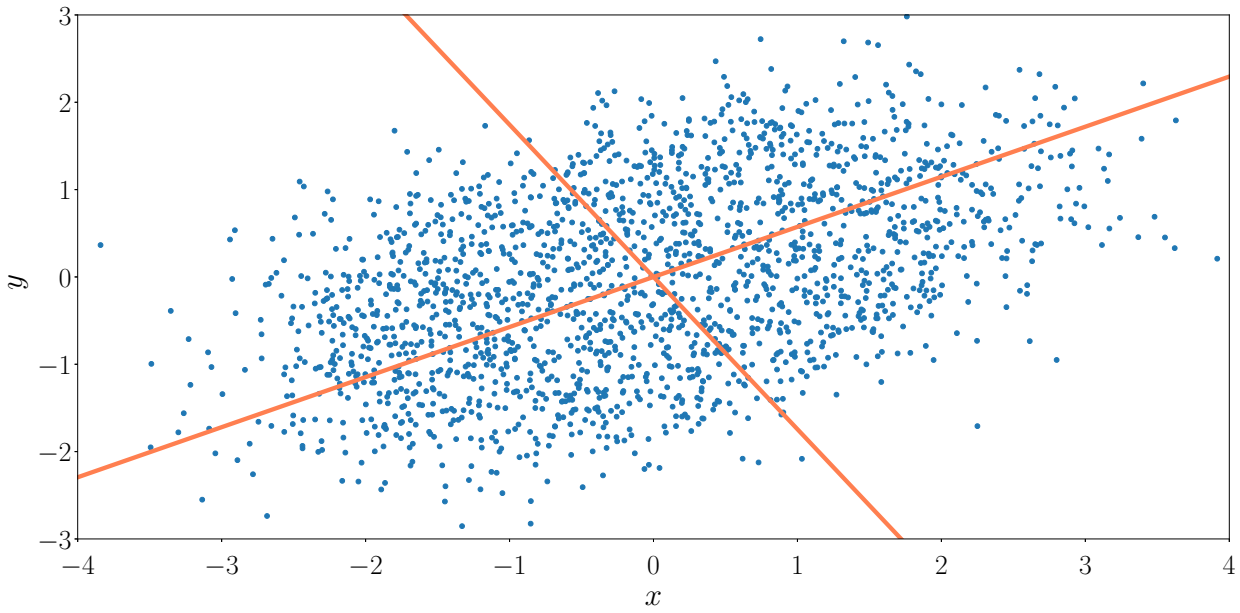

Figure 6.3: Axes (orange lines) determined from two largest components from PCA, with only a matrix built from the sample points' coordinates as input. The underlying distribution is a centered 2D Gaussian with variances 1 and 1/3, rotated by an angle $\pi/3$ from the x-axis. The angles of the computed axes differ from the true values by less than 2%.

between sites i and j of the lattice, averaged over different temperatures:

$$\left(X^T X\right)_{ij} \propto \sum_{\beta} \langle s_i s_j \rangle_{\beta} \,, \tag{6.9}$$

where each covariance $\langle s_i s_j \rangle_{\beta}$ is computed from all of the lattice samples of inverse temperature β. As correlations grow at lower temperatures, the sum is dominated by the large-β terms. The principal components of $X^T X$ thus correspond to a basis of vectors that maximize intersite spin correlations. Projecting X onto these components yields vectors whose entries measure the degree of similarity between individual lattice samples and the eigen-lattices of maximal spin correlation: Large values, typically associated with low temperatures, indicate ordered lattices, while small values, associated with high temperatures, characterize disordered lattices.

As highlighted by Ref. [136], PCA can be used to discover structural features in lattice models. When applied to the 2D Ising model, the two leading components reveal not only the existence of a phase transition, but also the degeneracy of the ground state. Since the energy of the lattice is unchanged by a simultaneous flip of all spins, the Ising model possesses a global Z_2 symmetry. At temperatures below the phase transition, PCA is able to characterize this degeneracy, as indicated by the two low-temperature clusters in Fig. 6.4.

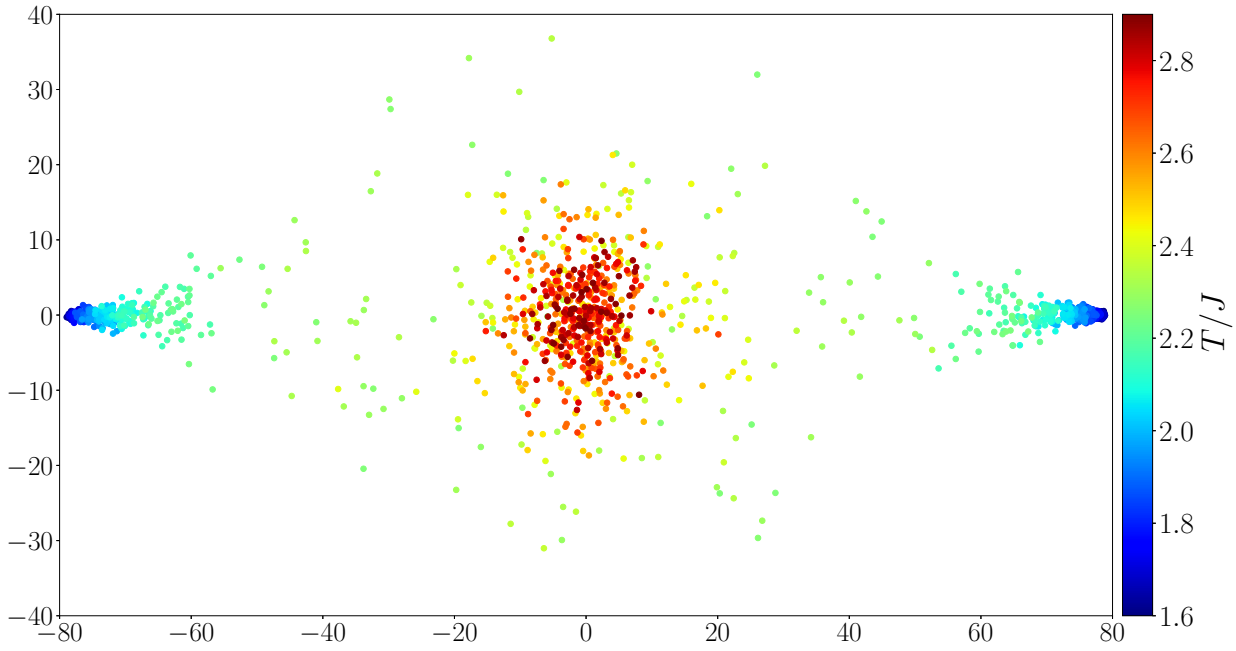

Figure 6.4: Scatter of projection onto the two largest PCA components of the 2D Ising model at various temperatures. At high temperatures, no features are apparent, but the Z_2 symmetry becomes evident below the critical temperature.

Section 6.2: The three-body lattice model

Just as the three-body interactions considered previously only featured a contribution when three fermions of different flavors collided, we here consider a Hamiltonian that only involves sets of three neighboring lattice sites at a time:

$$H = -J \sum_{\langle ijk \rangle} \left(1 - \delta_{s_i s_j}\right) \left(1 - \delta_{s_j s_k}\right) \left(1 - \delta_{s_k s_i}\right), \tag{6.10}$$

where $J > 0$ is the coupling, $\langle ijk \rangle$ indicates sets of neighboring sites, and s_i, etc. represent the value of the spin at site i (-1, 0, or 1).[2] In keeping with the fermionic nature throughout this work, Eq. (6.10) requires the spins to all be different for any interaction to take place. While there is no explicit repulsion between like spins, an overall constant added to the energy would achieve this effect without changing the physics; the repulsion would not be stronger for three neighboring like spins than for two, however.

As it is preferable for the Hamiltonian to be written in terms of functions (rather than the Kronecker-δ), we now demonstrate that Eq. (6.10) can be recast in terms of simple trigonometric functions. Using the

[2] As far as the Hamiltonian is concerned, the actual values the spins take on are arbitrary.

complex-exponential form of the Kronecker-δ in a 3D basis,

$$\delta_{jk} = \frac{1}{3}\sum_{n=-1}^{1} e^{i\frac{2\pi}{3}n(j-k)} = \frac{1}{3} + \frac{2}{3}\cos\left(\frac{2\pi}{3}(j-k)\right), \tag{6.11}$$

each factor in (6.10) can be written as

$$1 - \delta_{s_j s_k} = \frac{2}{3}\left[1 - \cos\left(\frac{2\pi}{3}(s_j - s_k)\right)\right], \tag{6.12}$$

so that after application of a trigonometric identity, the Hamiltonian becomes

$$H = -\frac{64J}{27}\sum_{\langle ijk\rangle} \sin^2\left(\frac{\pi}{3}(s_i - s_j)\right)\sin^2\left(\frac{\pi}{3}(s_j - s_k)\right)\sin^2\left(\frac{\pi}{3}(s_k - s_i)\right). \tag{6.13}$$

Since what it means for three sites to be "neighbors" depends on the geometry of the lattice—in particular, the coordination number—we must choose the geometry wisely. While the Ising model is typically formulated on a square lattice, we employ a triangular lattice for the three-body interaction to avoid what is known as *frustration*. Since a triangular lattice consists of "plaquettes" (the region defined by the smallest closed polygon that can be formed by linking nearest neighbors) with three vertices, its geometry naturally suits the three-body interaction. Rather than the bonds linking two neighboring spins in the Ising model, the smallest interacting unit in our model consists of a triangular plaquette whose vertices are each in different orientations (see Fig. 6.5). If we were to formulate this model on a square lattice, it would be impossible to achieve a maximally interacting lattice configuration, and hence the lattice would be frustrated. Even on a triangular lattice (with periodic boundary conditions), the number of sites in each dimension of the 2D lattice must be a multiple of six to avoid frustration. Here, we choose equal numbers of sites L in each dimension, such that the total number of lattice sites is $N = L^2$, and the number of plaquettes is $N_p = 2N$.

Given the Hamiltonian (6.10), the partition function for this model is

$$\mathcal{Q} = \sum_{\{c\}} e^{\beta J\sum_{\langle ijk\rangle_c}\left(1-\delta_{s_i s_j}\right)\left(1-\delta_{s_j s_k}\right)\left(1-\delta_{s_k s_i}\right)} = \sum_{\{c\}}\prod_{\langle ijk\rangle_c} e^{\beta J\left(1-\delta_{s_i s_j}\right)\left(1-\delta_{s_j s_k}\right)\left(1-\delta_{s_k s_i}\right)}, \tag{6.14}$$

where the sum is over the set of all possible lattice configurations c. After carrying out the product over plaquettes $\langle ijk\rangle_c$ in each configuration, the partition function reduces to

$$\mathcal{Q} = \sum_{\{c\}} e^{\beta J n_c} = \sum_{n_c=0}^{N_p} g(n_c)\, e^{\beta J n_c}, \tag{6.15}$$

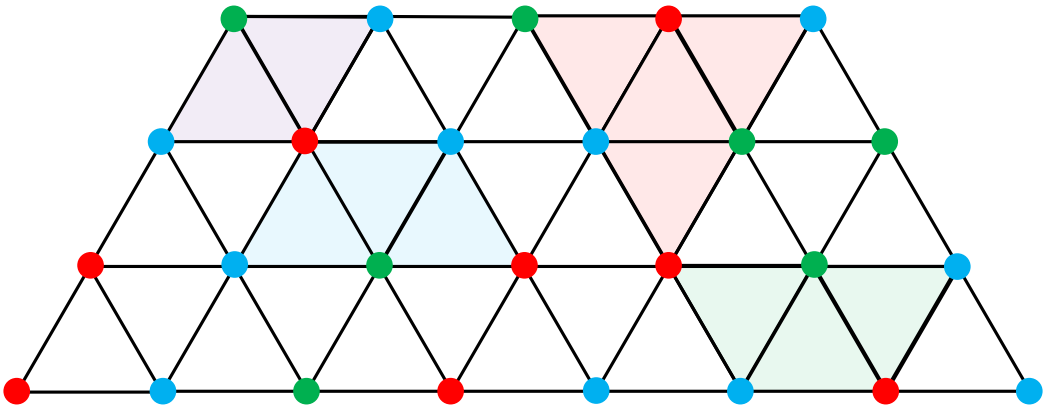

Figure 6.5: Example segment of triangular lattice, where shaded plaquettes of different colors indicate interactions with incompatible orientations. Red, blue, and green vertices represent the three possible spin orientations at each site.

where n_c is the number of interacting plaquettes in the configuration c, and $g(n_c)$ is a weight function accounting for all possible configurations.

Just as in the 2D Ising model, we primarily rely on Monte Carlo to obtain results for the three-body lattice model. As described in the previous chapter, to satisfy detailed balance, Eq. (5.25) is insufficient when the set of possible outcomes has more than two options. Instead, we again employ the ternary transition probabilities exemplified by Eq. (5.31). The first result of this procedure, the energy per lattice site as a function of inverse temperature, is displayed in Fig. 6.6, demonstrating a high degree of convergence with increasing lattice sizes.

Section 6.3: Considerations for a cluster update algorithm

The most straightforward way of carrying out Monte Carlo in the Ising (and similar) models is by using *local* updates, which consider changes to only one lattice site (spin) at a time. While this is the easiest method both in concept and in practice, it does have its drawbacks. Chief among these is the occurrence of "critical slowing down," which becomes a problem in the neighborhood of critical points. Because critical phenomena involve the development of long-range correlations—the divergence of correlation lengths is a key marker of criticality—local updates struggle to effectively capture such behavior. Each local update is statistically independent of previous ones, so that it takes a very long time for large clusters to form. One

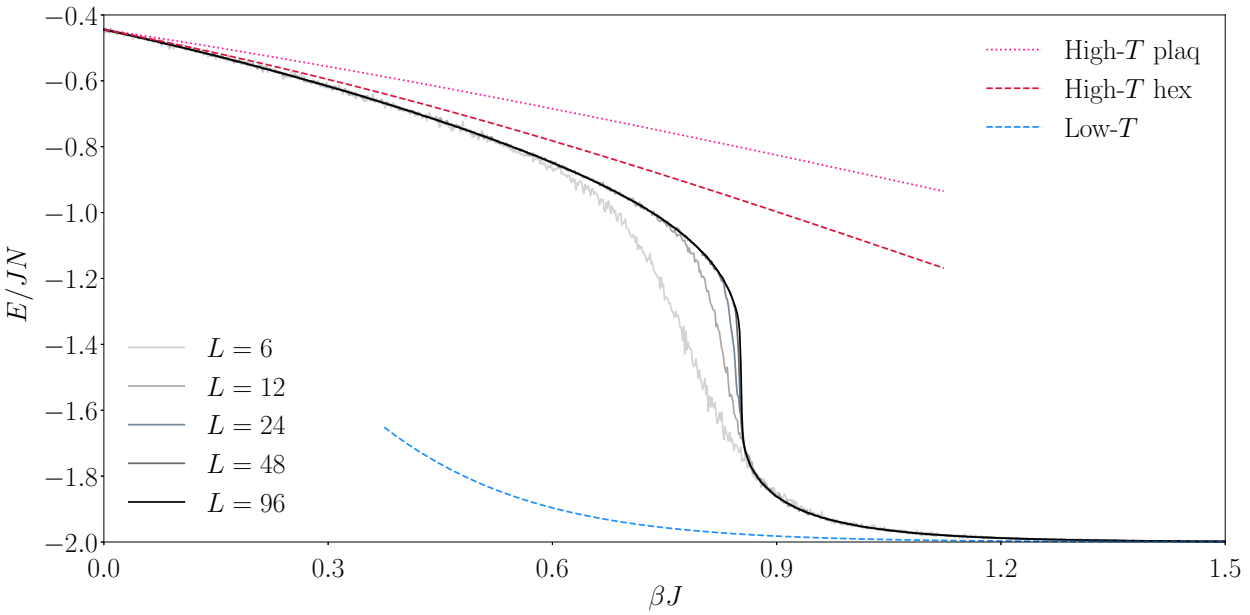

Figure 6.6: Energy per lattice site of the three-body model, where the thermodynamic limit is approached with increasing darkness of curves. Also shown: approximations for single plaquette at high temperature (dotted pink), hexagon at high temperature (dashed red), and hexagon at low temperature (dashed blue).

must wait for the update to chance upon the boundary of the growing cluster, but the probability of the boundary being landed on randomly tends to zero in the thermodynamic limit.[3] Since large-scale changes slow down significantly, samples modified by local updates are highly correlated, and an increasing number of updates must be carried out before samples become statistically independent [137].

To overcome the difficulties of critical slowing down associated with local updates, *cluster* update algorithms have been developed, which update many lattices sites at once. The most efficient cluster algorithm developed for the Ising model to date is the Wolff algorithm [138], which builds clusters whose size tends to grow with decreasing temperatures: given that one lattice site is in the cluster, the probability for each of its neighboring sites to be added to the cluster is $p = 1 - e^{-2\beta J}$. The Wolff algorithm is rejection-free,[4] so that proposed updates are *always* accepted while still satisfying detailed balance.

As described in Ref. [139], the Wolff algorithm is built by recursively considering the probability of adding (or not adding) same-spin neighbors of lattice sites to the cluster. Since the Ising model has only two possible spin values, it is straightforward to compare the statistical weights of a cluster before and after flipping it. By following similar reasoning, we may construct a cluster algorithm for the three-body model

[3] In d-dimensional space, the probability of randomly choosing a boundary location (with size L^{d-1}) out of the whole volume (with size L^d) scales as L^{-1}; the thermodynamic limit sends $L \to \infty$.

[4] Other values of p would be valid, but would not be rejection-free.

on the triangular lattice as follows.

First, randomly choose a plaquette that is in an interacting configuration. Its neighbors are those plaquettes that share an edge (two vertices); if they are in the same phase orientation, they are added to the cluster with probability p (not yet specified), and so on for each of their neighbors. Once the cluster is constructed, it is collectively "flipped" to a new orientation with some probability P (to be determined). This "flip" is carried out by performing a permutation on the values of all of the lattice sites belonging to plaquettes in the cluster.

Now, we must determine the probabilities p and P. To do so, collect the cluster plaquettes' neighboring plaquettes that were not added to the cluster, whether by non-compatibility of orientation or by failure to meet the probability p. This set of plaquettes is the same before and after the flip ("set A"). Find the vertices that are members of both set A and of the cluster, then collect those plaquettes to which these vertices belong that are neither in the cluster nor in set A. These plaquettes form "set B", also the same before and after a flip. Define x as the number of interacting plaquettes in set B.[5] Then, if we choose $p = 1 - e^{-\beta J}$, the probability P of flipping the cluster from its initial configuration to a new one is given by

$$P(i \to f) = \min\left\{1, e^{\beta(x_f - x_i)}\right\}, \tag{6.16}$$

where x_i and x_f are values of x before and after the flip, respectively. This algorithm is thus not rejection-free, but it still may prove more efficient than the local update scheme.

Carrying out this cluster update, the energy (not shown) appears very similar to that obtained with the local update, shown in Fig. 6.6. A phase transition still appears to occur, but with a higher critical temperature, appearing closer to $\beta J \approx 0.6$. Why the disagreement? It turns out that this cluster algorithm does not actually obey detailed balance; the critical step lies at the very beginning of the procedure.

As laid out clearly by Ref. [139], the probability of carrying out a Monte Carlo update consists of not only the probability of accepting vs. rejecting, but also of the probability of *proposing* any given change. In formulating proposals, we must not introduce any undue bias to a particular region of configuration space (this is the requirement of *ergodicity*). Notice that in the first step of this algorithm, however, we chose a plaquette that was *already* in an interacting configuration. As a result, although the steps that follow may be in accord with detailed balance, we have restricted ourselves to updating only those regions which are immediate neighbors of interacting plaquettes; noninteracting plaquettes are never chosen as the starting point for an update. Ordered phases are thus preferentially chosen for updates at the exclusion of disordered

[5] In most cases, x is equal to the number of interacting plaquettes that are intersected by the boundary of the cluster and have only one vertex inside the cluster. While helpful for visualization, this is not always the case.

phases. The Wolff algorithm does not suffer from this deficiency, as any randomly chosen site can serve as the beginning of a cluster. To date, we have not discovered a suitable remedy for this bias and leave it for future work.

Section 6.4: Towards a transfer matrix solution

In the 1D Ising model, the transfer matrix formalism enabled an exact solution with minimal effort. There, construction of the transfer matrix boiled down to determining the repeated unit—single bonds—and accounting for the connectivity of neighbors in all of their possible configurations. Since there were only two nearest neighbors (both along the same axis), the transfer matrix products "hopped" along the lattice, joining two neighbors at a time by means of only one matrix multiplication (contraction of a single index, in tensor terms).

In the 2D Ising model, each lattice site is linked to *four* nearest neighbors (two in each dimension). The simplest repeating unit becomes a lattice site with a bond extending in both dimensions, forming half of the outline of a square. Since the "transfer" occurs along both dimensions, there are now *two* indices of contraction associated with each unit cell; the simple 1D problem of finding the largest eigenvalue of a 2×2 matrix becomes an involved problem in group theory, as expounded by Onsager [135]. Although there are two indices, each unit cell is still determined by only one free parameter—a single spin—just as in 1D.

In the three-body model, both the geometry of the triangular lattice and the nature of the interaction complicate the structure of the unit cell. As illustrated in Fig. 6.7, by linearizing the triangular lattice, we gain insight into the simplest repeating unit. Shown in blue, the unit cell contains four plaquettes and six lattice sites. Unlike in the Ising model, the unit cell contains *two* free parameters (the lattice sites labelled a_{00} and b_{00} in Fig. 6.7). As a result, the transfer matrix is characterized by three indices—two in the horizontal direction, and one in the vertical. Just as the 1D three-body interaction was effectively 2D, then, the three-body interaction in this model causes a 2D lattice to acquire an additional effective dimension.

In the Ising model, the transfer matrix formalism—particularly, the representation in terms of Pauli matrices—is enabled by the fact that the Hamiltonian features simple products of the values of neighboring spins. In the three-body model, on the other hand, the Hamiltonian is a function of the spin values which cannot be reduced to a simple product. As a consequence, a full group-theoretical treatment, if possible, is beyond the scope of the present work.

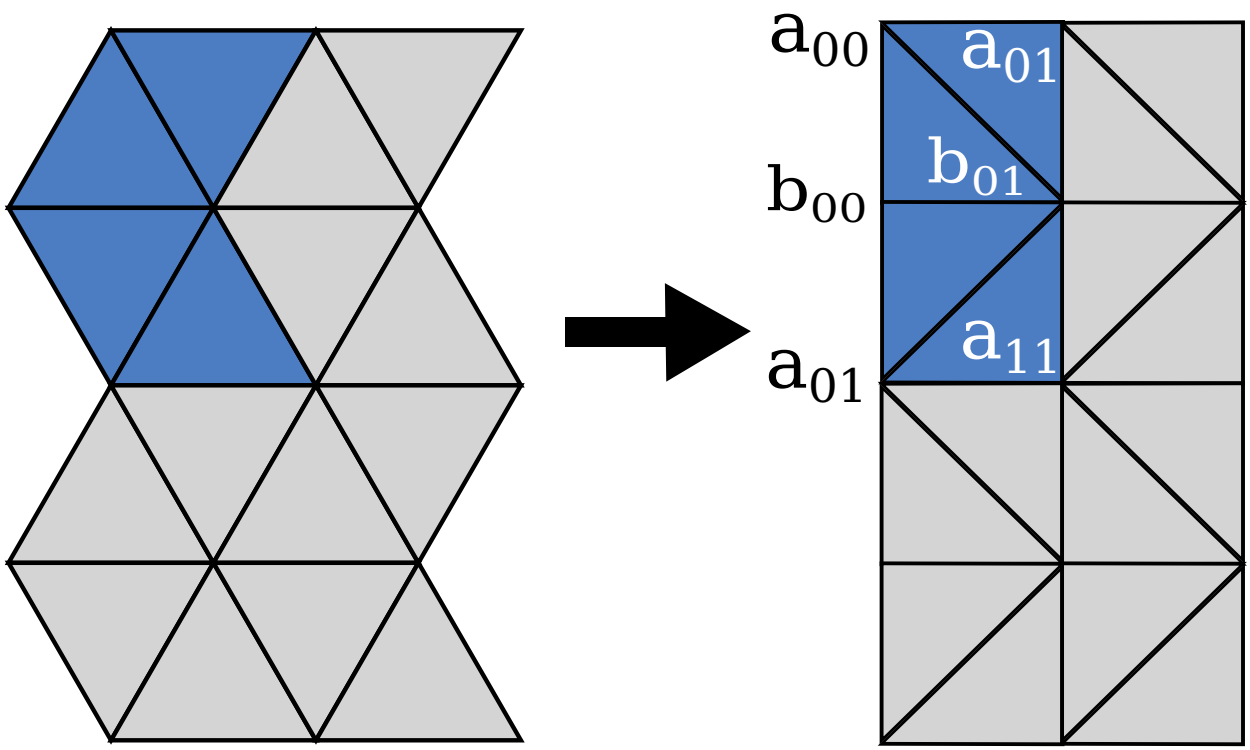

Figure 6.7: Linearized representation of triangular lattice, with unit cell shaded blue.

Section 6.5: Approximations at high and low temperatures

While the local Monte Carlo scheme described previously provides numerical results, a comparison to analytical results is desirable. Unfortunately, given the vast number of possible configurations of three flavors (3^N), the weight function $g(n_c)$ is enormously complicated. Thus, we now seek approximations in the limits of high and low temperatures.

At high temperatures ($\beta \to 0$), thermal effects dominate over interaction effects, and the orientation of any given spin becomes entirely random. Of the $3^3 = 27$ possible configurations of a single plaquette, $3! = 6$ are interacting, so we expect that, on average, $2N_p/9 \equiv n_T$ plaquettes will be in interacting configurations at $\beta = 0$. As the temperature begins to decrease, lattice configurations with $n_c < n_T$ will become suppressed, while configurations with $n_c > n_T$ will become favored. We may demonstrate this trend by factoring out the Boltzmann weight of the totally random, thermal case from the partition function:

$$\mathcal{Q} = e^{\beta J n_T} \sum_{n_c=0}^{N_p} g(n_c)\ e^{\beta J(n_c - n_T)}. \tag{6.17}$$

While thermodynamics favors an increase in the number of interacting plaquettes, for small β, this influence is outweighed by the weight function $g(n_c)$, so that it is insufficient to consider small fluctuations around

n_T. Instead, the most basic approximation is to consider each plaquette to be independent of all others—an "ideal gas" of plaquettes—and compute the partition function

$$\mathcal{Q} \approx \mathcal{Q}_p^{N_p}, \tag{6.18}$$

where $\mathcal{Q}_p$ corresponds to a single plaquette. Of course, since plaquettes share vertices with their neighbors, this approximation neglects the correlations imposed by the lattice on neighboring sites. Considering the 6 interacting and the 21 noninteracting plaquette configurations, the single-plaquette partition function is

$$\mathcal{Q}_p = 21 + 6e^{\beta J}, \tag{6.19}$$

from which the high-temperature energy per lattice site may be estimated as

$$\left(\frac{E}{N}\right)_{\beta\to 0} \approx -\frac{4J}{2+7e^{-\beta J}}. \tag{6.20}$$

While this approximation gives the correct value at $\beta = 0$ (and also at $\beta \to \infty$), we can obtain a better estimate by considering more than one plaquette. The motivation for doing so stems from the fact that when a single spin changes orientation, it has the potential to change the energy of the *six* plaquettes of which it is a member. The cluster of plaquettes including a single spin and its nearest neighbors forms a hexagon (Fig. 6.8), which we will now treat as the independent constituent of our "ideal gas."

The procedure before us remains the same—compute the hexagon's partition function, $\mathcal{Q}_{\text{hex}}$, and approximate the full partition function as $\mathcal{Q} \approx \mathcal{Q}_{\text{hex}}^N$—but the details are more complicated. Accounting for all possible orientations of each of the spins in the hexagon, we build the partition function according to the number of interacting plaquettes n_c in the hexagon:

$$\mathcal{Q}_{\text{hex}} = \sum_{n_c=0}^{6} g(n_c)\, e^{\beta J n_c}. \tag{6.21}$$

Using a simple computer script to enumerate the values of $g(n_c)$, we find

$$\mathcal{Q}_{\text{hex}} = 597 + 720e^{\beta J} + 558e^{2\beta J} + 180e^{3\beta J} + 126e^{4\beta J} + 6e^{6\beta J}. \tag{6.22}$$

If we immediately use this result to approximate the energy per lattice site, we will find that we have overestimated the magnitude by a factor of three. Each hexagon comprises six plaquettes, while each lattice

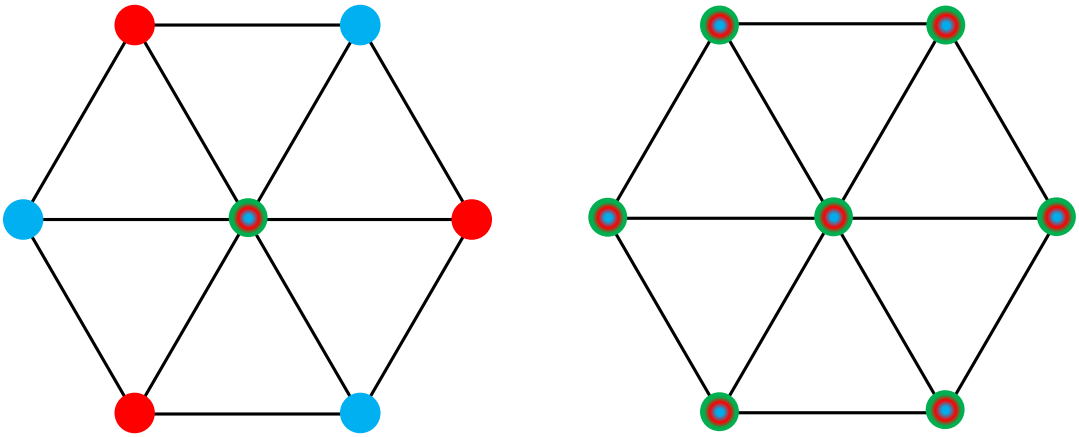

Figure 6.8: Hexagonal clusters that form the basis of the low-temperature (left) and high-temperature (right) approximations. At low temperature, only the central site is allowed to fluctuate, while the outer vertices remain in the ground-state configuration; at high temperature, all sites may fluctuate.

site corresponds to only two plaquettes. Thus, addressing this overcounting, we obtain the estimate

$$\left(\frac{E}{N}\right)_{\beta\to 0} \approx -4Je^{\beta J}\left(\frac{20+31e^{\beta J}+15e^{2\beta J}+14e^{3\beta J}+e^{5\beta J}}{199+240e^{\beta J}+186e^{2\beta J}+60e^{3\beta J}+42e^{4\beta J}+2e^{6\beta J}}\right). \tag{6.23}$$

Both high-temperature approximations to the energy are plotted alongside the numerical results in Fig. 6.6, showing reasonable agreement. The success of the hexagon approximation stems from the fact that at high temperatures, the correlation length is very small, and the formation of interacting domains is heavily disfavored combinatorically. As a result, individual sites are largely independent of their neighbors, so the assumptions of the approximation are met to an accuracy of roughly $1/N$ (the order of likelihood of two interacting plaquettes being neighbors). Once the temperature drops to the point where clusters begin to dominate, however, the approximation breaks down.

The low-temperature ($\beta \to \infty$) limit features many of the same considerations but ends up being considerably simpler to implement. As $\beta \to \infty$, the lattice will become fully saturated with interacting plaquettes. Any individidual spin flip will be suppressed by a factor $e^{-6\beta J}$, corresponding to the six plaquettes of the hexagon it will disrupt. Multiple simultaneous flips are suppressed by powers of this exponential, making them highly unlikely on thermal considerations alone. However, the combinatorial weights associated with such flips competes against the thermal suppression, and we expect that as the temperature rises, the com-

binatorics will lead to non-neglible deviations from the ground-state, perfect lattice. Thus, just as in the high-temperature case, we treat individual flips as if they were independent from one another and write $\mathcal{Q} \approx \mathcal{Q}_1^N$, where

$$\mathcal{Q}_1 = 2 + e^{6\beta J}, \tag{6.24}$$

corresponding to the one interacting and two noninteracting configurations of a single spin flipping in an otherwise perfect lattice. Given the hexagon picture we are using, the energy will again be overestimated by a factor of three; accounting for this,

$$\left(\frac{E}{N}\right)_{\beta\to\infty} \approx -\frac{2J}{1+2e^{-6\beta J}}, \tag{6.25}$$

where the approximation is seen to be exact in the limit. This low-temperature estimate of the energy is also plotted alongside the numerical results in Fig. 6.6, where the agreement is fair. One possible reason for the deficiency of this approximation is that at low temperatures, the energy cost of flipping two distant spins can be significantly larger than the cost of flipping two neighboring spins. Although neighboring flips are suppressed combinatorically, their relatively lower energy cost may mean that it is not sufficient to consider isolated, independent flips as this approximation does.

Section 6.6: Methods of detecting the phase transition

As already indicated, a divergence in the slope of the energy as a function of temperature is characteristic of a phase transition. Given that this derivative is related to the heat capacity at constant volume,

$$C_V = \left(\frac{\partial E}{\partial T}\right)_V, \tag{6.26}$$

we may use the energy fluctuations in the canonical ensemble to compute this derivative:

$$C_V = \beta^2 \left(\langle E^2\rangle - \langle E\rangle^2\right). \tag{6.27}$$

In Fig. 6.9, the *specific* heat capacity at constant volume clearly shows an increasingly sharp spike at the critical temperature. Though the maximum value of c_V is finite here, it diverges in the thermodynamic limit, corresponding to the latent heat: During the phase transition, the temperature remains constant as the change in energy brings about the transition.

In addition to the quantitative evidence of a phase transition furnished by the heat capacity, visually inspecting the lattice reveals qualitative differences between the two sides of the transition. In the Ising

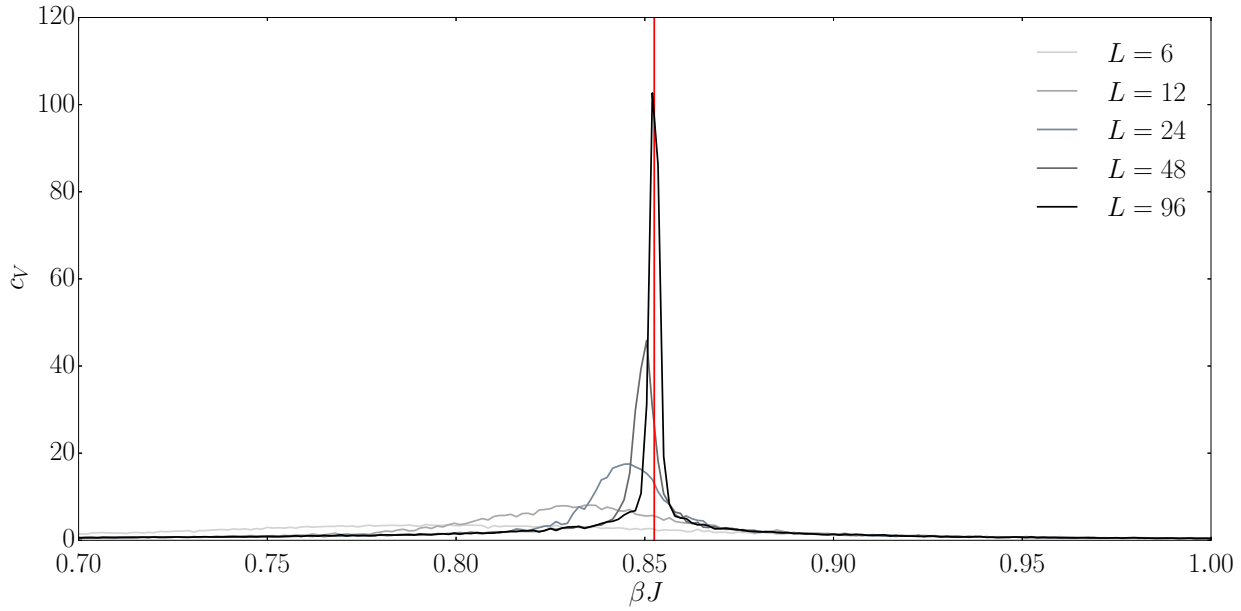

Figure 6.9: Specific heat capacity of the three-body lattice model, displaying a phase transition at the critical inverse temperature $\beta_c \simeq 0.853\ J^{-1}$ (red bar). Note the zoomed scale compared to Fig. 6.6.

model, the two values of ± 1 easily lend themselves to visualization—in Fig. 6.2, black and white compete until the decisive victory of black at the critical temperature. In the three-body model, however, visualizing the lattice is more nuanced.

To distinguish between the six possible phase orientations, we consider lattices corresponding to the six distinct ground states. Each ground state is maximally aligned, so that the orientation of any interacting plaquette in a sample must align with one, and only one, ground state. By comparing each plaquette against these six templates, a uniquely determined color may be assigned to each plaquette—*if* it is interacting. If no interaction takes place within a plaquette, it may be left uncolored. The result of this procedure is presented in Fig. 6.10, where the trend is analogous to that in the Ising model (Fig. 6.2). Starting from a random configuration at high temperatures, clusters form and grow as the temperature decreases. The six different phase orientations, which are incompatible with one another, compete until red abruptly dominates at the critical temperature.

Just as PCA reflected the discrete global Z_2 symmetry of the Ising model (Fig. 6.4), we anticipate that it will demonstrate the S_3 symmetry of the three-body model (see next section). Examining the results in Fig. 6.11, the appearance of a regular hexagon confirms this expectation. At high temperatures, the central cluster corresponds to the disordered, thermal configurations seen in the first grids of Fig. 6.10. As the temperature decreases, the sudden movement to six symmetrically distributed clusters (with few exceptions)

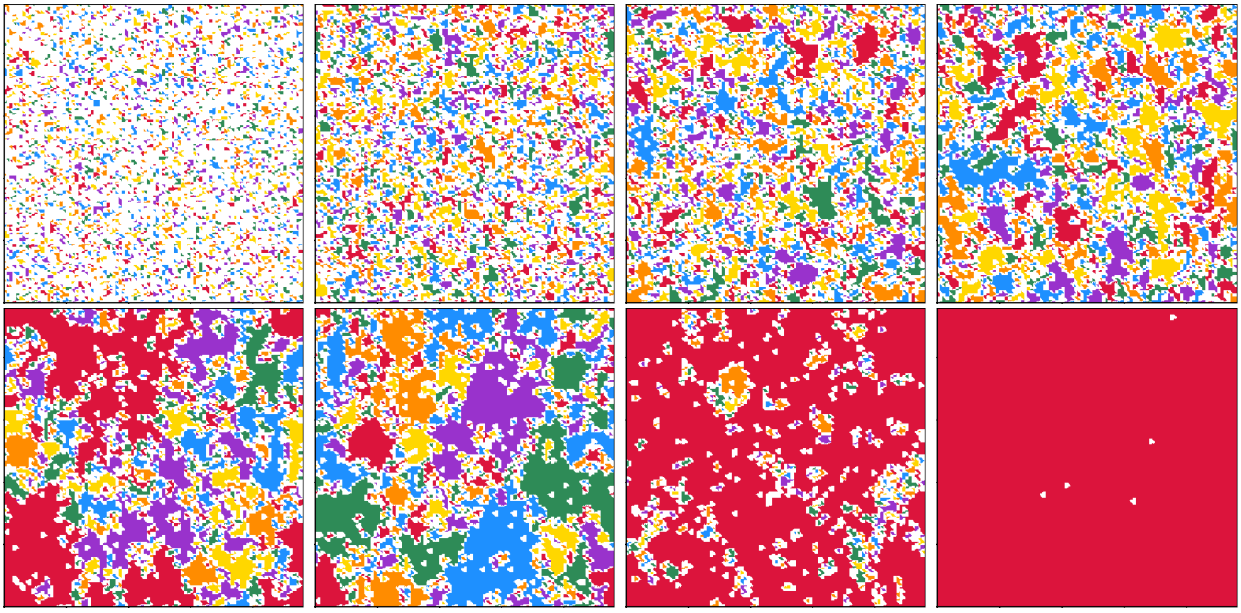

Figure 6.10: Linearized 96×96 triangular lattices colored by type of interacting plaquette (white indicates noninteracting). With decreasing temperatures, domains grow until reaching the critical (inverse) temperature $\beta_c \simeq 0.853\ J^{-1}$, at which point one domain (red) overwhelmingly dominates. In reading order from top left: $\beta J = 0$, $\beta J = 0.6$, $\beta J = 0.75$, $\beta J = 0.84$, $\beta J = 0.8475$, $\beta J = 0.8505$, $\beta J = 0.8535$, $\beta J = 1.5$.

reflects again the abrupt nature of the phase transition.

Finally, as the magnetization in the Ising model provided another indication of a phase transition, we may seek an analogue in the three-body model. In the Ising model, given the two opposing possible orientations of spins (up and down), magnetization may be quantified simply as the difference in the number of up and down spins. In the three-body model, on the other hand, the situation is again more complicated. Inspired by the hexagonal structure of Fig. 6.11, one possibility would be to assign to the different orientations the values of the coordinates of the hexagon in the complex plane (6^{th} roots of unity, $e^{in\pi/3}$). With this choice, though, the orientations are not treated on equal footing. Two orientations that differed by π radians would cancel exactly, but orientations that differed by some other angle would not.

Instead, we propose a geometric alternative: First, assign to each lattice a vector $\mathbf{n}$ in the non-negative orthant of $\mathbb{R}^6$ whose entries are the number of plaquettes in each of the six orientations. With this construction, a maximally ordered lattice would have a vector parallel to one of the six unit vectors $\mathbf{e}_i$, $1 \leq i \leq 6$, while a maximally disordered lattice would have a vector parallel to the vector $\mathbf{r} = (1, 1, 1, 1, 1, 1)$. The polar angle of $\mathbf{n}$ from $\mathbf{r}$, which is always positive, would then quantify the degree to which one phase dominates over the others,[6] in analogy with the absolute value of the magnetization in the Ising model. To normalize

[6]While we anticipate that the azimuthal angle about $\mathbf{r}$ would indicate *which* phase orientation is preferred, we do not perform

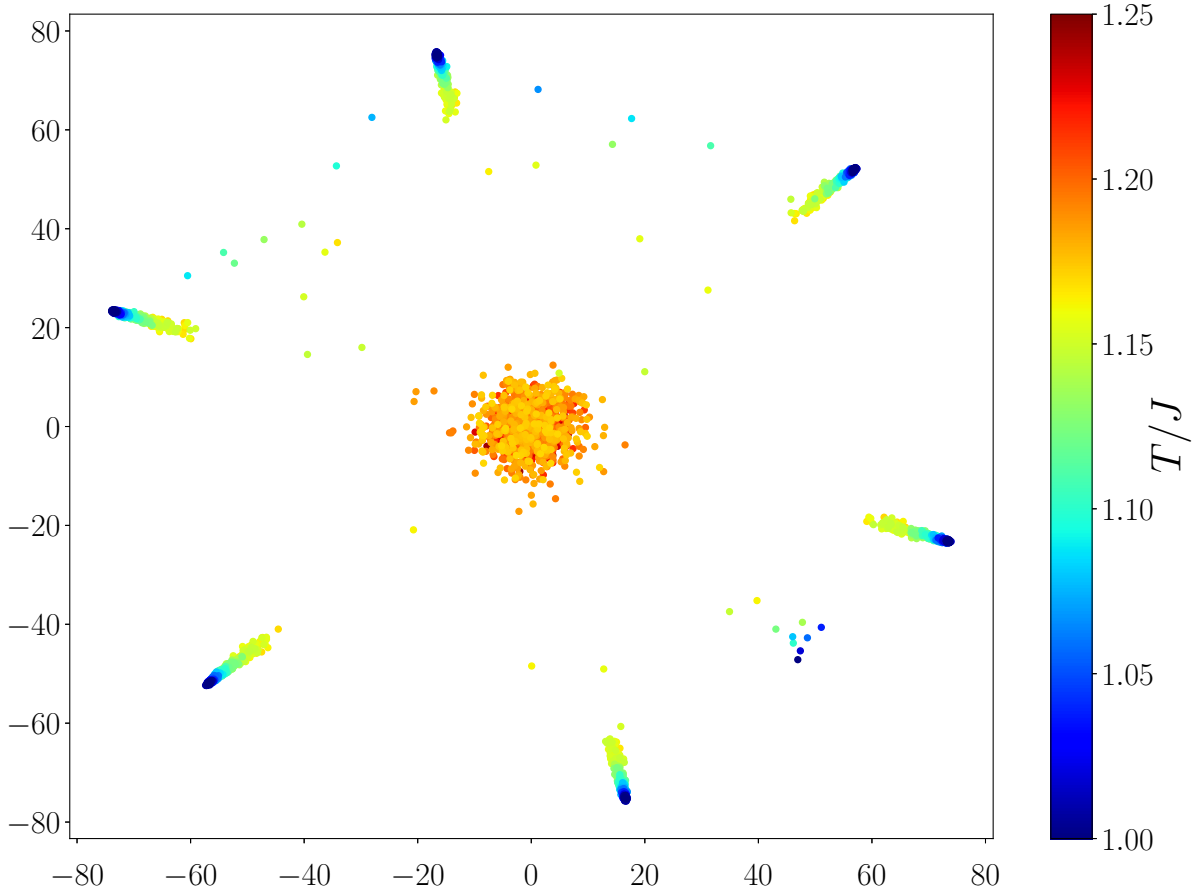

Figure 6.11: Scatter of projection onto the two most dominant PCA eigenvectors for 500 samples of 96×96 triangular lattices around the critical temperature. The six vertices, forming a regular hexagon, correspond to the six equivalent ground-state configurations, reflecting the S_3 symmetry.

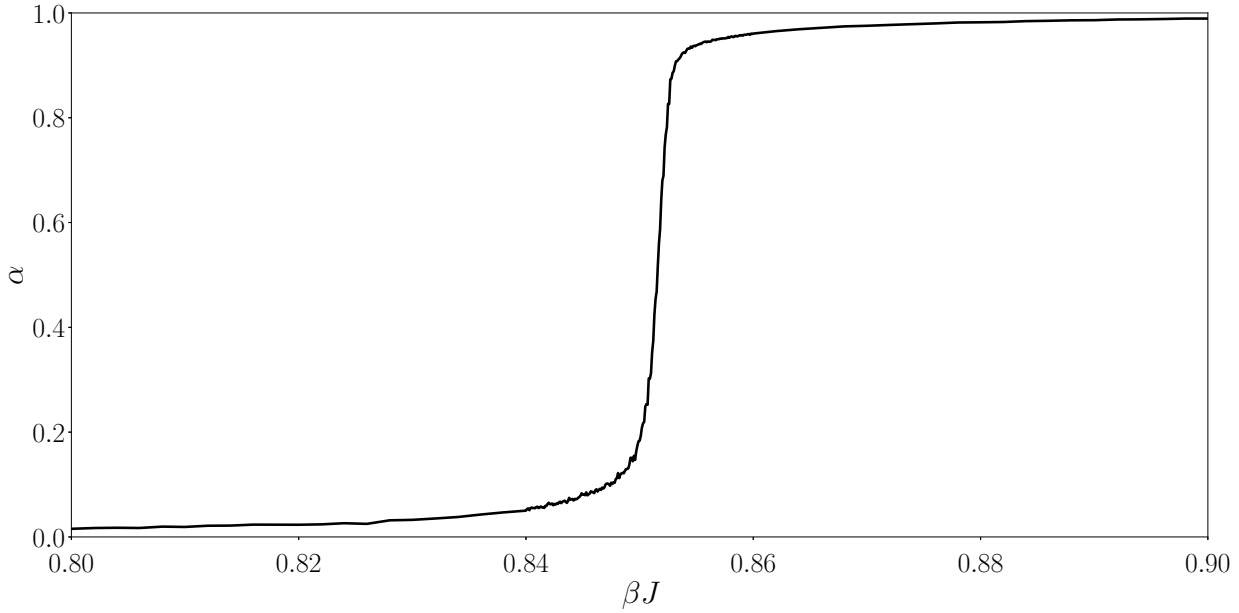

Figure 6.12: Degree of preference for one phase orientation over the others in the three-body lattice model, showing a sudden transition from disorder to order at the critical temperature.

all results for comparison, and to assign 0 to disorder and 1 to order, we define

$$\alpha = \frac{1 - \hat{\mathbf{n}} \cdot \hat{\mathbf{r}}}{1 - \mathbf{e}_i \cdot \hat{\mathbf{r}}}, \tag{6.28}$$

where $\mathbf{e}_i \cdot \hat{\mathbf{r}} = 1/\sqrt{6}$ for all i. In Fig. 6.12, α is plotted around the critical temperature, showing a remarkable similarity to the Ising magnetization of Fig. 6.1.

Section 6.7: S_3 symmetry and its reduction to Z_2

The Hamiltonian (6.10) is unaffected by any permutation of s_i, s_j, and s_k. To see this more directly, it is helpful to express (6.10) in terms of the Levi-Civita tensor as

$$H = -J \sum_{\langle ijk \rangle} \left(\epsilon_{s_i s_j s_k}\right)^2. \tag{6.29}$$

Cyclic permutations of the three-index Levi-Civita tensor leave it invariant, while the square prevents the change of sign that would occur from any other permutation. The symmetry group that captures such behavior—permutations on three objects—is the symmetric group S_3. As the order of any symmetric group

such an analysis in this work.

S_n is $n!$, S_3 has six elements, corresponding to the six colors seen in Fig. 6.10.

In this system, S_3 is a *global* symmetry: The whole lattice may be relabeled without a change in energy, but within one lattice configuration, there are still six possible, incompatible orientations of interacting plaquettes. Relabeling only a portion of the lattice would leave the energy invariant within the affected domain, but its boundary energy would likely change under such an action. At first glance, each of the six colors in Fig. 6.10—representing the possible orientations—corresponds to a unique ground state, neatly accounting for each of the elements of S_3.

However, the presence of periodic boundary conditions means that there are *not* six unique ground states. In fact, since the location of the boundary is arbitrary, there are only *two* unique ground states. The three "even" orientations are identified (as are the "odd" ones); in group theory terms, these sets of orientations form two cosets—one for even permutations, one for odd—and we have the quotient group[7]

$$S_3/Z_3 \cong Z_2, \tag{6.30}$$

where Z_n is the cyclic group of order n. Interestingly, despite the differences between this model and the Ising model, we see that their ground states share the same symmetry group.

Though the reduction from S_3 to Z_2 is readily apparent in the ground state, the symmetry actually breaks as soon as the phase transition occurs. Examining the density of the six different phases, all display equal representation at high temperatures (Fig. 6.13). At the critical temperature, however, three different categories emerge. "Major" denotes the dominant phase, as represented by the predominance of red in Fig. 6.10. "Minor" indicates the two other phases in the same Z_2 coset as major, so that major and minor comprise either all of the even permutations or all of the odd permutations. "Submajor" then corresponds to the remaining coset.

There is thus an asymmetric effect on the density of phases according to whether or not they belong to the same permutation sign as the dominant phase, so that even at finite temperatures, phases are distinguished according to the quotient group of Eq. (6.30). In terms of permutation signs of phases, Z_3 cyclic permutations do not generate a distinct lattice configuration. Parity inversions of Z_2 *do* invert the lattice configuration, but they also leave the energy invariant.

To highlight the symmetry breaking, we may repeat the PCA procedure on the lattice data, this time accounting for the periodic boundary conditions. As the numerical array holding the lattice values (which is fed into PCA) must have a boundary *somewhere*, values on the boundary of the array may differ even

[7]In general, $S_n/A_n \cong Z_2$, where A_n is the alternating group [140]; as there is only one group of order three, $Z_3 \cong A_3$.

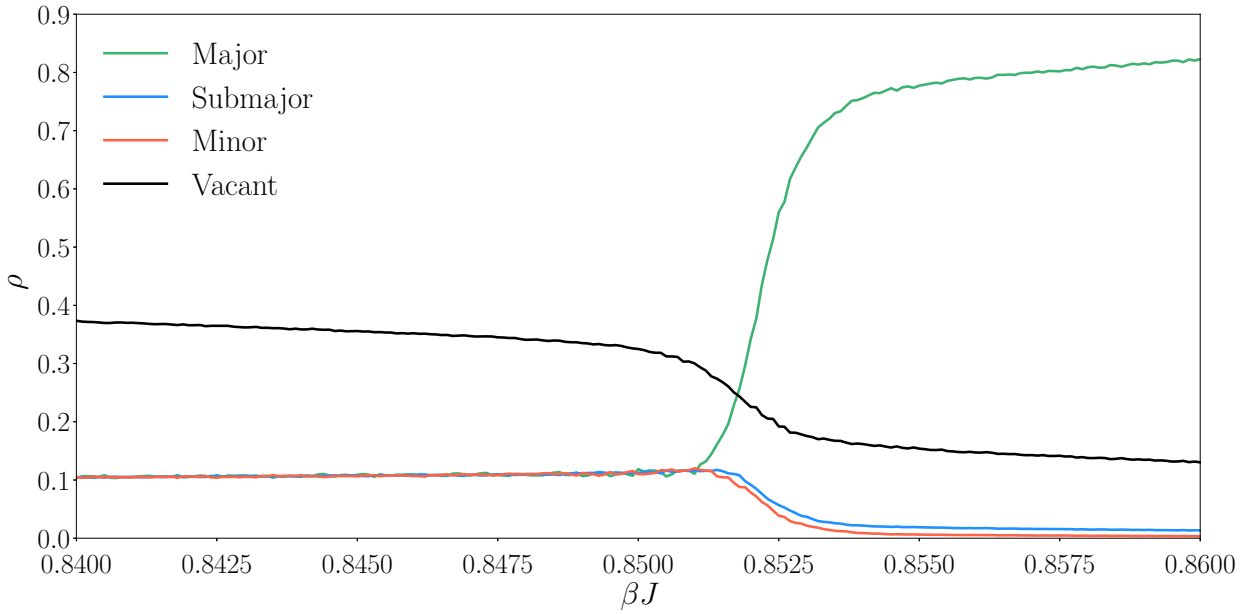

Figure 6.13: Density by area of plaquette phases in the triangular lattice model, showing an abrupt transition at the critical temperature. At this transition, three categories of interacting phases become distinct. "Vacant" denotes noninteracting plaquettes.

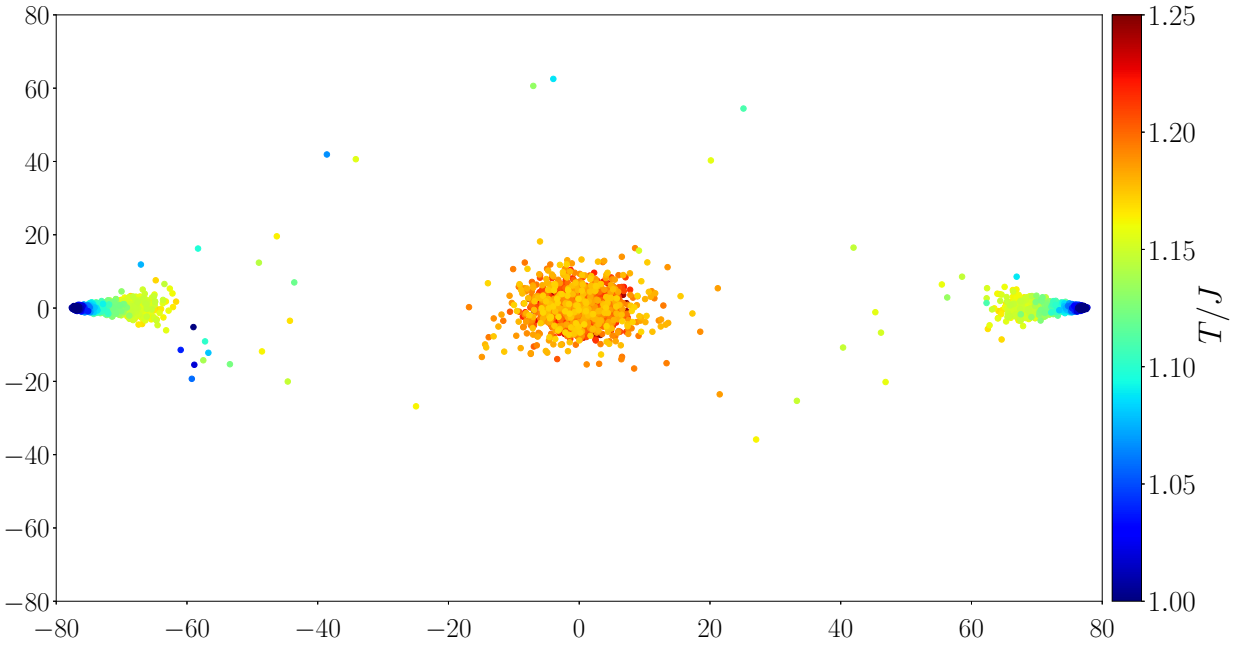

Figure 6.14: The same PCA scatter as in Fig. 6.11 after transforming the data to "inform" the PCA of the periodic boundary conditions. Note the similarity to Fig. 6.4, indicating a reduction of symmetry from S_3 to Z_2.

when they correspond to the same physical configuration. To remove this artificial distinction imposed by the data structure, we may shift the location of boundaries so that there are only two distinct dominant phases at low temperatures among all samples—one for even permutations, and one for odd. After this transformation, PCA reveals that there are indeed only two distinct configurations at temperatures below the phase transition. The two opposing[8] clusters in Fig. 6.14 now appear nearly identical to those of the Ising model, in accordance with their shared Z_2 symmetry.

Section 6.8: Summary

In this chapter, we formulated a lattice theory for three-body interactions. Curiously, as in the 1D three-body model, the three-body interaction in this lattice model has the effect of increasing the effective dimension by one. Transfer matrix and cluster update attempts presented insurmountable challenges, but we proceeded successfully with a local-update Monte Carlo solution. Basing our analysis on that of the Ising model, we found strong evidence for a second-order phase transition by multiple independent methods. This phase transition was associated with a reduction of discrete global symmetry from S_3 to Z_2. In a future work, we plan to address the critical exponents and universality class of this model.

[8] In Fig. 6.11, the hexagon is better viewed as two overlaid equilateral triangles in a "Star of David" configuration. The two triangles represent the even and odd elements of Z_2. To achieve the linear alignment seen in Fig. 6.14, one must take care to transform the data so that the two parity representations correspond to diametrically opposed vertices of the two triangles in the Star of David, as opposed to vertices at acute angles to each other.

CHAPTER 7: CONCLUSION AND OUTLOOK

In this Thesis, we have introduced and investigated two systems: a three-component Fermi gas in 1D with an attractive, zero-range three-body interaction; and a 2D triangular lattice model with an attractive, nearest-neighbor three-body interaction. Here, we briefly summarize each topic and discuss future prospects for each.

Section 7.1: Three-component 1D Fermi gas

In Chapters 2–5, we examined the three-component 1D Fermi gas in stages, successively adding more particles and adapting our approach as necessary. Starting with the simplest case of three particles (which is identical to the bosonic case), we carried out an exact solution and related the center-of-mass problem to the two-component, two-body Fermi system in 2D with an attractive, zero-range two-body interaction. This correspondence enabled us to find the first non-trivial virial coefficient b_3 for the three-component 1D problem, which provided a first approximation for thermodynamic quantities at low fugacity. Though we identified a Hubbard-Stratonovich transformation for the three-body force, we found that it suffered a complex phase problem and was thus unsuitable for straightforward Monte Carlo simulation.

Next, we studied the addition of a few more particles, where we developed a numerical method for solving the Schrödinger equation. While the method could, in principle, be applied to any number of particles, we found the numerical cost to be prohibitive beyond six particles. Limiting ourselves to the few-body problems of four to six particles, we applied this method to obtain results for the ground-state energy over a wide range of coupling strengths. To validate our approach, we used perturbation theory to provide analytical comparisons in the limits of weak and strong coupling and found the agreement to be excellent in both cases. As our numerical approach also gave access to the full wave function, we examined the spatial structure of the four-body problem, finding that the ground state consisted of a trimer plus an isolated spectator particle. Specifically considering the six-body case of two particles of each flavor, we found that instead of forming a bound hexamer state, the system prefers to assume the form of two separate trimers. Along with the strong-coupling energies of the other systems, these results suggested that trimer formation is the norm across varying particle numbers. As a final application of this method, we reintroduced two-body forces to the three-body problem, demonstrating the dissociation of the trimer for sufficiently repulsive two-body

interactions.

Before moving on to the many-body problem, we considered the presence of a harmonic trapping potential. The three-body problem again yielded to an exact solution, enabling us to find the trapped virial coefficient b_3 in terms of the corresponding 2D problem with two-body forces. Using previously known results, we additionally found a closed-form expression for b_3 in the limit of weak interactions (relative to the trapping frequency). Because the one-body eigenstates of the noninteracting trapped problem—which we used as a basis—are not simultaneously momentum eigenstates, we were unable to successfully apply the numerical method used in the un-trapped problem for the few-body case.

To analyze the many-body problem, it was necessary to abandon the wave function approach and instead turn to second quantization. Representing the grand canonical partition function in terms of worldlines, we employed the worm algorithm of quantum Monte Carlo to generate lattice configurations at finite temperature. With this approach, we presented results for various thermodynamic quantities and found good agreement with our earlier result for the virial expansion at low fugacity. In relation to the few-body predictions of trimer formation, we found that in the limit of strong coupling, the three-component Fermi system with attractive interactions approaches an ideal Fermi gas of trimers, constituting a Fermi-Fermi crossover (to be contrasted with the BCS-BEC crossover observed in two-component Fermi systems). We also obtained Tan's contact in the many-body problem, quantifying the breaking of scale invariance that motivated the study of this system.

Experimentally, the particular combination of parameters studied in this work has not yet been realized. Still, each of the constituent pieces has either been realized or proposed theoretically in either bosons or fermions. Many experimental groups have demonstrated the possibility of three-component Fermi gases through the use of multiple hyperfine states. In both bosons and fermions, effective three-body interactions have been achieved in the lab, while a mechanism for the suppression of two-body forces has been proposed theoretically for bosons. We hope that progress in this direction will eventually enable the same suppression to be realized for fermions, where our work will provide a first set of predictions.

While we strictly studied the balanced case of equal numbers of fermions of each species in the many-body problem, our application of the worm algorithm can readily be adapted to include polarization, as well as mass imbalance and the addition of an external potential without any sign problem. Thus, while the harmonic trapping potential caused difficulties in the few-body problem, it presents no such issue in the many-body case. The algorithm also easily allows us to increase the number of fermionic components and to include two-, four-, and higher-body interactions (both attractive and repulsive)—as long as we remain in 1D. In higher dimensions, the sign problem becomes an issue. Still, these possibilities provide a wealth of options for future research in 1D.

Section 7.2: Triangular lattice model

Motivated by the three-component Fermi gas, we constructed a classical model for attractive three-body interactions on a 2D triangular lattice. Using the Ising model as an illustrative comparison, we found qualitative evidence for a phase transition through the abrupt collapse to one of six possible phases. We then confirmed the existence of a phase transition quantitatively by computing the energy and heat capacity, both of which showed clearly the characteristics associated with second-order phase transitions. By extrapolating the heat capacity results to the large-volume limit (to be detailed in future work), we found a critical temperature of $T_c/J = 1.173093(32)$.

In addition to the typical measures of energy and heat capacity, we constructed a measure of net polarization in the system using the "cosine distance" and used principal component analysis to provide further qualitative insight into the model. By comparison to the Z_2 symmetry displayed by the Ising model under PCA, we illustrated the S_3 symmetry that exists in the three-body model. After noting a disparity among remnants of phases after the phase transition, we identified a collapse of the S_3 symmetry to Z_2, whereby two sets of three phases were distinguished from one another.

As hinted at previously, the study of this model is ongoing. The most immediately pressing task is the determination of the critical exponents of this system. Initial estimates are promising, but such analysis is too premature for quantitative results to be presented. Other questions of interest include block renormalization and the identification of a physical system to which this model might be applied. We anticipate further progress and publication of results in the near future.

APPENDIX A: THREE-BODY WAVE FUNCTION SOLUTION

The starting point is Eq. (2.3),

$$\left[-\frac{1}{2\bar{m}}\nabla_q^2 + \tilde{g}\delta(q_1)\delta(q_2)\right]\phi(q_1,q_2) = E_r\phi(q_1,q_2). \tag{A.1}$$

With the Fourier representation

$$\phi(\mathbf{q}) = \int \frac{d^2k}{(2\pi)^2}\; e^{-i\mathbf{k}\cdot\mathbf{q}}\tilde{\phi}(\mathbf{k}) \tag{A.2}$$

inserted into the above,

$$-\frac{1}{2\bar{m}}\int \frac{d^2k}{(2\pi)^2}\; -k^2 e^{-i\mathbf{k}\cdot\mathbf{q}}\tilde{\phi}(\mathbf{k}) + \tilde{g}\delta(\mathbf{q})\int \frac{d^2k}{(2\pi)^2}\; e^{-i\mathbf{k}\cdot\mathbf{q}}\tilde{\phi}(\mathbf{k}) = E_r\int \frac{d^2k}{(2\pi)^2}\; e^{-i\mathbf{k}\cdot\mathbf{q}}\tilde{\phi}(\mathbf{k}). \tag{A.3}$$

Transforming now to p-space,

$$\frac{1}{2\bar{m}}\int \frac{d^2k}{(2\pi)^2}\; k^2\tilde{\phi}(\mathbf{k})\int d^2q\; e^{i\mathbf{q}\cdot(\mathbf{p}-\mathbf{k})} + \tilde{g}\int \frac{d^2k}{(2\pi)^2}\; \tilde{\phi}(\mathbf{k})\int d^2q\; \delta(\mathbf{q})e^{i\mathbf{q}\cdot(\mathbf{p}-\mathbf{k})}$$
$$= E_r\int \frac{d^2k}{(2\pi)^2}\; \tilde{\phi}(\mathbf{k})\int d^2q\; e^{i\mathbf{q}\cdot(\mathbf{p}-\mathbf{k})}, \tag{A.4}$$

or, replacing the q integrals with δ-functions,

$$\frac{1}{2\bar{m}}\int d^2k\; k^2\tilde{\phi}(\mathbf{k})\;\delta(\mathbf{p}-\mathbf{k}) + \tilde{g}\int \frac{d^2k}{(2\pi)^2}\;\tilde{\phi}(\mathbf{k}) = E_r\int d^2k\;\tilde{\phi}(\mathbf{k})\;\delta(\mathbf{p}-\mathbf{k}), \tag{A.5}$$

leading finally to

$$\frac{p^2}{2\bar{m}}\tilde{\phi}(\mathbf{p}) + \frac{\tilde{g}}{(2\pi)^2}\int d^2k\;\tilde{\phi}(\mathbf{k}) = E_r\tilde{\phi}(\mathbf{p}). \tag{A.6}$$

Recognizing that the integral term is a constant, neglecting normalization, defining $\epsilon_B \equiv -E_r$, and inserting $\bar{m} = 1/2$, the solution is

$$\tilde{\phi}(\mathbf{p}) = -\frac{\tilde{g}}{(2\pi)^2}\frac{1}{p^2+\epsilon_B}\int d^2k\;\tilde{\phi}(\mathbf{k}). \tag{A.7}$$

While (A.7) appears to be implicit and not yet solved, the integral term is a constant, and the functional form of $\tilde{\phi}$ is fully determined. The implicit aspect leads to a relationship between $\tilde{g}$ and the normalization.

APPENDIX B: JUSTIFICATION FOR THE EQUALITY OF 1D THREE-BODY AND 2D TWO-BODY PARTITION FUNCTIONS

The primary concerns that arise in considering the equality of the 1D three-body and 2D two-body partition functions stem from the choice of coordinates. More precisely, we must verify that the results obtained are independent of our particular choice of coordinates.

For the c.m. coordinate, we have no freedom to choose a different *direction* for the basis vector. However, mathematically speaking, we are free to choose an arbitrary *magnitude* for the basis vector. Let us first demonstrate that whatever magnitude we choose has no effect on the c.m. partition function.

Taking the 3-body 1D problem as an example, the "canonical" c.m. coordinate is $\left(\frac{x}{3}, \frac{y}{3}, \frac{z}{3}\right)$. Instead of this, we will assign an arbitrary coefficient a and write the c.m. coordinate as (ax, ay, az). Given that the Laplacian before any coordinate change is given by

$$\nabla^2 = \frac{\partial^2}{\partial x^2} + \frac{\partial^2}{\partial y^2} + \frac{\partial^2}{\partial z^2}, \tag{B.1}$$

we wish to determine the coefficient on the $\frac{\partial^2}{\partial Q^2}$ term, which will determine the mass M of the c.m. coordinate. By standard partial derivative rules,

$$\frac{\partial}{\partial x} = \frac{\partial q_1}{\partial x}\frac{\partial}{\partial q_1} + \frac{\partial q_2}{\partial x}\frac{\partial}{\partial q_2} + \frac{\partial Q}{\partial x}\frac{\partial}{\partial Q}, \tag{B.2}$$

and similarly for y and z. As we are currently only interested in the Q derivatives, we may neglect the q_1 and q_2 terms—since these coordinates are orthogonal, there will be no cross terms. The result we are after, then, is

$$\nabla_Q^2 = \left[\left(\frac{\partial Q}{\partial x}\right)^2 + \left(\frac{\partial Q}{\partial y}\right)^2 + \left(\frac{\partial Q}{\partial z}\right)^2\right]\frac{\partial^2}{\partial Q^2} = 3a^2\frac{\partial^2}{\partial Q^2}, \tag{B.3}$$

revealing that the c.m. mass $M = 1/3a^2$. In the typical case where $a = 1/3$, we recover the expected $M = 3$. Now, let us see how this result applies to the partition function.

The c.m. partition function is given by

$$\mathcal{Q}_{1,1,1}^{\text{c.m.}} = \text{Tr}\left[e^{-\beta\hat{P}^2/2M},\right] \tag{B.4}$$

where $\hat{P}$ denotes the c.m. momentum operator. If we evaluate the trace by immediately integrating the exponential between $\langle P| \cdot |P\rangle$, we will obtain a divergent factor $\delta(0)$. To avoid this, we insert a resolution of the identity in position space as follows:

$$\int dP \int dQ \;\; \langle P|Q\rangle \langle Q|e^{-\beta\hat{P}^2/2M}|P\rangle = \frac{1}{2\pi}\int dQ \int dP \; e^{-\beta P^2/2M}, \tag{B.5}$$

where we have applied $\langle Q|P\rangle = \frac{1}{\sqrt{2\pi}}\exp(iQP)$. Applying box normalization, where the original coordinates span $(-L/2, L/2)$, the integral over dQ gives a factor of $3aL$; the one over dP is a standard Gaussian integral. The final result is then

$$\mathcal{Q}^{\text{c.m.}}_{1,1,1} = \frac{3aL}{2\pi}\sqrt{\frac{2\pi M}{\beta}} = \sqrt{3}\frac{L}{\lambda_T} \tag{B.6}$$

where we have applied $M = 1/3a^2$ and introduced the thermal wavelength $\lambda_T = \sqrt{2\pi\beta}$. We thus see that L scales proportionally to a, while $\sqrt{M}$ scales inversely proportionally to a, such that the partition function is unaffected by a rescaling of the c.m. coordinate.

Having seen that the choice of coordinates does not change the partition function, we must now verify that all of the scales involved in the mapping between the 1D 3-body and 2D 2-body problems allow us to equate the partition functions of their relative Hamiltonians. While the Hamiltonian (2.3) is clearly 2D, there are subtleties not addressed in the main text. First, the coupling is modified as $g \to \tilde{g}$ by the change of basis in 1D, but not in 2D; the mass $\bar{m} = m/2$ in both cases. Since the relative coefficients of the kinetic and potential terms are different in 1D and 2D, it is not immediately clear that the Hamiltonians truly correspond to the same problem. Furthermore, the scales of length L in each problem behave differently under the changes of basis. In 2D, the relative coordinate ranges over $(-L/2, L/2)$ in both directions. In 1D, the relative coordinates q_1 and q_2 range over $(-L, L)$ and $(-2L/\sqrt{3}, 2L/\sqrt{3})$, respectively: The geometry is rectangular, not square! This difference in length scales applies even at short distances, making the use of the same momentum cutoff Λ (and thus ϵ_B) in both directions suspect—the momentum integral (2.7) is elliptical rather than radial. In particular, ratios of partition functions that involve factors of L, such as in Eq. (2.21), do not obviously cancel.

With some modification, we can demonstrate that the above concerns are only superficial. The original coordinates q_1 and q_2 were chosen for their orthogonality and the equality of masses in both directions; these considerations provided the connection to the 2D problem. However, yet another choice of coordinates satisfies these criteria while *also* maintaining equal length scales in both directions. By rotating the q_1, q_2 axes by 45° as

$$\begin{pmatrix}\tilde{q}_1\\ \tilde{q}_2\end{pmatrix} = \begin{pmatrix}\frac{1}{\sqrt{2}} & \frac{1}{\sqrt{2}}\\ \frac{1}{\sqrt{2}} & -\frac{1}{\sqrt{2}}\end{pmatrix}\begin{pmatrix}q_1\\ q_2\end{pmatrix}, \tag{B.7}$$

we obtain

$$\begin{pmatrix}\tilde{q}_1\\ \tilde{q}_2\\ Q\end{pmatrix} = \begin{pmatrix}-\frac{1}{\sqrt{2}}+\frac{1}{\sqrt{6}} & \frac{1}{\sqrt{2}}+\frac{1}{\sqrt{6}} & -\sqrt{\frac{2}{3}}\\ -\frac{1}{\sqrt{2}}-\frac{1}{\sqrt{6}} & \frac{1}{\sqrt{2}}-\frac{1}{\sqrt{6}} & \sqrt{\frac{2}{3}}\\ \frac{1}{3} & \frac{1}{3} & \frac{1}{3}\end{pmatrix}\begin{pmatrix}x\\ y\\ z\end{pmatrix}, \tag{B.8}$$

where the masses on $\tilde{q}_1$, $\tilde{q}_2$ equal those on q_1, q_2, and both coordinates span $\left(-\tilde{L}, \tilde{L}\right)$, where $\tilde{L} = \sqrt{2}\left(1 + 1/\sqrt{3}\right) L$.[1]

Now that the geometries (and masses) are the same in the relative problems in 1D and 2D, the question boils down to whether

$$\mathrm{Tr}\left[e^{-\beta \hat{H}^{\mathrm{rel}}_{1,1,1}}\right] = \mathrm{Tr}\left[e^{-\beta \hat{H}^{\mathrm{rel,2D}}_{1,1}}\right] \tag{B.9}$$

in the limits $L, \tilde{L} \to \infty$ with $\tilde{L}/L = \sqrt{2}(1 + 1/\sqrt{3})$ and $\tilde{g}/g = 2/\sqrt{3}$. Now, as seen in Eq. (2.8), the binding energy is completely insensitive to long-distance physics, so the discrepancy between L and $\tilde{L}$ is inconsequential. Further, as each system obeys its respective version of Eq. (2.8), the parameters g and Λ are completely characterized by and absorbed into the physical binding energy ϵ_B. Finally, once ϵ_B is established, the entire energy spectrum is determined, with no free parameters [141]. Consequently, as long as $\beta\epsilon_B$ takes the same value in the 1D 3-body and 2D 2-body problems, the equality of the partition functions is guaranteed, and Eq. (2.22) is unambiguously confirmed.

[1] This rotation does not change the value of $\tilde{g}$.

APPENDIX C: EVALUATION OF HUBBARD-STRATONOVICH INTEGRAL

In the transformation, we encounter the following integral:

$$\int_{-3\pi/2}^{3\pi/2} \frac{dx}{3\pi} \exp\left(ae^{i2x/3}\cos^2 x\right), \tag{C.1}$$

where we are concerned with the functional dependence on a. Our approach will be to expand the first exponential as a power series; express cos as the sum of complex exponentials before performing a binomial expansion; integrate term by term; and then evaluate the sum. Disregarding the factor of 3π, the integrand becomes

$$\sum_{n=0}^{\infty} \frac{a^n}{n!} e^{i2nx/3} \left(\frac{e^{ix}+e^{-ix}}{2}\right)^{2n} = \sum_{n=0}^{\infty} \frac{1}{n!} \left(\frac{a}{4}\right)^n e^{i2nx/3} e^{i2nx} \sum_{k=0}^{2n} \binom{2n}{k} e^{-i2kx}. \tag{C.2}$$

What we now need to integrate reduces to

$$\frac{1}{3\pi} \int_{-3\pi/2}^{3\pi/2} e^{i2x\left(\frac{4n}{3}-k\right)} = \delta_{k,\frac{4n}{3}}. \tag{C.3}$$

This Kronecker delta restricts n to multiples of 3, so we may relabel the sum as

$$\sum_{n=0}^{\infty} \frac{1}{n!} \left(\frac{a}{4}\right)^n \sum_{k=0}^{2n} \binom{2n}{k} \delta_{k,\frac{4n}{3}} \to \sum_{n=0}^{\infty} \frac{1}{(3n)!} \left(\frac{a}{4}\right)^{3n} \sum_{k=0}^{6n} \binom{6n}{k} \delta_{k,4n}. \tag{C.4}$$

Using the Kronecker delta to evaluate the sum over k, we have

$$\sum_{n=0}^{\infty} \frac{1}{(3n)!} \left(\frac{a}{4}\right)^{3n} \binom{6n}{4n} = \sum_{n=0}^{\infty} \left(\frac{a}{4}\right)^{3n} \frac{(6n)!}{(2n)!(3n)!(4n)!}. \tag{C.5}$$

Finally, using Mathematica to evaluate the infinite sum, the result is

$$\int_{-3\pi/2}^{3\pi/2} \frac{dx}{3\pi} \exp\left(ae^{i2x/3}\cos^2 x\right) = {}_2F_4\left(\frac{1}{6},\frac{5}{6};\frac{1}{4},\frac{1}{2},\frac{3}{4},1;\frac{1}{2}\left(\frac{3a}{8}\right)^3\right), \tag{C.6}$$

where ${}_2F_4$ is a hypergeometric function.

APPENDIX D: DERIVATION OF CONTINUOUS, FREE-SPACE INTEGRAL EQUATION FOR $2+1+1$ FERMIONS

As seen in Eq. (3.26), the equation we are concerned with for four fermions (two identical) is

$$f(p) = -\frac{g}{4\pi^2}\int dxdydz\ \left[\frac{f(p)-f(x)}{\frac{1}{2}\left(p^2+x^2+y^2+z^2\right)+\epsilon}\right]\delta(x+y+z+p), \tag{D.1}$$

where $\epsilon = -E_4$ is the dimensionless 4-body (assumed) bound-state energy (all dimensionful quantities are in terms of ϵ_B for the 3-body case). This can be rearranged to

$$f(p)\left[1+\frac{g}{4\pi^2}\int dxdydz\ \frac{\delta(x+y+z+p)}{\frac{1}{2}\left(p^2+x^2+y^2+z^2\right)+\epsilon}\right] = \frac{g}{4\pi^2}\int dxdydz\ \left[\frac{f(x)}{\frac{1}{2}\left(p^2+x^2+y^2+z^2\right)+\epsilon}\right]\delta(x+y+z+p), \tag{D.2}$$

where we are primarily concerned with the integral in square brackets on the left-hand side. Though this integral features a logarithmic divergence, we will not yet introduce a cutoff. To get started, then, we rewrite the integral as

$$I \equiv \int dxdydz\ \frac{\delta(x+y+z+p)}{\frac{1}{2}\left(p^2+x^2+y^2+z^2\right)+\epsilon} = \frac{1}{\pi}\int ds\ e^{isp}\int d^3\mathbf{r}\frac{e^{i\mathbf{s}\cdot\mathbf{r}}}{r^2+p^2+2\epsilon}, \tag{D.3}$$

where $\mathbf{r} = (x,y,z)$, $\mathbf{s} = (s,s,s)$, and we have written the δ-function in its integral form. The right-most integral leads to a Yukawa-type function:

$$\int d^3\mathbf{r}\frac{e^{i\mathbf{s}\cdot\mathbf{r}}}{r^2+p^2+2\epsilon} = (2\pi)^3\,\frac{e^{-|\mathbf{s}|\sqrt{p^2+2\epsilon}}}{4\pi|\mathbf{s}|} = \frac{2\pi^2}{\sqrt{3}}\frac{e^{-|s|\sqrt{3p^2+6\epsilon}}}{|s|}, \tag{D.4}$$

where the factors of $\sqrt{3}$ arise from the magnitude of the $\mathbf{s}$ vector. At this point, then, the integral looks like

$$I = \frac{2\pi}{\sqrt{3}}\int_{-\infty}^{\infty}\frac{ds}{|s|}\ e^{isp}e^{-|s|\sqrt{3p^2+6\epsilon}}. \tag{D.5}$$

To deal with the absolute values, we break up the integral as

$$\int_{-\infty}^{\infty}\frac{ds}{|s|}\ e^{isp}e^{-|s|\sqrt{3p^2+6\epsilon}} = \int_{-\infty}^{0}\frac{ds}{-s}\ e^{isp}e^{s\sqrt{3p^2+6\epsilon}} + \int_{0}^{\infty}\frac{ds}{s}\ e^{isp}e^{-s\sqrt{3p^2+6\epsilon}}, \tag{D.6}$$

which can then be rearranged to

$$\int_{-\infty}^{\infty}\frac{ds}{|s|}\ e^{isp}e^{-|s|\sqrt{3p^2+6\epsilon}} = 2\int_{0}^{\infty}\frac{ds}{s}\cos(sp)\,e^{-s\sqrt{3p^2+6\epsilon}}. \tag{D.7}$$

Here we see that the integral will diverge as $s \to 0^+$, so we will replace 0 with Λ^{-1} (s has dimensions of length). Now,

$$2\int \frac{ds}{s}\cos(sp)\, e^{-s\sqrt{3p^2+6\epsilon}} = \mathrm{Ei}\left[-s\left(\sqrt{3p^2+6\epsilon}+ip\right)\right] + \mathrm{Ei}\left[-s\left(\sqrt{3p^2+6\epsilon}-ip\right)\right], \tag{D.8}$$

where $\mathrm{Ei}(x)$ is the exponential integral. For the evaluation at the upper bound, we have the limit

$$\lim_{x\to\infty} \mathrm{Ei}\left[-x\left(a+ib\right)\right] + \mathrm{Ei}\left[-x\left(a-ib\right)\right] = -i\pi + i\pi = 0, \tag{D.9}$$

for $a, b > 0$. This leaves only the lower bound's contribution, so, collecting all prefactors,

$$I = -\frac{2\pi}{\sqrt{3}}\left(\mathrm{Ei}\left[-\Lambda^{-1}\left(\sqrt{3p^2+6\epsilon}+ip\right)\right] + \mathrm{Ei}\left[-\Lambda^{-1}\left(\sqrt{3p^2+6\epsilon}-ip\right)\right]\right) = \\ -\frac{4\pi}{\sqrt{3}}\mathrm{Re}\left(\mathrm{Ei}\left[-\Lambda^{-1}\left(\sqrt{3p^2+6\epsilon}+ip\right)\right]\right). \tag{D.10}$$

For small negative arguments,

$$\mathrm{Ei}(x) = \gamma - i\pi + \ln x + \mathcal{O}(x), \tag{D.11}$$

where γ is the Euler-Mascheroni constant, so

$$-\mathrm{Re}\left(\mathrm{Ei}\left[-\Lambda^{-1}\left(\sqrt{3p^2+6\epsilon}+ip\right)\right]\right) = -\gamma + \ln\Lambda - \ln\sqrt{4p^2+6\epsilon} + \mathcal{O}\left(\Lambda^{-1}\right), \tag{D.12}$$

where the complex phase drops out after taking the real part. Altogether, in the limit $\Lambda \to \infty$, we have

$$I = \frac{4\pi}{\sqrt{3}}\left(\ln\Lambda - \ln\sqrt{4p^2+6\epsilon} - \gamma\right). \tag{D.13}$$

Inserting this into the left-hand side of our original equation,

$$f(p)\left[1 + \frac{g}{\pi\sqrt{3}}\left(\ln\Lambda - \ln\sqrt{4p^2+6\epsilon} - \gamma\right)\right], \tag{D.14}$$

we may use the fact that

$$\ln\Lambda^2 = -\frac{2\pi\sqrt{3}}{g}, \tag{D.15}$$

where ϵ_B is the three-body binding energy, to finally write

$$f(p)\left[\ln\sqrt{4p^2+6\epsilon}+\gamma\right] = -\frac{\sqrt{3}}{4\pi}\int dxdydz\ \left[\frac{f(x)}{\frac{1}{2}\left(p^2+x^2+y^2+z^2\right)+\epsilon}\right]\delta(x+y+z+p), \tag{D.16}$$

where we have eliminated both g and Λ, leaving only the physical binding energy ϵ_B as a parameter.

Following the same approach, it is possible to reduce the right-hand side as well. Rewriting the integral as

$$2\int dx\ f(x)\int dydz\ \frac{\delta(x+y+z+p)}{p^2+x^2+y^2+z^2+2\epsilon} = \frac{1}{\pi}\int dxds\ f(x)e^{is(x+p)}\int dydz\ \frac{e^{is(y+z)}}{y^2+z^2+p^2+x^2+2\epsilon}, \quad \text{(D.17)}$$

where the last integral can be written as

$$\int d^2\mathbf{r}\frac{e^{i\mathbf{s}\cdot\mathbf{r}}}{r^2+p^2+x^2+2\epsilon} = 2\pi K_0\left(|s|\sqrt{2p^2+2x^2+4\epsilon}\right). \quad \text{(D.18)}$$

With this, the Fourier cosine transform of K_0 appears, such that the final result is

$$f(p)\left[\ln\sqrt{4p^2+6\epsilon}+\gamma\right] = -\frac{\sqrt{3}}{2}\int dx\ \frac{f(x)}{\sqrt{(x+p)^2+2p^2+2x^2+4\epsilon}}. \quad \text{(D.19)}$$

Completing the square in the square root,

$$f(p)\left[\ln\left(4p^2+6\epsilon\right)+2\gamma\right] = -\int dx\ \frac{f(x)}{\sqrt{\left(x+\frac{p}{3}\right)^2+\frac{2}{9}\left(4p^2+6\epsilon\right)}}, \quad \text{(D.20)}$$

where the denominator of the integrand is seen to be the square root of a Breit-Wigner (a.k.a. Lorentzian, Cauchy) distribution with a resonance at $x=-p/3$ and a width related to the noninteracting contribution. Since the bounds are infinite, we can shift the integration variable to obtain

$$f(p)\left[\ln\left(4p^2+6\epsilon\right)+2\gamma\right] = -\int dy\ \frac{f\left(y-\frac{p}{3}\right)}{\sqrt{y^2+\frac{2}{9}\left(4p^2+6\epsilon\right)}}. \quad \text{(D.21)}$$

APPENDIX E: TRAPPED THREE-BODY WAVE FUNCTION SOLUTION

We start from the separated relative equation of motion,

$$\left[-\frac{\nabla_q^2}{2m}+\frac{\tilde{g}}{m}\delta(\mathbf{q})+\frac{1}{2}m\omega^2 q^2\right]\phi(\mathbf{q})=E_r\phi(\mathbf{q}), \tag{E.1}$$

where $\mathbf{q}=(q_1,\ q_2)$ (the factor of $1/m$ in front of the delta function accounts for units). Assuming zero angular momentum, we work with only the radial parts of the equation and define the dimensionless radius as $\rho\equiv\sqrt{m\omega}q$. The Hamiltonian then takes the form

$$\hat{H}=-\frac{\omega}{2}\left(\frac{\partial^2}{\partial\rho^2}+\frac{1}{\rho}\frac{\partial}{\partial\rho}\right)+\tilde{g}\omega\frac{\delta(\rho)}{2\pi\rho}+\frac{\omega}{2}\rho^2 \tag{E.2}$$

In analogy to the plane-wave Fourier transform of free space, we introduce an oscillator-space transform based on the solutions of the noninteracting trap (assuming azimuthal symmetry, i.e. zero angular momentum):

$$f(\rho)=\sum_{n=0}^{\infty}\tilde{f}_n e^{-\rho^2/2}L_n(\rho^2), \tag{E.3}$$

where L_n is the n^{th} order Laguerre polynomial.

With the normalization condition $\int_0^\infty dx\ e^{-x}L_m(x)L_n(x)=\delta_{mn}$, the inverse transform is

$$\tilde{f}_n=\int_0^\infty d\rho^2\ e^{-\rho^2/2}f(\rho)L_n(\rho^2). \tag{E.4}$$

(A factor of 2π from the angular integration has been omitted since it appears equally on all terms.) Inserting this expansion for $\phi(\rho)$,

$$\begin{aligned}&\sum_{k=0}^{\infty}\tilde{\phi}_k e^{-\rho^2/2}\times\\ &\quad\omega\Big[-\frac{1}{2}\Big((\rho^2-2)L_k(\rho^2)+4(\rho^2-1)L_{k-1}^{(1)}(\rho^2)+4\rho^2L_{k-2}^{(2)}(\rho^2)\Big)+\frac{\tilde{g}}{2\pi\rho}\delta(\rho)L_k(\rho^2)+\frac{1}{2}\rho^2L_k(\rho^2)\Big]=\\ &\qquad\qquad E_r\sum_{k=0}^{\infty}\tilde{\phi}_k e^{-\rho^2/2}L_k(\rho^2),\end{aligned} \tag{E.5}$$

where the $L_k^{(i)}$ are the associated Laguerre polynomials.

Applying the operator $\int_0^\infty d\rho^2\ e^{-\rho^2/2}L_n(\rho^2)$, it is necessary to make use of the following identities to carry out the integrals:

$$\int_0^\infty dx\ xe^{-x}L_n(x)L_k(x) = (2n+1)\delta_{n,k} - n\delta_{n-1,k} - (n+1)\delta_{n+1,k}$$
$$\int_0^\infty dx\ xe^{-x}L_n(x)L_{k-1}^{(1)}(x) = (n+1)\delta_{n+1,k} - n\delta_{n,k}$$
$$\int_0^\infty dx\ e^{-x}L_n(x)L_{k-1}^{(1)}(x) = \begin{cases} 1, & \text{if } k-1 \geq n \\ 0, & \text{otherwise} \end{cases}$$
$$\int_0^\infty dx\ xe^{-x}L_n(x)L_{k-2}^{(2)}(x) = \begin{cases} 1, & \text{if } k-2 \geq n \\ -n, & \text{if } k = n+1 \\ 0, & \text{otherwise} \end{cases}$$

Then, careful application of these identities yields the equation of motion as

$$\omega(2n+1)\tilde{\phi}_n + \frac{\tilde{g}\omega}{\pi}\sum_{k=0}^{\infty}\tilde{\phi}_k = E_r\tilde{\phi}_n. \tag{E.6}$$

From here, the oscillator-space wavefunction can be immediately written as

$$\tilde{\phi}_n = \frac{\tilde{g}}{\pi}S\ \frac{1}{E_r/\omega - (2n+1)}, \tag{E.7}$$

where $S = \sum_{k=0}^{\infty}\tilde{\phi}_k$.

Given all of the above,

$$S = \frac{\tilde{g}}{\pi}S\sum_{n=0}^{\infty}\frac{1}{E/\omega - (2n+1)}, \tag{E.8}$$

showing that

$$\frac{1}{\tilde{g}} = \frac{1}{\pi}\sum_{n=0}^{\infty}\frac{1}{E/\omega - (2n+1)}. \tag{E.9}$$

APPENDIX F: ANALYTICAL EVALUATION OF INTEGRAL OF PRODUCT OF SIX HERMITE POLYNOMIALS

The first derivation in this chapter extends ideas in Ref. [142] to the 3D case, while the second relies on the generating function for Hermite polynomials.

Section F.1: Integral in question

From the 3-body contact interaction in a 1D harmonic trap, we encounter the following integral:

$$\int_{-\infty}^{\infty} \mathrm{d}x\ e^{-3x^2} H_{n'}(x) H_{m'}(x) H_{l'}(x) H_n(x) H_m(x) H_l(x). \tag{F.1}$$

Assuming that the Hermite polynomials are defined such that $e^{-x^2} H_i^2(x)$ is normalized to unity, we can rewrite the integral in terms of general orthonormal functions as

$$\int_{-\infty}^{\infty} \mathrm{d}x\ \phi_{n'}^*(x) \phi_{m'}^*(x) \phi_{l'}^*(x) \phi_n(x) \phi_m(x) \phi_l(x). \tag{F.2}$$

Now, before the δ-function interactions were integrated out, the integral appeared as

$$\int_{-\infty}^{\infty} \mathrm{d}x\ \mathrm{d}y\ \mathrm{d}z\ \phi_{n'}^*(x) \phi_{m'}^*(y) \phi_{l'}^*(z) \phi_n(x) \phi_m(y) \phi_l(z)\ \delta(x-y) \delta(y-z). \tag{F.3}$$

In this form, it is evident that a change of coordinates might prove useful. In particular, the normalized Jacobi coordinates,

$$\begin{pmatrix} r_1 \\ r_2 \\ R \end{pmatrix} = \begin{pmatrix} \frac{1}{\sqrt{2}} & -\frac{1}{\sqrt{2}} & 0 \\ \frac{1}{\sqrt{6}} & \frac{1}{\sqrt{6}} & -\sqrt{\frac{2}{3}} \\ \frac{1}{\sqrt{3}} & \frac{1}{\sqrt{3}} & \frac{1}{\sqrt{3}} \end{pmatrix} \begin{pmatrix} x \\ y \\ z \end{pmatrix}, \tag{F.4}$$

are most suitable for the δ-functions (the transformation must be unitary to ensure that the transformed raising and lowering operators satisfy canonical commutation relations). Note that under this transformation, the δ-functions acquire an overall factor of $1/\sqrt{3}$.

Section F.2: Wave functions as oscillator states

Going forward, we will work with the raising and lowering operators acting on states labelled by excitation number. Inverting the above transformation, the relative operators can be written in terms of the original

ones as

$$\begin{pmatrix} a_x \\ a_y \\ a_z \end{pmatrix} = \begin{pmatrix} \frac{1}{\sqrt{2}} & \frac{1}{\sqrt{6}} & \frac{1}{\sqrt{3}} \\ -\frac{1}{\sqrt{2}} & \frac{1}{\sqrt{6}} & \frac{1}{\sqrt{3}} \\ 0 & -\sqrt{\frac{2}{3}} & \frac{1}{\sqrt{3}} \end{pmatrix} \begin{pmatrix} a_1 \\ a_2 \\ a_R \end{pmatrix}. \tag{F.5}$$

With these operators, the state $\phi_n(x)\phi_m(y)\phi_l(z)$ can be represented by

$$|nml\rangle = \frac{1}{\sqrt{n!\ m!\ l!}} \left(a_x^\dagger\right)^n \left(a_y^\dagger\right)^m \left(a_z^\dagger\right)^l |0\rangle_x |0\rangle_y |0\rangle_z , \tag{F.6}$$

and since the ground state is unique in either coordinate system, this is also equal to

$$\frac{1}{\sqrt{n!m!l!}} \left(\frac{1}{\sqrt{2}}a_1^\dagger + \frac{1}{\sqrt{6}}a_2^\dagger + \frac{1}{\sqrt{3}}a_R^\dagger\right)^n \left(-\frac{1}{\sqrt{2}}a_1^\dagger + \frac{1}{\sqrt{6}}a_2^\dagger + \frac{1}{\sqrt{3}}a_R^\dagger\right)^m \left(-\sqrt{\frac{2}{3}}a_2^\dagger + \frac{1}{\sqrt{3}}a_R^\dagger\right)^l |0\rangle_1 |0\rangle_2 |0\rangle_R . \tag{F.7}$$

Applying the multinomial theorem to each exponentiated term, this state can be rewritten as

$$\sqrt{\frac{n!m!l!}{3^l}} \sum_{ijk} \sum_{\alpha\beta\gamma} \sum_{ab} \frac{(-1)^{\alpha+a}}{i!\ j!\ k!\ \alpha!\ \beta!\ \gamma!\ a!\ b!}\ 2^{(a-i-j-\alpha-\beta)/2}\ 3^{-(j+k+\beta+\gamma)/2}\ \delta_{i+j+k,n}\delta_{\alpha+\beta+\gamma,m}\delta_{a+b,l}\ \times$$
$$\sqrt{(i+\alpha)!(j+\beta+a)!(k+\gamma+b)!}\,|i+\alpha\rangle_1 |j+\beta+a\rangle_2 |k+\gamma+b\rangle_R . \tag{F.8}$$

The expression for $\langle n'm'l'|$ is analogous.

Section F.3: Reconstructing the integral

In terms of states, the integral can be written as

$$\int_{-\infty}^{\infty} \mathrm{d}x\ \mathrm{d}y\ \mathrm{d}z\ \ \langle n'm'l'|xyz\rangle \langle xyz|nml\rangle\ \ \delta(x-y)\delta(y-z) =$$
$$\int_{-\infty}^{\infty} \mathrm{d}r_1\ \mathrm{d}r_2\ \mathrm{d}R\ \ \langle n'm'l'|r_1r_2R\rangle \langle r_1r_2R|nml\rangle\ \ \frac{\delta(r_1)\delta(r_2)}{\sqrt{3}}. \tag{F.9}$$

Carrying out the integrals with δ-functions and reintroducing wave function notation, the above inner products evaluate to

$$\phi^*_{i'+\alpha'}(0)\phi_{i+\alpha}(0)\phi^*_{j'+\beta'+a'}(0)\phi_{j+\beta+a}(0)\phi^*_{k'+\gamma'+b'}(R)\phi_{k+\gamma+b}(R). \tag{F.10}$$

Noting that Hermite polynomials of odd order vanish at the origin, we learn from this that $i+\alpha$, $j+\beta+a$, and their primed analogs all must be even. Integrating over R, we further learn that $k+\gamma+b = k'+\gamma'+b'$ is another constraint.

If $H_n(x)$ is taken to have the same normalization as Mathematica's `HermiteH[n,x]`, then

$$\phi_n(x) = \frac{1}{\sqrt{n!\ 2^n\sqrt{\pi}}} e^{-x^2/2} H_n(x), \tag{F.11}$$

such that

$$\phi_n(0) = \frac{(-1)^{n/2}}{\sqrt{n!\ 2^n\sqrt{\pi}}} \frac{n!}{(n/2)!}. \tag{F.12}$$

From here, all of the pieces written previously can be combined into a single expression which is a summation over 16 indices subject to 11 constraints:

$$\begin{aligned}
&\int_{-\infty}^{\infty} \mathrm{d}x\ e^{-3x^2} H_{n'}(x) H_{m'}(x) H_{l'}(x) H_n(x) H_m(x) H_l(x) = \\
&\quad \frac{(-1)^{(n+m+l+n'+m'+l')/2}}{\pi 2^{n+m+n'+m'}} \sqrt{\frac{n!\ m!\ l!\ n'!\ m'!\ l'!}{3^{n+m+l+n'+m'+l'+1}}} \sum_{\substack{ijk \\ i'j'k'}} \sum_{\substack{\alpha\beta\gamma \\ \alpha'\beta'\gamma'}} \sum_{\substack{ab \\ a'b'}} (k+\gamma+b)!\ \delta_{k+\gamma+b,k'+\gamma'+b'} \times \\
&\qquad \delta_{a+b,l}\delta_{a'+b',l'} \frac{(-1)^{\alpha+\alpha'+a+a'+k+\gamma+b}}{i!\ j!\ k!\ i'!\ j'!\ k'!\ \alpha!\ \beta!\ \gamma!\ \alpha'!\ \beta'!\ \gamma'!\ a!\ b!\ a'!\ b'!}\ 2^{k+k'+\gamma+\gamma'}\ 3^{(i+i'+\alpha+\alpha')} \times \\
&\qquad \delta_{i+j+k,n}\delta_{i'+j'+k',n'}\delta_{\alpha+\beta+\gamma,m}\delta_{\alpha'+\beta'+\gamma',m'} \frac{(i+\alpha)!\ (j+\beta+a)!\ (i'+\alpha')!\ (j'+\beta'+a')!}{\left(\frac{i+\alpha}{2}\right)!\ \left(\frac{j+\beta+a}{2}\right)!\ \left(\frac{i'+\alpha'}{2}\right)!\ \left(\frac{j'+\beta'+a'}{2}\right)!},
\end{aligned} \tag{F.13}$$

where $i+\alpha$ and $j+\beta+a$ are even (as are their primed counterparts).

Section F.4: Solution by generating functions

The starting point for this derivation is the generating function for the (non-normalized) Hermite polynomials [68],

$$e^{2xt-t^2} = \sum_{m=0}^{\infty} H_m(x)\ \frac{t^m}{m!}. \tag{F.14}$$

From this relation, it is evident that

$$H_n(x) = \frac{d^n}{dt^n}\left(e^{2xt-t^2}\right)\Big|_{t=0}, \tag{F.15}$$

as all terms with $m < n$ do not survive the n^{th} derivative, and all terms with $m > n$ vanish at $t = 0$. A product of six Hermite polynomials may thus be represented by

$$H_n(x)H_m(x)H_l(x)H_{n'}(x)H_{m'}(x)H_{l'}(x) = \frac{\partial^n}{\partial t_1^n}\frac{\partial^m}{\partial t_2^m}\frac{\partial^l}{\partial t_3^l}\frac{\partial^{n'}}{\partial t_4^{n'}}\frac{\partial^{m'}}{\partial t_5^{m'}}\frac{\partial^{l'}}{\partial t_6^{l'}}\left[\prod_{i=1}^{6} e^{2xt_i - t_i^2}\right]_{t_1,\ldots,t_6=0}. \tag{F.16}$$

Since an integral over x commutes with all of the t-derivatives, we may first carry out

$$\int_{-\infty}^{\infty} dx\ e^{-3x^2+2xT_1-T_2} = \sqrt{\frac{\pi}{3}}\ e^{T_1^2/3-T_2}, \tag{F.17}$$

where $T_1 = \sum_{i=1}^{6} t_i$ and $T_2 = \sum_{i=1}^{6} t_i^2$. Incorporating the normalization, then, the final result may be expressed as

$$\int_{-\infty}^{\infty} \mathrm{d}x\ e^{-3x^2} H_{n'}(x)H_{m'}(x)H_{l'}(x)H_n(x)H_m(x)H_l(x) = \frac{1}{\pi\sqrt{3\cdot 2^{n+m+l+n'+m'+l'} n!\ m!\ l!\ n'!\ m'!\ l'!}}\frac{\partial^n}{\partial t_1^n}\frac{\partial^m}{\partial t_2^m}\frac{\partial^l}{\partial t_3^l}\frac{\partial^{n'}}{\partial t_4^{n'}}\frac{\partial^{m'}}{\partial t_5^{m'}}\frac{\partial^{l'}}{\partial t_6^{l'}}\left[e^{T_1^2/3-T_2}\right]_{t_1,\ldots,t_6=0}. \tag{F.18}$$

APPENDIX G: DYSON SERIES SOLUTION FOR THE IMAGINARY TIME EVOLUTION OPERATOR

Starting with the Schrödinger equation,

$$i\frac{\partial}{\partial t}\left|\alpha(t)\right\rangle = H\left|\alpha(t)\right\rangle, \tag{G.1}$$

we switch to imaginary time $\tau = it$ to obtain (the diffusion equation)

$$-\frac{\partial}{\partial \tau}\left|\alpha(\tau)\right\rangle = H\left|\alpha(\tau)\right\rangle. \tag{G.2}$$

The Hamiltonian is composed of $H = H_d + H_h$, which we relabel as $H_d \equiv H_0$ and $H_h \equiv V$ (H_h is to be treated as a perturbation on H_d).

Recasting the problem in the interaction picture,

$$\left|\alpha_I(\tau)\right\rangle = e^{\tau H_0}\left|\alpha(\tau)\right\rangle, \tag{G.3}$$

and

$$-\frac{\partial}{\partial \tau}\left|\alpha_I(\tau)\right\rangle = V_I(\tau)\left|\alpha_I(\tau)\right\rangle, \tag{G.4}$$

where

$$V_I(\tau) = e^{\tau H_0} V e^{-\tau H_0}. \tag{G.5}$$

Using the fact that

$$\left|\alpha_I(\beta)\right\rangle = \left|\alpha_I(0)\right\rangle + \int_0^\beta d\tau\ \frac{\partial}{\partial \tau}\left|\alpha_I(\tau)\right\rangle, \tag{G.6}$$

we arrive at the integral equation,

$$\left|\alpha_I(\beta)\right\rangle = \left|\alpha_I(0)\right\rangle - \int_0^\beta d\tau\ V_I(\tau)\left|\alpha_I(\tau)\right\rangle. \tag{G.7}$$

Substituting this equation into itself repeatedly generates a Dyson series solution,

$$\left|\alpha_I(\beta)\right\rangle = \left[\mathbb{1} - \int_0^\beta d\tau_1\ V_I(\tau_1) + \int_0^\beta d\tau_1 \int_0^{\tau_1} d\tau_2\ V_I(\tau_1)V_I(\tau_2) - \ldots\right]\left|\alpha_I(0)\right\rangle, \tag{G.8}$$

which may be rewritten as

$$\left|\alpha_I(\beta)\right\rangle = U_I(\beta)\left|\alpha_I(0)\right\rangle, \tag{G.9}$$

where we have identified the expression in square brackets as the imaginary time evolution operator in the

interaction picture. As we are interested in the Schrödinger picture solution, we may simply multiply from the left as follows to obtain the desired evolution operator:

$$|\alpha(\beta)\rangle = e^{-\beta H_0} |\alpha_I(\beta)\rangle = e^{-\beta H_0} U_I(\beta) |\alpha(0)\rangle = U(\beta) |\alpha(0)\rangle . \tag{G.10}$$

Note that $|\alpha_I(0)\rangle = |\alpha(0)\rangle$, so there is no exponential in H_0 to the right of $U(\beta)$.

Returning to the full Hamiltonian in the original problem, we have

$$|\alpha(\beta)\rangle = e^{-\beta H} |\alpha(0)\rangle , \tag{G.11}$$

so that we can identify

$$e^{-\beta H} = U(\beta). \tag{G.12}$$

To evaluate the partition function $\mathcal{Z} = \mathrm{Tr}\left(e^{-\beta H}\right)$, then, it is sufficient to evaluate the trace of $U(\beta)$. Expanding the V_I terms and replacing $H_0 = H_d$, $V = H_h$, we recognize the form of Eq. (11) from Ref. [121]:

$$\mathcal{Z} = \sum_{k=0}^{\infty} \int_0^{\beta} d\tau_k \int_0^{\tau_k} d\tau_{k-1} \ldots \int_0^{\tau_2} d\tau_1 \ \mathrm{Tr}\left[e^{-(\beta-\tau_k)H_d} H_h e^{-(\tau_k-\tau_{k-1})H_d} H_h \ldots H_h e^{-\tau_1 H_d} \right] . \tag{G.13}$$

APPENDIX H: THREE-COMPONENT MAGNETIC SUSCEPTIBILITIES AT VANISHING APPLIED FIELDS

As in the main text, we first seek a change of coordinates suitable for three components. With

$$\mathcal{Z} = \mathrm{Tr}\left[e^{-\beta(H-\mu_1 N_1-\mu_2 N_2-\mu_3 N_3)}\right] = \mathrm{Tr}\left[e^{-\beta\left(H-\vec{\mu}\cdot\vec{N}\right)}\right], \tag{H.1}$$

where $\vec{\mu} = (\mu_1, \mu_2, \mu_3)$ and $\vec{N} = (N_1, N_2, N_3)$, we insert $I = U^{-1}U$ as

$$\vec{\mu}^T\vec{N} = \vec{\mu}^T U^{-1} U\vec{N} = \vec{h}^T\vec{M}, \tag{H.2}$$

so that $\vec{M} = U\vec{N}$, $\vec{h} = \left(U^{-1}\right)^T\vec{\mu}$. Explicitly,

$$\begin{pmatrix} M_1 \\ M_2 \\ M_3 \end{pmatrix} = \begin{pmatrix} 1 & 1 & 1 \\ a & -a & 0 \\ b & b & -2b \end{pmatrix} \begin{pmatrix} N_1 \\ N_2 \\ N_3 \end{pmatrix}, \tag{H.3}$$

and

$$\begin{pmatrix} h_1 \\ h_2 \\ h_3 \end{pmatrix} = \begin{pmatrix} 1/3 & 1/2a & 1/6b \\ 1/3 & -1/2a & 1/6b \\ 1/3 & 0 & -1/3b \end{pmatrix} \begin{pmatrix} \mu_1 \\ \mu_2 \\ \mu_3 \end{pmatrix}. \tag{H.4}$$

The partition function can then be written as

$$\mathcal{Z} = \mathrm{Tr}\left[e^{-\beta\left(H-\vec{h}\cdot\vec{M}\right)}\right], \tag{H.5}$$

such that

$$\frac{1}{\mathcal{Z}}\frac{\partial\mathcal{Z}}{\partial h_i} = \beta\left\langle M_i\right\rangle \tag{H.6}$$

and

$$\frac{1}{\mathcal{Z}}\frac{\partial^2\mathcal{Z}}{\partial h_i^2} = \beta^2\left\langle M_i^2\right\rangle. \tag{H.7}$$

Using Eq. (H.3), we see that $\langle M_1\rangle = \langle N\rangle$, where N is the total particle number over all flavors.

Moving to M_2, the first moment vanishes:

$$\langle M_2\rangle = a\left\langle N_1 - N_2\right\rangle = a\left[\langle N_1\rangle - \langle N_2\rangle\right] = 0, \tag{H.8}$$

because for $h_2 = 0$, implying no asymmetry between flavors, particle number expectation values are equal.

The second moment, however, does not vanish:

$$\left\langle M_2^2 \right\rangle = a^2 \left\langle (N_1 - N_2)^2 \right\rangle = a^2 \left[\left\langle N_1^2 \right\rangle + \left\langle N_2^2 \right\rangle - 2 \left\langle N_1 N_2 \right\rangle \right]. \tag{H.9}$$

Using again the symmetry implied by $h_2 = h_3 = 0$, we may freely interchange the flavor labels inside expectation values, so that

$$\left\langle M_2^2 \right\rangle = 2a^2 \left[\left\langle N_i^2 \right\rangle - \left\langle N_i N_j \right\rangle \right], \tag{H.10}$$

where i and j indicate any two distinct flavors.

Similarly, for h_3, the first moment vanishes, but the second does not:

$$\left\langle M_3 \right\rangle = b \left\langle N_1 + N_2 - 2N_3 \right\rangle = b \left[\left\langle N_1 \right\rangle + \left\langle N_2 \right\rangle - 2 \left\langle N_3 \right\rangle \right] = 0, \tag{H.11}$$

and

$$\left\langle M_3^2 \right\rangle = 6b^2 \left[\left\langle N_i^2 \right\rangle - \left\langle N_i N_j \right\rangle \right], \tag{H.12}$$

where we have relabeled flavors and collected like terms.

Turning to the susceptibilities χ_i, we have

$$\chi_i \equiv \frac{1}{\beta} \frac{\partial^2 \ln \mathcal{Z}}{\partial h_i^2} = \frac{1}{\beta} \left[\frac{1}{\mathcal{Z}} \frac{\partial^2 \mathcal{Z}}{\partial h_i^2} - \left(\frac{1}{\mathcal{Z}} \frac{\partial \mathcal{Z}}{\partial h_i} \right)^2 \right]. \tag{H.13}$$

Since we have already seen in Eqs. (H.6), (H.8), and (H.11) that the first moments vanish, when we assert $h_2 = h_3 = 0$, $h_1 = \mu$, the susceptibilities depend only on the second moments:

$$\chi_i = \beta \left\langle M_i^2 \right\rangle. \tag{H.14}$$

When we reintroduce the original particle numbers, the two susceptibilities differ only by an overall factor:

$$\chi_2 = 2a^2 \beta \left[\left\langle N_i^2 \right\rangle - \left\langle N_i N_j \right\rangle \right], \tag{H.15}$$

and

$$\chi_3 = 6b^2 \beta \left[\left\langle N_i^2 \right\rangle - \left\langle N_i N_j \right\rangle \right]. \tag{H.16}$$

Since the coordinate change applies whether or not an interaction is present, if these susceptibilities are written as a ratio with their noninteracting counterparts, then the dependence on a and b drops out, and we

will obtain

$$\frac{\chi_2}{\chi_2^0} = \frac{\chi_3}{\chi_3^0} = \frac{\left\langle N_i^2 \right\rangle - \langle N_i N_j \rangle}{\langle N_k^2 \rangle_0 - \langle N_k N_l \rangle_0}, \tag{H.17}$$

where $i \neq j$ and $k \neq l$.

As Eq. (H.17) relies on the noninteracting susceptibility, we will now derive an exact expression for χ_i^0. First, we note that different fermionic species are completely uncorrelated in the ideal (noninteracting) case, so that $\langle N_i N_j \rangle_0 = \langle N_i \rangle_0 \langle N_j \rangle_0$.[1] As detailed in standard texts [75], the grand canonical partition function for the ideal Fermi gas with energy states ϵ is given by

$$\mathcal{Z} = \prod_\epsilon \left(1 + z e^{-\beta\epsilon}\right), \tag{H.18}$$

where $z = e^{\beta\mu}$ is the fugacity. In parallel with Eqs. (H.6) and (H.7),

$$\frac{1}{\mathcal{Z}} \frac{\partial \mathcal{Z}}{\partial (\beta\mu_i)} = \langle N_i \rangle, \tag{H.19}$$

and

$$\frac{1}{\mathcal{Z}} \frac{\partial^2 \mathcal{Z}}{\partial (\beta\mu_i)^2} = \left\langle N_i^2 \right\rangle. \tag{H.20}$$

Making the substitution $\beta\mu_i = \ln z_i$,

$$\langle N_i \rangle = z_i \frac{\partial \ln \mathcal{Z}}{\partial z_i} = \sum_\epsilon \left[1 + e^{\beta(\epsilon - \mu_i)}\right]^{-1}. \tag{H.21}$$

The squared number operator, however, is only slightly more involved. First, we write the particle number fluctuation in terms of the second log-derivative,

$$\left\langle N_i^2 \right\rangle - \langle N_i \rangle^2 = \frac{\partial^2 \ln \mathcal{Z}}{\partial (\ln z_i)^2} \tag{H.22}$$

which may be expanded as

$$\frac{\partial^2 \ln \mathcal{Z}}{\partial (\ln z_i)^2} = z_i \frac{\partial \ln \mathcal{Z}}{\partial z_i} + z_i^2 \frac{\partial^2 \ln \mathcal{Z}}{\partial z_i^2}, \tag{H.23}$$

where we recognize the first term on the right-hand side as $\langle N_i \rangle$. Evaluating the second term with the help of Eq. (H.18),

$$z_i^2 \frac{\partial^2 \ln \mathcal{Z}}{\partial z_i^2} = -\sum_\epsilon \left[1 + e^{\beta(\epsilon - \mu_i)}\right]^{-2}. \tag{H.24}$$

[1] While this argument is terse, a formal derivation involving mixed partial derivatives of the partition function yields the same result.

Now, recalling that $\langle N_i N_j \rangle_0 = \langle N_i \rangle_0 \langle N_j \rangle_0$ and that $\langle N_i \rangle = \langle N_j \rangle$ in the balanced case, we may combine all of the above to arrive at

$$\left\langle N_i^2 \right\rangle - \langle N_i N_j \rangle = \left\langle N_i^2 \right\rangle - \langle N_i \rangle^2 = \langle N_i \rangle - \sum_{\epsilon} \left[1 + e^{\beta(\epsilon - \mu_i)} \right]^{-2}. \tag{H.25}$$

Inserting Eq. (H.21) and combining the sums, the final expression may be written as

$$\left\langle N_i^2 \right\rangle_0 - \langle N_i N_j \rangle_0 = \frac{1}{4} \sum_{\epsilon} \cosh^{-2} \left[\frac{\beta}{2} (\epsilon - \mu) \right], \tag{H.26}$$

where the values of ϵ are given by (5.7) (modified for open boundary conditions).

REFERENCES

[1] S. Chu. The manipulation of neutral particles. *Rev. Mod. Phys.*, 70(3), Jul 1998.

[2] S. Chu. Laser trapping of neutral particles. *Sci. Am.*, Feb 1992.

[3] W.D. Phillips. Laser cooling and trapping of neutral atoms. *Rev. Mod. Phys.*, 70(3), Jul 1998.

[4] F. Serwane, G. Zürn, T. Lompe, T. B. Ottenstein, A. N. Wenz, and S. Jochim. Deterministic preparation of a tunable few-fermion system. *Science*, 332(6027):336–338, 2011.

[5] C. Chin, R. Grimm, P. Julienne, and E. Tiesinga. Feshbach resonances in ultracold gases. *Rev. Mod. Phys.*, 82:1225–1286, Apr 2010.

[6] X.-W. Guan, M.T. Batchelor, and C. Lee. Fermi gases in one dimension: From Bethe Ansatz to experiments. *Rev. Mod. Phys.*, 85:1633–1691, Nov 2013.

[7] M. Randeria, J.-M. Duan, and L.-Y. Shieh. Bound state, Cooper pairing, and Bose condensation in two dimensions. *Phys. Rev. Lett.*, 62(9), Feb 1989.

[8] S. Schmitt-Rink, C.M. Varma, and A.E. Ruckenstein. Pairing in two dimensions. *Phys. Rev. Lett.*, 63(4), Jul 1989.

[9] G. Bertaina and S. Giorgini. BCS-BEC crossover in a two-dimensional Fermi gas. *Phys. Rev. Lett.*, 106:110403, 2011.

[10] D. Blume. Few-body physics with ultracold atomic and molecular systems in traps. *Rep. Prog. Phys.*, 75:046401, 2012.

[11] T. Sowiński and M.Á. García-March. One-dimensional mixtures of several ultracold atoms: a review. *Rep. Prog. Phys.*, 82(10), Sep 2019.

[12] K. Huang. A critical history of renormalization. *Int. J. Mod. Phys. A*, 28:1330050, 2013.

[13] F. J. Dyson. The radiation theories of Tomonaga, Schwinger, and Feynman. *Phys. Rev.*, 75:486–502, Feb 1949.

[14] M. Gell-Mann and F. E. Low. Quantum electrodynamics at small distances. *Phys. Rev.*, 95:1300–1312, Sep 1954.

[15] K.G. Wilson. The renormalization group: Critical phenomena and the kondo problem. *Rev. Mod. Phys.*, 47:773–840, Oct 1975.

[16] B. Simon. The bound state of weakly coupled Schrödinger operators in one and two dimensions. *Ann. Phys.*, 97(2):279–288, 1976.

[17] B. Friedman. *Principles and Techniques of Applied Mathematics*. John Wiley & Sons, Inc., 1956.

[18] M.E. Peskin and D.V. Schroeder. *An Introduction to Quantum Field Theory*. Westview Press, 2016.

[19] K.G. Wilson. Renormalization group and critical phenomena. I. Renormalization group and the Kadanoff scaling picture. *Phys. Rev. B*, 4:3174–3183, Nov 1971.

[20] L.P. Kadanoff. Scaling laws for Ising models near T_c. *Physics Physique Fizika*, 2:263–272, Jun 1966.

[21] K.G. Wilson and J. Kogut. The renormalization group and the ϵ expansion. *Physics Reports*, 12(2):75–199, 1974.

[22] J.R. McKenney, N. Sato, W. Melnitchouk, and C.-R. Ji. Pion structure function from leading neutron electroproduction and SU(2) flavor asymmetry. *Phys. Rev. D*, 93:054011, Mar 2016.

[23] A. Pich. Effective field theory. pages arXiv:hep–ph/9806303, 1998.

[24] R. Machleidt and D.R. Entem. Chiral effective field theory and nuclear forces. *Physics Reports*, 503(1):1–75, Jun 2011.

[25] S. Gopalakrishnan. Self-adjointness and the renormalization of singular potentials, 2006.

[26] C.E. Shannon. Communication in the presence of noise. *Proceedings of the IRE*, 37, Jan 1949.

[27] V.N. Efimov. Weakly-bound states of three resonantly-interacting particles. *Sov. J. Nucl. Phys.*, 12(5), May 1971.

[28] H.-W. Hammer, A. Nogga, and A. Schwenk. Colloquium: Three-body forces: From cold atoms to nuclei. *Rev. Mod. Phys.*, 85:197–217, Jan 2013.

[29] N.C. Stone and N.W.C. Leigh. A statistical solution to the chaotic, non-hierarchical three-body problem. *Nature*, 576:406–410, Dec 2019.

[30] G.V. Skorniakov and K.A. Ter-Martirosian. Three body problem for short range forces. *Soviet Physics JETP*, 4, 1957.

[31] O.I. Kartavtsev and A.V. Malykh. Universal low-energy properties of three two-dimensional bosons. *Phys. Rev. A*, 74:042506, Oct 2006.

[32] E. Nielsen, D.V. Fedorov, and A.S. Jensen. Three-body halos in two dimensions. *Phys. Rev. A*, 56:3287–3290, Oct 1997.

[33] P.F. Bedaque, H.-W. Hammer, and U. van Kolck. The three-boson problem with short-range interactions. *Nucl. Phys. A*, 646:444–466, 1998.

[34] E. Nielsen, D.V. Fedorov, A.S. Jensen, and E. Garrido. The three-body problem with short-range interactions. *Phys. Rep.*, 347(5):373–459, 2001.

[35] M. Valiente. Three-body repulsive forces among identical bosons in one dimension. *Phys. Rev. A*, 100:013614, Jul 2019.

[36] A. Pricoupenko and D.S. Petrov. Three-body interaction near a narrow two-body zero crossing. *Phys. Rev. A*, 100:042707, Oct 2019.

[37] S. Paul, P.R. Johnson, and E. Tiesinga. Hubbard model for ultracold bosonic atoms interacting via zero-point-energy–induced three-body interactions. *Phys. Rev. A*, 93:043616, Apr 2016.

[38] S. Paul and E. Tiesinga. Large effective three-body interaction in a double-well optical lattice. *Phys. Rev. A*, 92:023602, Aug 2015.

[39] D.S. Petrov. Elastic multibody interactions on a lattice. *Phys. Rev. A*, 90:021601, Aug 2014.

[40] S. Will, T. Best, U. Schneider, L. Hackermüller, and D.-S. Lühmann. Time-resolved observation of coherent multi-body interactions in quantum phase revivals. *Nature*, 465:197–201, 2010.

[41] A.J. Daley and J. Simon. Effective three-body interactions via photon-assisted tunneling in an optical lattice. *Phys. Rev. A*, 89:053619, May 2014.

[42] C. Fey, J. Yang, S.T. Rittenhouse, F. Munkes, M. Baluktsian, P. Schmelcher, H.R. Sadeghpour, and

J.P. Shaffer. Effective three-body interactions in Cs($6s$)−Cs(nd) rydberg trimers. *Phys. Rev. Lett.*, 122:103001, Mar 2019.

[43] G. Guijarro, A. Pricoupenko, G. E. Astrakharchik, J. Boronat, and D. S. Petrov. One-dimensional three-boson problem with two- and three-body interactions. *Phys. Rev. A*, 97:061605, Jun 2018.

[44] V. Pashtukov. Ground-state properties of dilute one-dimensional Bose gas with three-body repulsion. *Phys. Lett. A*, 383:894–897, Feb 2019.

[45] Y. Nishida. Universal bound states of one-dimensional bosons with two- and three-body attractions. *Phys. Rev. A*, 97:061603, Jun 2018.

[46] Y. Sekino and Y. Nishida. Quantum droplet of one-dimensional bosons with a three-body attraction. *Phys. Rev. A*, 97:011602, Jan 2018.

[47] A. Goban, R.B. Hutson, G.E. Marti, S.L. Campbell, M.A. Perlin, P.S. Julienne, J.P. D'Incao, A.M. Rey, and J. Ye. Emergence of multi-body interactions in a fermionic lattice clock. *Nature*, 563:369–373, 2018.

[48] A. Bohrdt, A. Omran, E. Demler, S. Gazit, and F. Grusdt. Multiparticle interactions for ultracold atoms in optical tweezers: Cyclic ring-exchange terms. *Phys. Rev. Lett.*, 124:073601, Feb 2020.

[49] M.A. Perlin and A.M. Rey. Effective multi-body SU(N)-symmetric interactions of ultracold fermionic atoms on a 3d lattice. *New J. Phys.*, 21:043039, 2019.

[50] M. Takahashi. Many-body problem of attractive fermions with arbitrary spin in one dimension. *Prog. Theor. Phys.*, 44(4), Oct 1970.

[51] Á. Rapp, G. Zaránd, C. Honerkamp, and W. Hofstetter. Color superfluidity and "baryon" formation in ultracold fermions. *Phys. Rev. Lett.*, 98:160405, Apr 2007.

[52] R.A. Molina, J. Dukelsky, and P. Schmitteckert. Crystallization of trions in SU(3) cold-atom gases trapped in optical lattices. *Phys. Rev. A*, 80:013616, Jul 2009.

[53] J. Decamp, P. Armagnat, B. Fang, M. Albert, A. Minguzzi, and P. Vignolo. Exact density profiles and symmetry classification for strongly interacting multi-component Fermi gases in tight waveguides. *New J. Phys.*, 18:055011, 2016.

[54] Y. Nishida. New type of crossover physics in three-component Fermi gases. *Phys. Rev. Lett.*, 109:240401, Dec 2012.

[55] P. He, X. Yin, X. Guan, M.T. Batchelor, and Y. Wang. Analytical thermodynamics of a strongly attractive three-component Fermi gas in one dimension. *Phys. Rev. A*, 82:053633, Nov 2010.

[56] E.K. Laird, Z.-Y. Shi, M.M. Parish, and J. Levinsen. SU(n) fermions in a one-dimensional harmonic trap. *Phys. Rev. A*, 96:032701, Sep 2017.

[57] C.C.N. Kuhn and A. Foerster. Phase diagrams of three-component attractive ultracold fermions in one dimension. *New J. Phys.*, 14:013008, 2012.

[58] T.B. Ottenstein, T. Lompe, M. Kohnen, A.N. Wenz, and S. Jochim. Collisional stability of a three-component degenerate Fermi gas. *Phys. Rev. Lett.*, 101:203202, Nov 2008.

[59] J.H. Huckans, J.R. Williams, E.L. Hazlett, R.W. Stites, and K.M. O'Hara. Three-body recombination in a three-state Fermi gas with widely tunable interactions. *Phys. Rev. Lett.*, 102:165302, Apr 2009.

[60] A.N. Wenz, T. Lompe, T.B. Ottenstein, F. Serwane, G. Zürn, and S. Jochim. Universal trimer in a

three-component Fermi gas. *Phys. Rev. A*, 80:040702, Oct 2009.

[61] L. Salasnich. Three-component Fermi gas with SU(3) symmetry: BCS–BEC crossover in three and two dimensions. *Laser Phys.*, 23(1):015503, 2013.

[62] L. Salasnich. Condensate formation with three-component ultracold fermions. *Phys. Rev. A*, 83:033630, Mar 2011.

[63] G. Pagano, M. Mancini, G. Cappellini, P. Lombardi, F. Schäfer, H. Hu, X.-J. Liu, J. Catani, C. Sias, M. Inguscio, and L. Fallani. A one-dimensional liquid of fermions with tunable spin. *Nature Phys.*, 10:198–201, 2014.

[64] D.S. Petrov. Three-body interacting bosons in free space. *Phys. Rev. Lett.*, 112:103201, Mar 2014.

[65] P.A.M. Dirac. *The Principles of Quantum Mechanics*. Oxford University Press, 4$^{\text{th}}$ edition, 1958.

[66] J.E. Drut, J.R. McKenney, W.S. Daza, C.L. Lin, and C.R. Ordóñez. Quantum anomaly and thermodynamics of one-dimensional fermions with three-body interactions. *Phys. Rev. Lett.*, 120:243002, Jun 2018.

[67] J. Schwinger, L.L. DeRaad, K. Milton, and W.-Y. Tsai. *Classical Electrodynamics*. Westview Press, 1998.

[68] M. Abramowitz and I.A. Stegun. *Handbook of Mathematical Functions with Formulas, Graphs, and Mathematical Tables*. United States Department of Commerce, 1972.

[69] I.S. Gradshteyn and I.M. Ryzhik. *Table of Integrals, Series, and Products*. Elsevier, Inc., 7$^{\text{th}}$ edition, 2007.

[70] K.S. Thorne and R.D. Blandford. *Modern Classical Physics: Optics, Fluids, Plasmas, Elasticity, Relativity, and Statistical Physics*. Princeton University Press, 2017.

[71] E.T. Jaynes. *Probability Theory: The Logic of Science*. Cambridge University Press, 2003.

[72] E.T. Jaynes. Information theory and statistical mechanics. *Phys. Rev.*, 106(4):620–630, 1957.

[73] A.M. Kaufman, M.E. Tai, A. Lukin, M. Rispoli, R. Schittko, P.M. Preiss, and M. Greiner. Quantum thermalization through entanglement in an isolated many-body system. *Science*, 353(6301):794–800, 2016.

[74] J.R. McKenney, W.J. Porter, and J.E. Drut. Dynamics of entanglement entropy of interacting fermions in a 1D driven harmonic trap. *EPJ Web of Conferences*, 175:03002, 2018.

[75] R.K. Pathria and P.D. Beale. *Statistical Mechanics*. Elsevier, 3$^{\text{rd}}$ edition, 2011.

[76] G.E. Uhlenbeck and E. Beth. The quantum theory of the non-ideal gas. I. Deviations from the classical theory. *Physica*, 3(8):729–745, 1936.

[77] E. Beth and G.E. Uhlenbeck. The quantum theory of the non-ideal gas. II. Behaviour at low temperatures. *Physica*, 4(10):915–924, 1937.

[78] V. Ngampruetikorn, J. Levinsen, and M.M. Parish. Pair correlations in the two-dimensional Fermi gas. *Phys. Rev. Lett.*, 111:265301, Dec 2013.

[79] N. Hatano and M. Suzuki. *Finding exponential product formulas of higher orders*, pages 37–68. Springer Berlin Heidelberg, 2005.

[80] J. Drut and A.N. Nicholson. Lattice methods for strongly interacting many-body systems. *J. Phys. G: Nuclear and Particle Physics*, 40(4):043101, Mar 2013.

[81] A. Altland and B. Simons. *Condensed Matter Field Theory*. Cambridge University Press, 2nd edition, 2010.

[82] H.J.M. van Bemmel, D.F.B. ten Haaf, W. van Saarloos, J.M.J. van Leeuwen, and G. An. Fixed-node quantum Monte Carlo method for lattice fermions. *Phys. Rev. Lett.*, 72:2442–2445, Apr 1994.

[83] L. Rammelmüller, J.E. Drut, and J. Braun. A complex Langevin approach to ultracold fermions. *J. Phys.: Conference Series*, 1041:012006, Jun 2018.

[84] C.E. Berger, L. Rammelmüller, A.C. Loheac, F. Ehmann, J. Braun, and J.E. Drut. Complex Langevin and other approaches to the sign problem in quantum many-body physics. page arXiv:1907.10183, Jul 2019.

[85] A.C. Loheac and J.E. Drut. Third-order perturbative lattice and complex Langevin analyses of the finite-temperature equation of state of nonrelativistic fermions in one dimension. *Phys. Rev. D*, 95:094502, May 2017.

[86] H. Bethe. Zur Theorie der Metalle. *Z. Phys.*, 71:205–226, 1931.

[87] D. Kincaid and W. Cheney. *Numerical Analysis: Mathematics of Scientific Computing*. Brooks/Cole, 3rd edition, 2002.

[88] R. Kress. *Linear Integral Equations*. Springer, 3rd edition, 2013.

[89] S. Weinberg. Systematic solution of multiparticle scattering problems. *Phys. Rev.*, 133:B232–B256, Jan 1964.

[90] E.S. Page and D.R. Cox. The Monte Carlo solution of some integral equations. *Mathematical Proceedings of the Cambridge Philosophical Society*, 50(3):414–425, 1954.

[91] A. Doucet, A.M. Johansen, and V.B. Tadić. On solving integral equations using Markov chain Monte Carlo methods. *Appl. Math. Comput.*, 216:2869–2880, 2010.

[92] Z.Z. Yan and Z. Hong. Using the Monte Carlo method to solve integral equations using a modified control variate. *Appl. Math. Comput.*, 242:764–777, 2014.

[93] A. Erdélyi, W. Magnus, F. Oberhettinger, and F.G. Tricomi. Tables of integral transforms. vol. i. *ZAMM - Journal of Applied Mathematics and Mechanics / Zeitschrift für Angewandte Mathematik und Mechanik*, 34(12), 1954.

[94] R.P. Kanwal. *Linear Integral Equations*. Birkhäuser, 1997.

[95] L.B. Rall. Resolvent kernels of Green's function kernels and other finite rank modifications of Fredholm and Volterra kernels, 1976.

[96] B. Bazak and D.S. Petrov. Five-body Efimov effect and universal pentamer in fermionic mixtures. *Phys. Rev. Lett.*, 118:083002, Feb 2017.

[97] B. Bazak and D.S. Petrov. Energy of N two-dimensional bosons with zero-range interactions. *New J. Phys.*, 20(2):023045, Feb 2018.

[98] W. Pauli. The connection between spin and statistics. *Phys. Rev.*, 58:716–722, Oct 1940.

[99] L.D. Faddeev. Scattering theory for a three-particle system. *Soviet Physics JETP*, 12, 1961.

[100] A.G. Volosniev, D.V. Fedorov, A.S. Jensen, and N.T. Zinner. Hyperspherical treatment of strongly-interacting few-fermion systems in one dimension. *Eur. Phys. J. Spec. Top.*, 224:585–590, 2015.

[101] R. Shankar. *Principles of Quantum Mechanics*. Springer, 2nd edition, 1994.

[102] F. Bornemann. On the numerical evaluation of Fredholm determinants. *Math. Comp.*, 79:871–915, 2010.

[103] J.R. McKenney and J.E. Drut. Fermi-Fermi crossover in the ground state of one-dimensional few-body systems with anomalous three-body interactions. *Phys. Rev. A*, 99:013615, Jan 2019.

[104] A.J. Daley and J. Simon. Effective three-body interactions via photon-assisted tunneling in an optical lattice. *Phys. Rev. A*, 89:053619, May 2014.

[105] L. P. Pitaevskii and A. Rosch. Breathing modes and hidden symmetry of trapped atoms in two dimensions. *Phys. Rev. A*, 55:R853–R856, Feb 1997.

[106] X.-J. Liu, H. Hu, and P.D. Drummond. Three attractively interacting fermions in a harmonic trap: Exact solution, ferromagnetism, and high-temperature thermodynamics. *Phys. Rev. A*, 82:023619, Aug 2010.

[107] F. Werner and Y. Castin. General relations for quantum gases in two and three dimensions. II. Bosons and mixtures. *Phys. Rev. A*, 86:053633, Nov 2012.

[108] L. Pricoupenko. Isotropic contact forces in arbitrary representation: Heterogeneous few-body problems and low dimensions. *Phys. Rev. A*, 83:062711, Jun 2011.

[109] T. Busch, B.G. Englert, K. Rzażewski, and M. Wilkens. Two cold atoms in a harmonic trap. *Foundations of Physics*, 28(4):549–559, Apr 1998.

[110] A.J. Czejdo, J.E. Drut, Y. Hou, J.R. McKenney, and K.J. Morrell. Virial coefficients of trapped and un-trapped three-component fermions with three-body forces in arbitrary spatial dimensions. page arXiv:2003.04958, Mar 2020.

[111] N.J.S. Loft, A.S. Dehkharghani, N.P. Mehta, A.G. Volosniev, and N.T. Zinner. A variational approach to repulsively interacting three-fermion systems in a one-dimensional harmonic trap. *Eur. Phys. J. D*, 69(65), 2015.

[112] J.R. McKenney, A. Jose, and J.E. Drut. Thermodynamics and static response of anomalous 1D fermions via quantum Monte Carlo in the worldline representation. page arXiv:2003.01616, Mar 2020.

[113] H. Tasaki. The Hubbard model - an introduction and selected rigorous results. *J. Phys.: Condensed Matter*, 10(20):4354–4378, May 1998.

[114] R. Shankar. *Quantum Field Theory and Condensed Matter: An Introduction*. Cambridge University Press, 2017.

[115] F.H.L. Essler, H. Frahm, F. Göhmann, A. Klümper, and V.E. Korepin. *The One-Dimensional Hubbard Model*. Cambridge University Press, 2005.

[116] J. Browne. *Grassmann Algebra*, volume I: Foundations. Barnard Publishing, 2012.

[117] J. Zinn-Justin. *Path Integrals in Quantum Mechanics*. Oxford University Press, 2010.

[118] M.G. Endres. Lattice theory for nonrelativistic fermions in one spatial dimension. *Phys. Rev. A*, 85:063624, 2012.

[119] J.-W. Chen and D.B. Kaplan. Lattice theory for low energy fermions at nonzero chemical potential. *Phys. Rev. Lett.*, 92:257002, Jun 2004.

[120] P. Hasenfratz and F. Karsch. Chemical potential on the lattice. *Phys. Lett.*, 125B:308–310, 1983.

[121] H. Singh and S. Chandrasekharan. Few-body physics on a spacetime lattice in the worldline approach. *Phys. Rev. D*, 99:074511, Apr 2019.

[122] F.F. Assaad and H.G. Evertz. *World-line and Determinantal Quantum Monte Carlo for Spins, Phonons, and Electrons*, pages 277–356. Springer Berlin Heidelberg, 2008.

[123] N. Kawashima and K. Harada. Recent developments of world-line Monte Carlo methods. *Journal of the Physical Society of Japan*, 73(6):1379–1414, 2004.

[124] A.N. Rubtsov, V.V. Savkin, and A.I. Lichtenstein. Continuous-time quantum Monte Carlo method for fermions. *Phys. Rev. B*, 72:035122, Jul 2005.

[125] N. Metropolis, A.W. Rosenbluth, M.N. Rosenbluth, A.H. Teller, and E. Teller. Equation of state calculations by fast computing machines. *J. Chem. Phys.*, 21, 1953.

[126] S. Tan. Generalized virial theorem and pressure relation for a strongly correlated Fermi gas. *Ann. Phys.*, 323, 2008.

[127] M. D. Hoffman, P. D. Javernick, A. C. Loheac, W. J. Porter, E. R. Anderson, and J. E. Drut. Universality in one-dimensional fermions at finite temperature: Density, pressure, compressibility, and contact. *Phys. Rev. A*, 91:033618, Mar 2015.

[128] M. Girardeau. Relationship between systems of impenetrable bosons and fermions in one dimension. *Journal of Mathematical Physics*, 1(6):516–523, 1960.

[129] The Lord of the Rings: The Return of the King, 2003.

[130] E.Z. Ising. Beitrag zur Theorie des Ferromagnetismus. *Z. Phys.*, 31(1):253–258, Feb 1925.

[131] S.G. Brush. History of the Lenz-Ising model. *Rev. Mod. Phys.*, 39:883–893, Oct 1967.

[132] H.A. Kramers and G.H. Wannier. Statistics of the two-dimensional ferromagnet. Part I. *Phys. Rev.*, 60:252–262, Aug 1941.

[133] H.A. Kramers and G.H. Wannier. Statistics of the two-dimensional ferromagnet. Part II. *Phys. Rev.*, 60:263–276, Aug 1941.

[134] J.B. Kogut. An introduction to lattice gauge theory and spin systems. *Rev. Mod. Phys.*, 51:659–713, Oct 1979.

[135] L. Onsager. Crystal statistics. I. A two-dimensional model with an order-disorder transition. *Phys. Rev.*, 65:117–149, Feb 1944.

[136] L. Wang. Discovering phase transitions with unsupervised learning. *Phys. Rev. B*, 94:195105, Nov 2016.

[137] E. Luijten. *Introduction to Cluster Monte Carlo Algorithms*, pages 13–38. Springer Berlin Heidelberg, 2006.

[138] U. Wolff. Collective Monte Carlo updating for spin systems. *Phys. Rev. Lett.*, 62:361–364, Jan 1989.

[139] W. Krauth. *Cluster Monte Carlo Algorithms*, chapter 2, pages 5–22. John Wiley & Sons, Ltd, 2005.

[140] C.C. Pinter. *A Book of Abstract Algebra*. Dover Publications, Inc., 2nd edition, 2010.

[141] H.E. Camblong and C.R. Ordóñez. Renormalized path integral for the two-dimensional δ-function interaction. *Phys. Rev. A*, 65:052123, May 2002.

[142] G.F. Bertsch. *The Practitioner's Shell Model*. Elsevier, 1972.